Electrodeposition and Characterization of Oxide Semiconductors (SnO_2, Ga-O, and Fe-O) Thin Films

Name: Junie Jhon Magdadaro Vequizo

Doctoral Program in Engineering
Department of Engineering Physics, Electronics and Mechanics
Graduate School of Engineering
Nagoya Institute of Technology
Nagoya, Japan

Electrodeposition and Characterization of Oxide Semiconductors (SnO_2, Ga-O, and Fe-O) Thin Films

---

A Dissertation

Presented to
The Department of Engineering Physics, Electronics and Mechanics
Graduate School of Engineering
Nagoya Institute of Technology
Nagoya, Japan

In Partial Fulfillment
Of the Requirements for the Degree of
Doctor of Philosophy in Engineering

Junie Jhon Magdadaro Vequizo

March, 2014

ABSTRACT

Interests on transparent oxide semiconductors (TOS) have been increasing tremendously for wide range of technological and environmental applications. In particular, these TOS materials act as an integral part in the fabrication of *p-n* heterojunctions solar cells because of their fascinating optical, structural, and electrical properties. In this doctoral thesis, several *n-type*-oxide semiconductors; namely, SnO_2, Ga-O, and Fe-O thin films have been explored and investigated by employing electrodeposition at room temperature. Fabrication of heterostructures based on these materials along with the known *p-type* materials such as tin sulfide (SnS) and copper oxide (Cu_2O) are also demonstrated to elucidate their potentials in solar cell fabrication.

Tin oxide (SnO_2) thin films are electrodeposited on indium tin oxide (ITO) substrate from strongly acidic (pH < 1) aqueous solution containing $SnSO_4$. Oxygen bubbling is employed either before or during deposition. Transparent films are electrochemically produced from oxygen-bubbled solutions. Nearly stoichiometric ratios are attained for both as-deposited and annealed films. The *n-type* conductivity and the photosensitivity are evaluated and confirmed from photoelectrochemical (PEC) measurement. X-ray photoelectron spectroscopy (XPS) revealed that the Sn $3d_{5/2}$ and O 1s levels for the 250°C-annealed SnO_2 film after Argon-ion sputtering are shifted by 0.5 eV towards lower binding energy (E_B) relative to that at the surface. This effect might be originated from the shift of valence band maximum (VBM) as evidenced in the additional peak located near 2.6 eV. The electrodeposited SnS/SnO_2 superstrate structure with 250°C-annealed SnO_2 exhibits an open circuit voltage (V_{OC}) of 40-90 mV and a short circuit current density (J_{SC}) of 1.5-9.7 mA/cm^2. The highest solar conversion efficiency for electrodeposited SnS/SnO_2 heterostructure is estimated to be 0.14%. The valence band offset is determined to be approximately 1.85 eV. Using this value and the band gaps of individual layers, the conduction band minimum of SnO_2 is predicted to be higher than that of SnS by 0.65 eV.

Ga-O based thin films are electrodeposited on fluorine-doped tin oxide (FTO) substrate at room temperature from aqueous gallium sulfate solution with hydrogen peroxide (H_2O_2) as oxygen precursor. Effects of different deposition parameters such as deposition voltage, amount of H_2O_2 and deposition time are investigated. Nearly smooth and crack-free morphologies are attained at -1.0 (V vs SCE) deposition potential. As-deposited films have shown O to Ga ratio of 2.0, which signifies GaOOH formation. Thermal annealing in ambient air at 500-600°C reduces the O/Ga ratio and retains the morphology. As-prepared films with ~ 0.2 μm thickness have 80 % transparency in the visible wavelength range; however, the band gap of GaOOH could not be estimated because no absorption edge is observed. The SnS/GaOOH and Cu_2O/GaOOH heterojunctions have been fabricated via electrodeposition. In SnS/GaOOH, the rectification property is confirmed but not the photovoltaic characteristics. On the contrary, for the first time, the Cu_2O/Ga-O heterojunctions (with as-deposited and annealed GaOOH) display rectifying and photovoltaic characteristics. The solar cell parameters (V_{OC} = 0.15 V, J_{SC} = 0.35 mA/cm^2) and (V_{OC} = 0.22 V, J_{SC} = 0.45 mA/cm^2) are attained for Cu_2O/Ga-O heterojunctions with as-deposited and 400°C-annealed GaOOH layers, respectively.

γ-FeOOH films are electrodeposited on the ITO substrate from oxygen-bubbled aqueous $FeSO_4$-KCl solution at room temperature. Potential values near -0.7 (V vs SCE) are chosen to electrodeposit the films. A mixture of α-Fe and γ-FeOOH is achieved at more negative potential than -0.90 V and intense aggregation is favored at longer deposition time. Raman shifts at 252, 384, 538, and 664 cm^{-1} signify the characteristics of γ-FeOOH. The as-deposited γ-FeOOH film is nanocrystalline with crystallite size probably an order of nanometers. The *n-type* conductivity and photoresponse under illumination of γ-FeOOH film are confirmed from PEC measurement. The homogeneity of the anions in the solution is achieved by using sodium sulfate (Na_2SO_4) and the deposition current is enhanced by stirring. The γ-FeOOH films exhibit band gaps between 2.2 - 2.6 eV). A transformation of γ-FeOOH thin films to α-Fe_2O_3 is attained by thermal annealing at 400°C in air. In SnS/FeOOH fabricated by buffering the SnS solution, the rectifying behavior is demonstrated but not the photovoltaic properties. Interestingly, for the first time, the rectifying and photovoltaic properties of Cu_2O/FeOOH with as-deposited and 400°C-annealed FeOOH layers are successfully done by employing potentiostatic-galvanostatic electrodeposition techniques. The highest solar cell parameters (V_{OC} = 0.11 and J_{SC} = 0.95 mA/cm^2) are obtained for the Cu_2O/FeOOH heterostructure with 50 nm-thick as-deposited FeOOH layer.

ACKNOWLEDGMENTS

It is my honor to thank all the institutions and people who supported and guided me to make this research endeavor a significant and successful one.

I would like to express my deepest appreciation to the Monbukagakusho of the Ministry of Education (MEXT), Japan for the scholarship and to the Western Mindanao State University (WMSU), through the President, for the financial support and study leave grant to finish my master and doctorate studies in Nagoya Institute of Technology, Japan. I would also like to thank: Prof. Dr. Masaya Ichimura, my very kind and supportive research and thesis adviser, for sharing his expertise and persuasively conveyed the spirit of adventure in research, Assoc. Prof. Dr. Masashi Kato, my assistant supervisor, for the guidance and critical comments and suggestions during group discussions, and Dr. Marilou Elago, Dean of the College of Science and Mathematics-WMSU, for the moral support and encouragement.

I would like to thank the panel members, Prof. Drs. Yo Ichikawa and Masaki Maeda for being the examiners and critics of my thesis and for the comments and suggestions.

I am further indebted to Nakashima, Matsushita, Akita, Seki, Odon, Ashraf, Suphria, Muhibbullah, and Nishimura-san, for being my *senpais*, tutors and good friends, Mr. Fujimoto, AES technician, for sharing the knowledge in doing AES and SEM, Mr. Moriguchi for the technical assistance in doing the XPS characterization, Mr. Ishiguro for the assistance in operating the XRD machine and to the very fun-loving Ichimura-Kato laboratory members since 2008 to the present, especially to Wada, Aoki, Sakamoto, and Tajimi-san, Yamazaki, Maeda and Tanaka-kun and to my batch mates Ms. Song Ying, Mr. Yang Kai, and Ms. Bao Wujisiguleng, for the support and kindness in many things, and also the joy that made me feel at home while doing my research and studies.

I wish to thank the Department of Physics in WMSU, through the Chairman, for the constant support most especially to Profs. Jose Perano, Elsa Saavedra, Ma. Vivian Fernando, and Nerissa Mantilla; Sir Swidin Husin, Erwin Alonzo, Karla Belisario, Marvin Maulion, Vinchail Siason, and Aubrey May Flores. I would also like to thank Ma’am Gwen of Accounting and Cashier’s Office-WMSU for the help in lieu of my absence.

How grateful I am for the brotherly and sisterly kindness of Mary Jane Alcedo, Uncle Lemuel Platon, Dr. Rency Victoriano, my one of a kind NIT buddies: Dr. Raymond Virtudazo, Mr. Randy Jalem (also my cyclic voltammetry buddy), and Ms. Grace Domingo. Special thanks also to my dear friends, Drs. Gene Frederick Gagabe and Richard Alorro for the friendship and pieces of academic advice. I am also grateful to our generous dentist-friend, Dr. Atsushi Ogawa of Ogawa Family Dental Clinic-Nagoya, for the help and being a good friend and to Engrs. Jomel Libut and Arnold Dacwag, for the uplift during sad and good times.

I am very thankful also to my ever supportive Mama Rose, Manoy Erick, Manoy Naldo, Manang Rosemarie, Manoi Jeffrey, Tata, Kuya Christian, Inday Christine, Inday Icy, Ate Ester, Kuya Johndell, Michael, Jennelyn, Sadam, Dica, Kikim, Gogong, and Mia for the love, happiness and encouragement you have given me as always.

Most special thanks to my loving and very supportive wife, Heidi Belo-Vequizo, my source of endless encouragement, my inspiration, my proof-reader, and my enthusiastic listener to my everyday ups and downs.

To all the people and friends whom I forgot to mention, thank you so much for everything.

Above everything else, I am dedicating this work to our Almighty GOD, for Him all the honor and glory.

Junie Jhon Magdadaro Vequizo

Nagoya Institute of Technology
Nagoya, Japan, 2014

CONTENTS

CHAPTER

List of Figures and Tables

CHAPTER 1

INTRODUCTION

Environmental and energy-related issues have been the focal subjects of the development in engineering and technology. The continuous exploration of alternative and renewable energy resources provides long-term hope and goal to have clean and green environment. These alternative energy resources can be of great help to completely eradicate the serious problems brought by the existing conventional energy resources. Conventional energy resources such as fossil fuels (oil, natural gas, and coal) and nuclear energy have been the main sources of energy for a very long time. However, their availability has already been reduced significantly year after year and can be considered to reach extreme degradation few years from now. One cannot also disregard the environmental danger due to continuous emission of gas pollution in the surroundings, in which, it has large contribution in the worsening status of climate change. For these obvious and ubiquitous reasons, the search of alternative options is essential and worthy of doing.

Solar energy has been one of the best alternative renewable energy resources available to be harvested freely and safely by fabricating environment-friendly, stable, abundant, and promising materials or devices related to solar energy utilization or conversion. There are three familiar approaches towards energy conversion from sunlight [1]: (i) thermal approach where in solar radiation is absorbed by passive collection and conversion into thermal energy; it is then used in various purposes such as water heating, drying, and industrial heating; (ii) biological approach where in the solar energy is being promoted through photosynthesis, which can be used in the production of transportable fuels or electricity; and (iii) direct approach, in which energy conversion involves a one-step or direct conversion process that generates electrical energy from sunlight. This process can be described and illustrated in photovoltaic (PV) solar cell devices.

The idea of photovoltaic solar energy conversion is simple but the construction of the real photovoltaic device and solar panels for effective-harnessing of energy from the sun involves complex process and complicated problem usually arises. In principle, a solar cell is a junction device fabricated using two different materials with dissimilar roles in how solar conversion process is demonstrated within the device. The usual configuration of thin-film based solar cell is the *p-n* heterojunctions where in the *n* and *p* layers are stacked on top of each other to form a junction between them. In a simplest configuration, the *p-n* heterostructure consists of a substrate with transparent conducting oxide (TCO) that holds the thin film layers and draws the current to the outer circuit, a window or buffer layer to create junction with the absorber layer and to drive the generated carriers to the electrode, the absorber layer for carrier generation upon absorbing photons with minimal losses due to transmission and reflection, and metal contact layer as electrode contact. Understanding of the individual behaviors of these layers is essential for the design of the device. Moreover, the interface between different layers must be seriously considered since each layer has different structure, lattice constant, electron affinity/work function, physical and chemical properties, etc., the interfaces can cause stress, interdiffusion, defects and interface states that can act as recombination centers and affect the overall performance of the device.

The function of the buffer layer in heterojunction is primarily to form a junction with the absorber layer while allowing maximum amount of light to the junction region and absorber layer [2]. The beneficial effects of buffer layer can be two-fold: modifying the absorber layer' surface chemistry and providing protection on the sensitive interface during the subsequent window layer deposition [3]. Hence, the durability of the cell is enhanced by the presence of buffer layer at the same time protects the sensitive absorber layer.

Another important aspect is the selection of the materials as absorber layer in solar cell device. Essential parameters need to be considered include band gap, absorption coefficient and minority carrier diffusion length. The band gap should be capable to absorb the entire visible solar spectrum region. It has been demonstrated theoretically that a 10 % conversion efficiency can be achieved using any semiconductor with band gap between 0.8 to 2.4 eV [4-5]. Additionally, high absorption coefficients of the absorber layer will yield strong photon absorption characteristics and the thickness of the absorber can be reduced significantly with minimal absorption losses. With these characteristics, the absorber layer can be made thinner but still effective in absorbing the photons from the sun. Moreover, the other relevant parameter needs to be considered in choosing the absorber layer is the minority carriers' diffusion length, which describes the migration of carriers through diffusion process. After photon absorption and carrier generation in the absorber, the photogenerated carriers must be transported to the junction region with minimum losses. If the lifetime of minority carriers is long enough, then these carriers could reach the junction region and would be separated [6]. Diffusion length is influenced by the doping and impurity concentration, structure and the thickness of the absorber material.

Intensive studies have been performed by serious and committed researchers on the development and advancement of the photovoltaic devices-related research. This area of scientific and technological research is hoped to make significant contributions to the worldwide distribution of energy in the near future because it portrays and exhibits technical feasibility, economical, and very attractive. The PV power generation researches are expected to have major effect on the significant reduction of CO_2 emissions in the environment. PV solar cells have been in the limelight for quite some time with silicon (Si) gains the most attraction. Crystalline Si dominates the PV market for a long time, but due to some issues encountered during the large-scale production, the unit price of solar cells could not be lowered and it is still much higher than that of conventional energy source. These issues include low absorption coefficient ($\sim 10^3$ cm^{-1}) that can result in a large device thickness to absorb the solar irradiation, and consequently in complex manufacturing and high material cost. In this regard, Si-based PV materials cannot compete to the areas with readily available conventional power sources [7]. Thus, alternative materials as possible replacements to crystalline Si PV solar cells are needed to be explored and examined. Several replacements have been considered and investigated because of their promising properties with regards to their production with competitive efficiencies. Much effort has been performed by solar cell producers to improve efficiency and reduce manufacturing cost significantly in order to survive the challenging current market environment [8].

Thin film based Si solar cells have received special attention due to their potential for large areas and low-cost manufacturing. Conversion efficiencies of these solar cells vary depending on the structure. For instance, a single-junction amorphous solar panel exhibits an efficiency of 6 - 7 %. However, with the utilization of a double junction technology like a-Si:H/μc-Si:H junctions, the efficiency is increased up to 11 % [8-9]. Despite the many advantages that these solar cells can offer, efficiencies are still low compared to crystalline Si-based solar PV. By extending the structure to triple-junction, this will eventually improve further the efficiency by incorporating a thin intrinsic layer to obtain an *n-i-p* or *p-i-n* stacked triple-junction structures. But the processes involve in the fabrication of these solar cell structures require sophisticated equipment and careful considerations are needed in current matching, that is, generated current in individual cells must also flow in all cells since they are connected in series.

There are a lot of materials that are comparable to or even better than Si-based thin films in terms of physical and optical properties. Some of the potential candidates are copper indium (sulfide, selenide) -{CI(S,Se)} and copper indium gallium (sulfide, selenide) - {CIG(S, Se)}, cadmium telluride (CdTe), dye-sensitized solar cells (DSSC) and organic solar cells. They have already demonstrated promising and substantial progress in the area of materials research, device fabrication and technology development. Among these candidates, polycrystalline thin film solar cells based on CIS, CIGS, and CdTe compound semiconductors have shown large improvement in solar conversion efficiencies. Moreover, CIS, CIGS and CdTe have significant contributions in terrestrial applications because of their high efficiency, long-term stable performance, potential for low-cost production and high absorption coefficient (~ 10^5 cm^{-1}) [10]. A thin layer of ~ 2 μm of CIGS or CdTe thickness is enough to absorb the useful part of the solar spectrum. CIGS and CdTe solar cells with glass as the commonly used substrates achieved the highest efficiencies of 19.2 [11] and 16.5 % [12], respectively. Furthermore, the interest on flexible substrates gains much attention to develop innovations on flexible solar cells and other electronic devices. For instance, CIGS and CdTe - based solar cells have been reported to be efficient on polyimide [13, 15] and metal foils [14, 16] with 7 – 11 % and 12 – 18 % solar conversion efficiencies for CdTe and CIGS materials, respectively. In simple configurations, the solar cells based on CdTe and CIGS materials, which serve as *p*-type layers, utilize transparent conducting oxides (TCO) as front contact, an *n*-type wide band gap semiconductors as partner layers to form the *p*-*n* junction and specific metal layers as back contacts. The efficiencies of the solar cells could depend on various preparation methods in obtaining the individual layers. It is known that thin film deposition techniques have strong influence not only on the optoelectronic properties of the layers to be deposited but also on their interfaces. Cadmium sulfide (CdS) is commonly partnered in CIGS and CdTe solar cells as *n*-type layer in the described *p*-*n* configurations. However, problems such as undesirable interdiffusion of Cd into CIGS (or in CIS) layers during absorber deposition at elevated temperature and the toxicity of Cd are the critical challenges in considering the future of these structures. Intensive efforts have been performed to eradicate the use of CdS as buffer layers. Several oxides and sulfide *n-type* materials with band gaps between 2.0 – 3.8 eV such as ZnO [17-18], ZnMgO [19], $In(OH)_3$ [20], In_2S_3 [21-22], and ZnS [23] have been demonstrated and tested as alternative buffer layers. Interestingly, these materials can also be utilized as direct heteropartners of absorber layers to produce *p*-*n* heterojunctions. The resulting process is advantageous to reduce the cost because it eliminates an additional deposition step of a buffer layer. Nakada et. al achieved the breakthrough in the CdS-free configuration by using undoped ZnO and reported the highest efficiency of 12.8 % [18]. Further increase in the cell efficiency and the development of prospective non-toxic materials as buffer or window layers for the fabrication of *p*-*n* heterostructures will continue to boost the improvement of these solar cells. Other alternative buffer layers with wide band gaps and high optical transmission are still needed to be examined and investigated to reduce optical losses and modify the band alignment between the individual components of the solar cell structures.

Potential candidate materials as alternative wide band gap *n-type* layers are metal oxide semiconductors such as tin oxide (SnO_2), gallium oxide (Ga_2O_3), gallium oxyhydroxides (GaOOH), iron oxide (Fe_2O_3), and iron oxyhydroxides (FeOOH) thin films. With their interesting properties such as suitable band gaps as a general requirement for *n*-type layers, abundance of their constituents, and optical transparency make them good candidates for low-cost solar cell fabrication. Several deposition methods have been employed to prepare or deposit these oxides at room or slightly higher temperatures. Electrodeposition technique is one of these methods that demonstrate flexibility and simplicity characteristics. It has been widely used as room temperature deposition of thin and thick films with different morphologies and properties. Slightly elevated temperatures can also be possible depending on the desired thin film product.

Objectives

Various *n-type* metal oxides: SnO_2, Ga-O (Ga_2O_3 and GaOOH), and Fe-O (Fe_2O_3 and FeOOH) thin films have been considered and evaluated in this thesis as promising candidates for a wide range of device applications. Special attention has been given to these semiconducting metal oxides as potential gas sensors, transparent electrodes and window or buffer layers in thin-film based heterojunction solar cells. Several *p-type* absorber layers such as SnS and Cu_2O partnered with these *n-type* metal oxides to fabricate different superstrate heterostructures.

In this thesis, electrodeposition of transparent metal oxide semiconductors: SnO_2, Ga-O and Fe-O thin films are performed at room temperature from aqueous solutions with the following considerations:

(1) *SnO_2 thin film electrodeposition*: Dissolved oxygen induced by oxygen bubbling serves as the source of oxygen precursor. Two modes of electrolyte preparation are considered to electrodeposit SnO_2 thin films. These are (i) solution is bubbled only during deposition process and (ii) solution is bubbled only before deposition. Although there are already reports on electrodeposition of SnO_2 thin films, it is deemed wise to note that the deposition process employed in this study varies with deposition conditions and methods of preparation. This work aims (a) to investigate and discuss the constant potential electrodeposition of SnO_2 thin films from oxygen bubbled aqueous tin sulfate solution at room temperature with very low pH (< 1). Deposition at elevated temperature is also carried out to compare the quality of the films. In connection with the effect of oxygen bubbling, different deposition reaction mechanism to produce SnO_2 thin films onto the substrate is also proposed in this study. The reaction mechanism is different from the reported electrochemical reactions by other researchers working on electrodeposition of SnO_2 materials. Thermal annealing is also considered to investigate its effect on the quality and properties of the films; (b) the annealed-electrodeposited SnO_2 layer is then utilized to

fabricate SnO_2/SnS heterojunction solar cells. The fabricated heterostructure exhibits promising rectifying and photovoltaic characteristics. The interface of the heterostructure is also studied and investigated to explain and determine the valence and conduction band offsets experimentally by performing X-ray photoelectron spectroscopy (XPS).

(2) *Ga-O thin films*: Hydrogen peroxide (H_2O_2) instead of dissolved oxygen is used as an oxygen precursor to electrodeposit the films. Ga-O thin films are successfully deposited from aqueous gallium sulfate solutions containing H_2O_2. The option to utilize H_2O_2 in the deposition of Ga-O thin films is decided based on the significant observation on the substrate reduction effect during electrodeposition even if oxygen bubbling is induced in the process. Electrochemical parameters such as amount of H_2O_2, deposition potential and deposition time are considered for optimization to produce quality Ga-O thin films. The formation of Ga-O thin films involves electroreduction of H_2O_2 forming OH^- ions and these electrochemically produced ions combine with Ga^{3+} ions in the working solution to form GaOOH thin films on the substrate. Thermal annealing is also performed to study and investigate the quality, morphology and structure of the films after heat treatment. As-deposited and annealed GaOOH are then partnered with electrodeposited *p-type* Cu_2O to fabricate heterojunction solar cells and the characteristics and the performance of the heterostructures are presented and evaluated.

(3) *Fe-O thin films*: Oxygen bubbling is employed to facilitate the formation of Fe-O thin films on the substrate. The overall electrochemical reaction is discussed according to the starting precursors and the composition of the final product. The formation of Fe-O thin films is studied and investigated based on the considered electrochemical quantities: deposition time, applied potential, oxygen bubbling, stirring condition, and the nature of supporting electrolytes (KCl and Na_2SO_4). Thermal annealing is also considered to study its effect on the composition, morphology, and structure of the films. As-prepared and annealed Fe-O samples are then utilized to fabricate *p-n* heterojunctions. The performance and characteristics of the heterostructures are evaluated and discussed.

Significance of the Study

Fabrication of low-cost, environment-friendly, and efficient solar cells remains certainly possible by employing facile electrodeposition method. Several studies have been reported to synthesize, grow, and deposit SnO_2, Fe-O (γ-FeOOH and α-Fe_2O_3) and Ga-O (GaOOH and Ga_2O_3) transparent oxides in micro- and/or nano-structures. The deposition process employed in this study differs from the existing works on ECD of these materials. Different oxygen precursors are utilized and investigated to successfully produce the desired oxide materials for their potential use in electronic device applications such as transparent electrodes, gas sensors and solar cell fabrication.

Scope and Limitations

This study focuses mainly on the electrodeposition and characterization of SnO_2, Ga-O and Fe-O thin films using different oxygen precursors (dissolved oxygen induced by bubbling and hydrogen peroxide). Electrochemical parameters such as deposition time, pH, and deposition potential are considered for optimization of the quality of the electrodeposited films. The as-deposited and annealed transparent oxide films are then utilized as window layers along with the potential absorber layers such as SnS, and Cu_2O to fabricate heterojunction solar cells. The details on the growth kinetics during the electrodeposition of transparent oxide films are beyond the scope of the study.

Thesis Organization

As for the structure of this thesis, it is divided into eight (8) main chapters. It starts with the introduction and motivations in **Chapter 1**, where the main objectives and focus of the study are presented. This is followed by a brief review of related literature in **Chapter 2** about the characteristics of transparent oxide semiconductors: SnO_2, Ga-O, and Fe-O fabricated by electrodeposition and fundamentals of various chemical deposition techniques. For the results and discussion on electrodeposition of SnO_2 thin films from oxygen-bubbled aqueous solutions, **Chapters 3** and **4** present the details of these. In **Chapter 3**, the results and discussion on the electrodeposition of SnO_2 thin films with oxygen bubbling only during deposition are arranged according to the cyclic voltammetry, optimization of electrochemical parameters, surface morphological, structural, and composition studies, optical transmission and conductivity measurements. In **Chapter 4**, the result and discussion on the electrodeposition of SnO_2 thin films with oxygen bubbling only before deposition are arranged in the same manner of presentation of results and discussion in **Chapter 3** with the addition of effect of thermal annealing on the surface morphology and composition of the film samples. Fabrication of SnO_2/SnS heterostructure along with the *I-V* measurements for the SnO_2-based heterojunctions are presented and discussed in **Chapter 5**. In **Chapter 6**, results and discussion on the electrodeposition of Ga-O thin films from aqueous iron sulfate solution are arranged similar to the presentation in **Chapters 3** and **4** that starts from optimization of usual electrochemical parameters with the addition of the control of H_2O_2 concentration. Characterizations of the electrodeposited Ga-O films such morphological, structural and composition studies including optical transmission, conductivity and photosensitivity measurements and fabrication of Ga-O based heterojunctions are discussed and presented. Electrodeposition and characterization of Fe-O thin films oxygen-bubbled solutions are presented in **Chapter 7**. The results and discussion are arranged in the same manner of presentation in **Chapters 3**, **4**, and **6**. The evaluation of the results in the fabrication of the photovoltaic performance of Fe-O based heterojunctions is also included and discussed for the potential use of Fe-O thin films in electronic device applications. The brief summary, concluding remarks and suggestions for future works are presented in **Chapter 8**.

References

[1] A. M. Abdel Haleem Hassan: Electrochemical Deposition of InS-based Thin Films for Photovoltaic Applications, **Ph.D. Thesis** (2010) & references therein.

[2] B. E. McCandless and S. S. Hegedus: Proc. of the 22nd IEEE Photovoltaic Specialists Conference (1991) 967.

[3] J. Sterner: *Comprehensive Summaries of Uppsala Dissertations from the Faculty of Science and Technology,* **942** (2004) 14.

[4] M. Prince: J. Appl. Phys. **26** (1995) 534.

[5] J. J. Loferski: J. Appl. Phys. **27** (1956) 777.

[6] R. Trykozko: Opto-Electr. Rev. **5** (4) (1997) 271.

[7] R. M. Vequizo: Growth and Structural Characterization of Epitaxial $CuInS_2$ Thin Films on Si (001) and on GaP (001), **Ph.D. Thesis** (2007) & references therein.

[8] S. Kim, J.-W. Chung, H. Lee, J. Park, Y. Heo, and H.-M. Lee: Sol. Energy Mater. Sol. Cells **119** (2013) 26.

[9] J. Bailat, L. Fesquet, J.-B. Orhan, Y. Djeridane, B. Wolf, P. Madliger et al.: Proceeding of the 25th European Photovoltaic Solar Energy Conference (2010) 2720.

[10] A. Romeo, M. Terheggen, D. Abou-Ras, D. L. Bätzner, F.-J. Haug, M. Kälin, D. Rudmann, and A. N. Tiwari: Prog. Photovolt: Res. Appl. **12** (2004) 93.

[11] K. Ramanathan, M. A. Contreras, C. L. Perkins, S. Asher, F. S. Hasoon, J. Keane, D. Young, M. Romero, W. Metzger, R. Noufi, J. Ward, and A. Duda: Prog. Photovolt.: Res. Appl. **11** (1999) 225-230.

[12] X. Wu, J. C. Kane, R. G. Dhere, C. DeHart, D. S. Albin, A. Duda, T. A. Gessert, S. Asher, D. H. Levi, and P. Sheldon: Proc. 17th European Photovoltaic Solar Energy Conference and Exhibition, Munich (2002) 995.

[13] A. N. Tiwari, M. Krejci, F.-J. Haug, and H. Zogg: Prog. Photovolt.: Res. Appl. **7** (1999) 393.

[14] J. R. Tuttle, A. Szalaj and J. Keane: Proc. 28th IEEE Photovoltaic Specialist Conference, Anchorage (2000) 1042.

[15] I. Matulionis, S. Han, J. A. Drayton, K. J. Price, and A. D. Compaan: Proc. 2001 MRS Spring Meeting, San Francisco (2001) H8.23.1.

[16] A. Romeo, M. Arnold, D. L. Bätzner, and H. Zogg: Proc. PV Europe – from PV Technology to Energy Solutions Conference and Exhibition (2002) 377.

[17] L. C. Olsen, H. Aguilar, F. W. Addis, W. Lei, and J, Li: Proc. of the 25th IEEE Photovoltaic Specialists Conference (1996) 997.

[18] T. Nakada and T. Mise: Proc. 17th European Photovoltaic Solar Energy Conference, Munich (2011) 1027.

[19] T. Negami, T. Aoyagi, T. Satoh, S. Shimakawa, S. Hayashi, and Y. Hashimoto: Proc. 29th IEEE Photovoltaic Specialist Conference, USA (2002) 656.

[20] K. O. Velthaus, J. Kessler, M. Ruckh, D. Schmid, and H. W. Schock: Proc. 11th European Photovoltaic Solar Energy Conference, Switzerland (1992) 842.

[21] N. Naghavi, S. Spiering, M. Powalla, B. Cavana, and D. Lincot: Prog. Photovolt. Res. Appl. **11** (2003) 437.

[22] S. Spiering, A. Eicke, D. Hariskos, M. Powalla, N. Naghavi, and D. Lincot: Thin Solid Films **451-452** (2004) 562.

[23] K. Kushiya, T. Nii, I. Sugiyama, Y. Sata, Y. Inamori, H. Takeshita: Jpn. J. Appl. Phys. **35** (1996) 4383.

CHAPTER 2

Review of Related Literature

The main focus of this work is on the fabrication of oxide semiconductor thin films by employing facile electrodeposition technique at room temperature for various device applications. This chapter begins with the brief presentation and discussion on the significant contributions that the development of thin film technology can offer; followed by the discussion on the characteristics of various oxide semiconductor materials that are fabricated in this work to have insights on their physical, structural and electronic properties. Elucidations of several deposition techniques are also presented to explain their differences in processing, advantages, and limitations in relation to thin film preparation.

2.1 Thin Film Technology

Thin film technology tremendously makes an impact on the advancement of scientifically and environmentally-related things or devices that we are enjoying and utilizing in our daily lives. Thin film coatings on items from mirrors to camera lenses to sunglasses to glass windows to television and computer displays provide an enhanced optical properties and performance that made our life easier and enjoyable. Architectural glass is often coated to reduce the heat load in large office buildings and provide significant cost savings by reducing air conditioning requirements. Thin film coatings in aircraft windows have been found to effectively evaporate ice or fogs upon heating the coating by applying potential over it [1]. Furthermore, the enhanced properties of the glass windows coated with metal oxide thin film have been demonstrated by effective reflection of infrared light emitted by the objects in a room [2]. The performance of optical coatings is typically enhanced when the thin film coating consists of multiple layers with variation in thickness and refractive index. Moreover, a periodic structure of alternating thin films made of different materials may collectively form a super-lattice, which exploits the phenomenon of quantum confinement by restricting electronic phenomena to two-dimension. Furthermore, the developments of transparent conducting oxides (TCO) materials have demonstrated significant contributions in thin film technology research. For instance, the efficiency of a superstrate-type thin film-Si solar cell strongly depends on the quality of the textured TCO layer used as the front electrode material. To improve cell efficiency, it is necessary to prepare a TCO layer with a high transparency in the solar spectrum and to optimize the surface morphology for light scattering by controlling the deposition and texturing conditions [3].

2.2 Characteristics of SnO_2

The rutile structure of tin oxide (SnO_2) has tetragonal unit cell belongs to a space-group symmetry $P_{42/mnm}$ and with lattice constants, $a = b = 4.7380$ Å, $c = 3.1865$ Å. The Sn and O atoms have 6-3 coordination, that is, Sn atoms are six-fold coordinated and O atoms are three-fold coordinated, as depicted in Fig. 2.1. SnO_2 is usually regarded as oxygen-deficient *n-type* semiconductor. This means that SnO_2 prefers to give up oxygen and can accommodate electrons more easily than holes in its lattice [4]. Thus, oxygen vacancies are always the source of electron carriers for an undoped material. SnO_2 is a prototype material for the development of transparent conducting oxides. Its wide direct band gap characteristics (~3.6 – 3.8 eV), high transparency in the visible region, high mechanical hardness, and environmental compatibility are the interesting features that are essential and plausible for electrode materials [5-7], gas sensors [8-11], solar cell fabrication [12-18], transparent and protective coatings [1-2, 19-27], and other device applications.

In gas sensors applications, when SnO_2 surface is exposed to air, oxygen absorbs onto the surface as O^{2-} ads or O^{-} ads. These adsorbed molecules form an electron depletion layer just below the SnO_2 surface and consequently make the SnO_2 highly resistive [28-31]. When reducing gases (e.g. H_2 and CO) are introduced as gas ambient, the adsorbed oxygen species are removed through the oxidation of reducing gases and the electrons that are being captured in the process are restored in the conduction band. This results to the decrease of the resistance and/or resistivity, which can be recorded and measured easily, of the oxide material [32]. Moreover, photochemically deposited SnO_2 thin films as hydrogen gas sensors are found to be highly sensitive at room temperature [33-34]. Introducing impurities such as Cu, Fe, Co and Ni on the undoped SnO_2 can enhance the electrical properties of the material [35-38] and can promote change or modify the surface morphology and decrease the grain size [39].

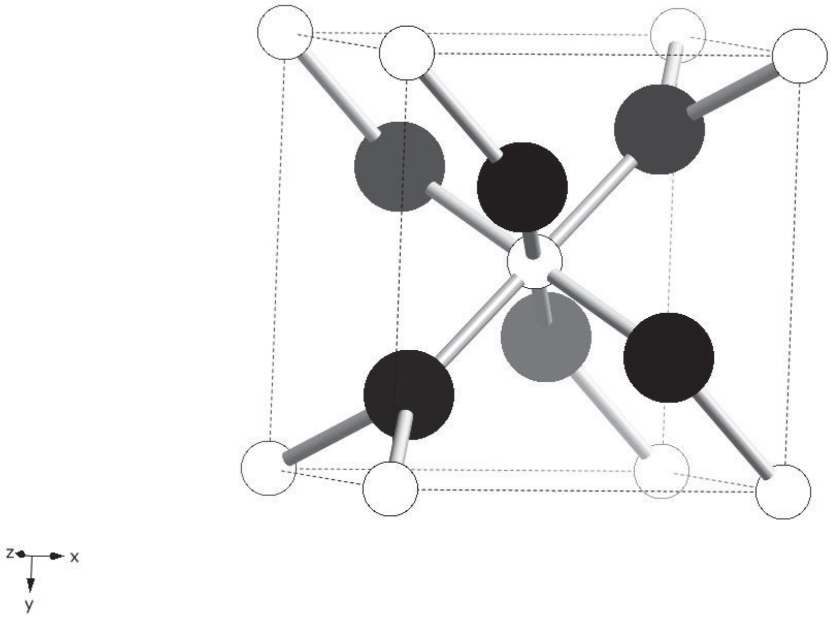

Fig. 2.1 Rutile structure of SnO_2. Smaller-white and bigger-dark circles are tin and oxygen atoms, respectively.

Completely stoichiometric undoped tin oxide would be an insulator, but a reasonable degree of conductivity can be achieved by stoichiometric deviation or by doping. Undoped tin oxide films often show some degree of conductivity because of unintentional doping with Cl^- or due to non-stoichiometry, mostly caused by oxygen vacancies in the lattice. These vacancies contain electrons from the removed oxygen atom, which can be excited to the conduction band. If too many oxygen vacancies are created, the structure can change into SnO with excess oxygen, which often has a negative influence on the conductivity. Another possibility for increasing the conductivity of tin oxide is the incorporation of suitable ions in the lattice. Substituting Sb^{5+}, Sb^{3+}, In^{3+}, P^{5+}, or As^{3+} for Sn^{4+}, or substituting F^-, Cl^- for O^{2-}, results in a donor level in the energy band gap causing a higher conductivity. The charge carriers generated by non-stoichiometry and doping are scattered by various mechanisms, like ionized impurity scattering, neutral impurity scattering, grain boundary scattering, and scattering at other defects and dislocations. Thus, the conductivity is dependent on the composition and the morphology of the layer, which in turn is dependent on deposition parameters like substrate temperature, film thickness, gas flow rate, precursor composition, and post-deposition annealing [40].

For solar cell fabrication, tin oxide is often used as the top window layer in semiconductor/insulator/semiconductor (SIS) solar cells because of its high electrical conductivity and high optical transmission properties. The top wide band gap semiconductor in SIS solar cells is expected to provide the window of incident photons from sunlight, that is, photons pass the window and reach the junction without being absorbed. Most of the reported SIS configuration contain either SnO_2 or indium tin oxide (ITO) as the window layer and single-crystalline or polycrystalline Si as the absorber layer. Many SIS solar cells have demonstrated efficiencies above 10 % and several have produced high efficiencies in the same range as diffused *p-n* junction cells [41-45]. For similar reasons, it is often used as substrates such as fluorine-doped SnO_2 (electrode material) for growing or depositing thin films that can be utilized further in the fabrication of heterojunction solar cells as buffer or window layers in *p-n* heterostructures. Additionally, SnO_2 can be combined with conducting organic polymers (COPs) to fabricate hybrid solar cell. COPs are capable to transport, emit or absorb light under specific conditions [46-47]. With the application of SnO_2 to fabricate poly (2-methoxy-5-(2'ethyl-hexoxy)-1,4—phenylene-vinylene) or MEH-PPV/SnO_2 solar cell provides a good choice as electron transport material, which neglects or decreases the degradation of the MEH-PPV polymer during irradiation under ambient atmospheres [46]. It has been studied and reported that the electron transfer from MEH-PPV polymer to SnO_2 is energetically favorable and can be photoinduced [46, 48]. Hence, COPs partnered with wide band gap transparent oxides will open other options to have efficient solar cell devices.

Another interesting aspect of SnO_2 material is the reconstruction of SnO_2 with respect to the positioned oxygen atoms. For instance, the reconstructions of SnO_2 (110) and SnO_2 (101) surfaces can result to oxygen deficient surface. The stoichiometric (110) surface is the most stable surface at high oxygen chemical potentials. However, at lower oxygen chemical potentials, one of the reduced (101) surface terminations is energetically favored [49-51]. This implies that the surface of the material can act as a sink of oxygen vacancies for many times. In addition, the dual valency of Sn at the surface of SnO_2 material can cause dramatic change on the surface transformation of the material. For example, the stoichiometric surface with Sn^{4+} is reduced to a surface with Sn^{2+}. Reduction of the surface can lead to the formation of Sn 5s surface derived surface states that lie deep within the band gap. This can cause lowering of the work function [52]. Moreover, derivations from the stoichiometric composition by introducing oxygen vacancies can cause high conductivity while maintaining the transparency of the material. This is due to the low carrier density of $10^{19} – 10^{21}$ cm^{-3} and high mobility of 150 cm^2 V^{-1} s^{-1} at room temperature [53-54].

2.3 Ga-O (Ga_2O_3 and GaOOH) characteristics

Ga-O based materials such as Ga_2O_3 and GaOOH are promising materials for wide-range of device applications. β-Ga_2O_3 has a monoclinic crystalline structure with dimensions a = 12.23, b = 3.04, c = 5.80 Å and β = 103.7° [55-56]. There are 4 Ga_2O_3 in the unit cell. The most probable space group to which the crystal belongs is C_{2h}^{3}-$C2/m$, that is, the atoms are in five sets of special positions 4*i*: (000, ½ ½ 0) ± *(x0z).* There are two kinds of coordination for Ga^{3+} ions in this structure, namely tetrahedral and octahedral. Average inter-ionic distances are: tetrahedral Ga-O (1.83 Å), octahedral Ga-O (2.00 Å), tetrahedron edge O-O (3.02 Å) and octahedron edge O-O (2.84 Å). Because of the reduced coordination of half of the metal ions, the density of β-Ga_2O_3 is lower than that of α-Ga_2O_3 which has the α-corundum structure, as shown in Fig. 2.2, where oxygen ions are situated in approximately hexagonal closed-pack array with all the Ga^{3+} ions octahedrally coordinated to O^{2-} ions. Also in the α-phase, the octahedral share edges and faces which bring the metals ions very near each other. In β-Ga_2O_3 no faces are shared between polyhedra and the shortest Ga^{3+}-Ga^{3+} distance is 3.04 Å [56]. Usually the structures, in which the faces of polyhedra are shared, are less stable than those in which edges are shared, which in turn are less stable than structures in which only corners are shared [57]. Thus, one would expect the β phase to be more stable than the *α*-phase. Foster et al. have shown that although the α-Ga_2O_3 forms at lower temperatures than β-Ga_2O_3, the *α*-phase is metastable [58]. Additionally, it is known that the wave function of the conduction band bottom of β-Ga_2O_3 is composed of mostly 4s orbitals of Ga^{3+} in octahedral sites [59-60].

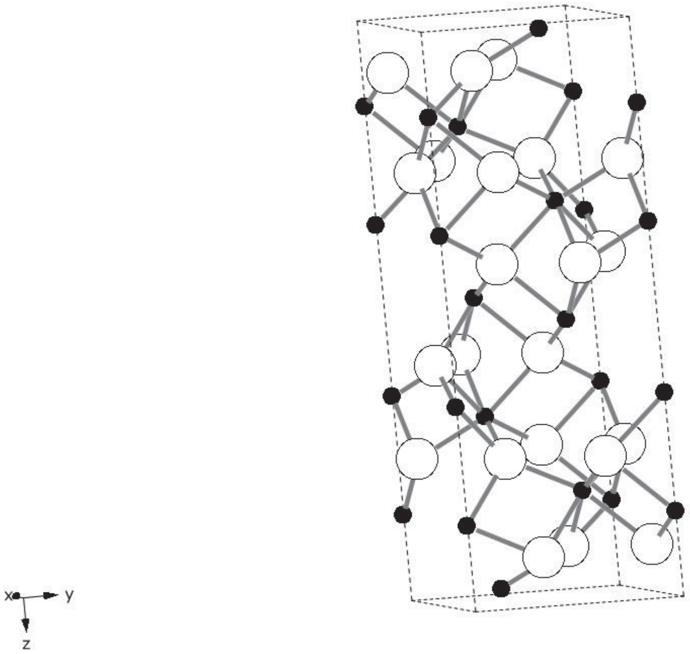

Fig. 2.2 Corundum structure of β-Ga_2O_3. Filled-smaller and empty-bigger circles are Ga and O atoms, respectively.

β-Ga_2O_3 material has been considered as a wide band gap (E_g ~ 4.9 eV [60-61]) semiconductor with interesting electrical and optical properties at high temperatures. It is the most stable Ga_2O_3 phase and exhibits *n*-type semiconductor property at high temperatures over 600°C due to oxygen deficiency in the crystal [62]. In fact, this oxide material can detect only oxygen gas over 900°C [63]. Moreover, Nakagomi et al. have fabricated and demonstrated the hydrogen gas sensing ability of β-Ga_2O_3 single crystals operating at high temperature [64-65]. Hence, β-Ga_2O_3 is potential materials for high temperature gas sensors. Other applications of β-Ga_2O_3 include deep ultraviolet (UV) photodetectors (flame sensors and UV radiation monitoring below the ozone hole) [66], photocatalytic decomposition of organic pollutant perfluorooctanic acid ($C_7F_{15}COOH$) under 254 nm UV irradiation [67] and benzene under ambient conditions [68].

Gallium oxide hydroxide (GaOOH) is an important material for the chemical synthesis of Ga_2O_3 and gallium nitride (GaN). Thermal annealing has been effective in transforming GaOOH to either α-Ga_2O_3 or β-Ga_2O_3 depending on the annealing temperature. For instance, rhombohedral α-Ga_2O_3 can be readily obtained by heating GaOOH powders as starting materials at 420^{o}C in oxygen ambient [69] or GaOOH nanorods prepared by hydrothermal method are transformed to β-Ga_2O_3 with similar nanorods morphology at 700^{o}C [70]. The crystal structure of GaOOH is reported to be analogous to that of diaspore (α – AlOOH) [71], which has orthorhombic crystal symmetry, i.e, it consists of double chains of an edge-shared octahedron. The formation of GaOOH depends on the reactions involve in the deposition process. For example, GaOOH precipitates are easily formed in aqueous solutions and are usual product of thermohydrolysis of metal cations in aqueous solutions accompanied by proton (H^+) generation. The kinetics of formation is influenced by the temperature. Under this condition, water acts as an effective reactant in hydrolysis. The formation is described and represented by [70, 72]

$$Ga^{3+} + 2H_2O \rightarrow GaOOH + 3H^+ \tag{2.1}$$

If transfer of electrons is involved in the formation of GaOOH onto the substrate like in the case of electrochemical deposition or electrodeposition process from gallium nitrate solution at elevated temperature of 80^{o}C, the formation is mainly based on the generation of OH^- ions at the cathode electrode (different from the hydrolysis process described in reaction 2.1). The rate of formation or growth is strongly influenced by the applied potential, which controls the OH^- ions generated near or at the cathode. With the starting materials, the generated OH^- ions are the products of electrochemical reduction of precursors such as nitrate ions (NO_3^-) and dissolved O_2 in aqueous gallium nitrate solution [73]. These generated OH^- ions then react with Ga^{3+} to produce GaOOH. The OH^- ion generation process is similar to the process involves in the formation of zinc oxide (ZnO) from aqueous zinc nitrate solution with nitrate ions as oxygen precursors [74-76].

2.4 Fe-O (Fe_2O_3 and FeOOH) characteristics

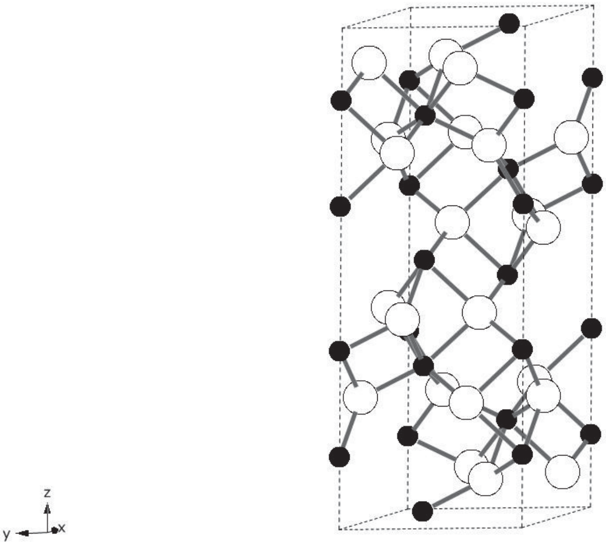

Fig. 2.3 Hematite (α-Fe_2O_3) structure. Dark-small and white-bigger circles represent Fe and O atoms, respectively.

Iron oxides are inexpensive materials utilized for many catalytic reactions such as hydrogen production [77] and oxidation of alcohols [78]. The common iron oxides used in catalytic applications are the most stable hematite (α-Fe_2O_3) and magnetite (Fe_3O_4). Their semiconducting properties make them suitable for oxidation-reduction reactions. α-Fe_2O_3 is also an attractive *n-type* semiconductor material for photoelectrochemical solar cells [79] because of its chemical stability in aqueous solutions and its relatively small band gap of 2.2 eV (it can able to absorb most of the photons of solar spectrum about 40 % of incident solar radiation). The maximum theoretical energy efficiency of α-Fe_2O_3 under AM 1.5 illumination is approximately 13 % when utilized as water splitting material [80]. Moreover, nanostructured α-Fe_2O_3 thin films are suitable for hydrogen production by developing multi-junction hybrid photoelectrodes. The gas sensing ability of α-Fe_2O_3 materials has been reported and demonstrated for the detection of combustible gases such as CH_4, C_3H_8, and *i*-C_4H_8. Furthermore, α-Fe_2O_3 can also be used as an electrode in non-aqueous and alkaline rechargeable batteries [81].

Hematite (α-Fe_2O_3) exhibits the rhombohedral-corundum (α-Al_2O_3) structure as shown in Fig. 2.3. The structure of α-Fe_2O_3 can be described as an array of oxygen ions stacked along the [001] anions. The Fe (III) ions filled the two thirds of the sites, which are arranged regularly with two-filled sites followed by a vacant one so that it forms a six-fold ring [82]. It has antiferromagnetic properties below ~260 K (Morin transition temperature) and shows weak ferromagnetism between 260 and Néel temperature (950 K) [83]. Several methods have been employed to prepare α-Fe_2O_3 materials with micro- and nano-structure morphologies for different applications.

Maghemite (γ-Fe_2O_3) is another polymorph of iron oxide material. It has a cubic structure (as depicted in Fig. 2.4) and considered metastable because it can be converted to the α-Fe_2O_3 at high temperatures. Maghemite has ferromagnetic features that make it applicable in the fabrication of recording tapes. The superparamagnetic property of γ-Fe_2O_3 material can be achieved when they are produced as ultrafine particles with sizes smaller than 10 nm. Additionally, γ-Fe_2O_3 can be prepared by several methods such as thermal dehydration of γ-FeOOH and careful oxidation of iron (II, III) oxide and Fe_3O_4 [84].

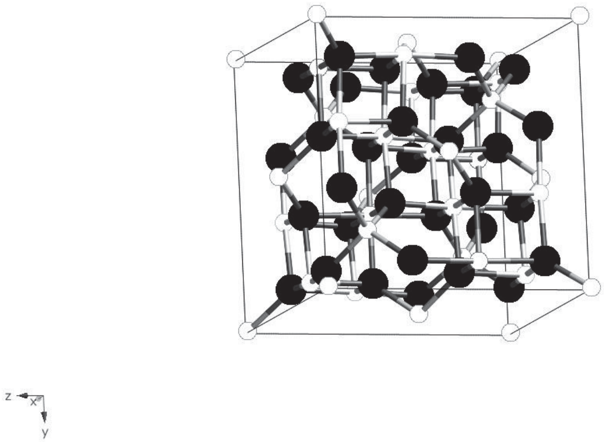

Fig. 2.4 Maghemite (γ-Fe_2O_3) structure [85]. Smaller and bigger circles are Fe and O atoms, respectively.

Meanwhile, iron oxide hydroxides (FeOOH) have gained interest for their potential usage in scientific, technological and environmental applications. Several iron oxide hydroxide polymorphs are known such as α-, β- and γ-FeOOH. The high specific surface areas of these oxide hydroxides compared to iron oxides and other metallic oxides make them potential candidates for adsorbent materials for the removal of heavy metal ions. Oxide hydroxides, particularly α- and γ-FeOOH, have demonstrated effective performance in the removal of heavy metal ions such as As(V) and Cr(VI) ions in polluted water and aqueous solutions [86-88] and in the adsorption of alpha amino acids in water/α-FeOOH interface [89]. Moreover, FeOOH materials have been also utilized as starting precursors in obtaining the most thermodynamically and chemically stable phase (α-Fe_2O_3) by thermal annealing process. Depending on the annealing condition, FeOOH can be transformed to metastable phase (γ-Fe_2O_3) at relatively lower temperature or to the most stable phase (α-Fe_2O_3) at much higher temperature. For instance, it is known that γ-FeOOH upon heating in air decomposes to γ-Fe_2O_3 and at higher temperatures transforms into α-Fe_2O_3.The transformation starts at 200^{o}C that marks the endothermic transition from γ-FeOOH to γ-Fe_2O_3 and an exothermic transition from γ-Fe_2O_3 to α-Fe_2O_3 at temperature of 430^{o}C [90].

In particular, γ-FeOOH has also exhibited good adsorption performance towards Se (VI) near neutral pH and at room temperature [91], although it appears that γ-FeOOH is thermodynamically metastable compared to other ferric oxyhydroxides [92-93]; but it has proven its significant contribution as functional materials for photocatalytic applications. However, most of the reports on γ-FeOOH are focused mainly on the synthesis, growth, and deposition of the material with their performance as good adsorbent and in photocatalytic process. For instance, γ-FeOOH nanoflakes were successfully synthesized using a simple solution method at 100^{o}C with ethylene glycol (EG) as mediator [88]. Furthermore, several studies have been reported to produce γ-FeOOH from aerial oxidation of $Fe(OH)_2$ in aqueous solution. Depending on the reaction temperature, oxidation rate, initial concentration of the reactants and pH of the solution, a mixture of Fe_3O_4, α-FeOOH, and γ-FeOOH can be obtained from the oxidation of $Fe(OH)_2$ [94]. Hence, the control of one or more of these parameters is necessary to produce pure γ-FeOOH. Additionally, aerial oxidation of neutral or slightly alkaline suspension containing $Fe(OH)_2$ would yield an intermediate green complex and solid green rust (GRI and GRII). The formation of GRI and GRII depends on the anion added to prepare the suspension, for instance, GRI and

GRII are formed when $FeCl_2$ and $FeSO_4$ are used as the starting materials, respectively. The formation of green rust as intermediate product is considered necessary to obtain pure γ-FeOOH through the process of air oxidation [95-98]. The detailed characteristics of the green rust are reported elsewhere.

The consideration of γ-FeOOH semiconductor properties has not been explored and reported yet. Thus, one of the objectives in this work is to investigate and gather experimental evidence that will elucidate and explain the semiconductor properties of γ-FeOOH fabricated via simplified electrodeposition method. The details of the employed process and results are presented in Chap. 7.

2.5 Chemical Deposition Techniques

Thin films can be prepared either with similar or different properties from their bulk counterparts. The thickness of the films plays significant role in distinguishing their potential applications. Selection process and parameters influence the structure and composition of the films, thereby altering their physical properties. Generally, different thin film deposition techniques involving simple to complicated processes can be utilized to prepare quality films. These methods can be classified into two main categories: (a) physical and (b) chemical techniques. The physical methods such vacuum thermal evaporation, sputtering, and molecular beam epitaxy (MBE) have been considered the sophisticated technique in obtaining high-purity films because of its complexity in the process and expensive equipment is needed to achieve the purpose. On the other hand, the chemical deposition techniques have been regarded as simple and inexpensive, but still effective methods to synthesize, grow or deposit quality thin films for a wide range of applications. Several chemical deposition methods are known and popular depending on the actual process or procedure in the film formation. Some of these chemical techniques are described and discussed in the following sections to differentiate their individual capacity in relation to thin film deposition (general perspective) and in oxide semiconductors fabrication (specific perspective).

2.5.1 Chemical Vapor Deposition (CVD)

Chemical vapor deposition is a versatile process suitable for manufacturing of coatings, powders, fibers, and monolithic components. CVD may be defined as the deposition of solid from a chemical reaction in the vapor phase, that is, it generally uses a gas-phase precursor, often a halide or hydride of the element to be deposited. With CVD it is possible to produce most metals, many non-metallic elements such as carbon (C) and silicon (Si) as well as a large number of compounds including carbides, nitrides, oxides, intermetallic and many others. Moreover, in CVD process, conformal and multi-directional depositions can be achieved. Several chemical reactions can happen during the CVD process that includes pyrolysis, reduction, hydrolysis, disproportionation, oxidation, carburization, and nitridation. These chemical reactions can occur singly or simultaneously during deposition [99].

Several versions of CVD processes have been developed to address the existing limitations of the conventional process. These are metal-organic CVD (MOCVD), low-pressure CVD (LPCVD), plasma enhanced CVD (PECVD), atomic layer CVD (ALCVD), ultra-high vacuum CVD (UVCVD), laser CVD (LCVD) and many others [99-100].

The development of MOCVD provides alternative options to produce thin films at lower temperature and pressure compared to conventional CVD. MOCVD only requires temperature that ranges from 573-1073 K and pressure varying from atmospheric to less than 1 Torr. Chemical precursors, usually metal-organic compounds, used in MOCVD are often commercially available. MOCVD reactions have been reported and investigated for the deposition of oxides such as tin oxide by oxidation of tetramethyl tin at 350-600^{o}C and reaction of {$(CH_3)_2SnCl_2$ with O_2 at 540^{o}C [101-103], and iron oxide by decomposition of $Fe(F_3C_5H_4)_3$ and $(C_5H_5)_2Fe$ in oxygen ambient at 300^{o}C and 400-500^{o}C, respectively [104].

CVD has several important advantages which make it the preferred process in many cases. Among these are (a) the line of sight deposition is not restricted, (b) deposition rate is high and thick coatings can be easily obtained, (c) CVD equipment does not normally require ultra high vacuum and generally can be adopted to many process variations, and (d) its flexibility that allows many changes in the composition during deposition. These reasons make the CVD process competitive and in some cases more economical than PVD. However, CVD has several disadvantages such as (i) it is most versatile at temperatures $600^{o}C$ and above, hence substrate selection is limited (many substrates are not thermally stable in this temperature range), (ii) the chemical precursors as starting materials with high vapor pressure are often hazardous, corrosive and extremely toxic at times, (iii) the by-products of CVD reactions such as CO, H_2 and HF are also toxic and corrosive, thus costly operations are necessary to neutralized these products, and (iv) compounds with sufficient purity are expensive.

2.5.2 Chemical Bath Deposition (CBD)

Chemical bath deposition (CBD) is one of the wet chemical methods available to grow semiconductor materials on solid surfaces (as substrates). The desired material to be deposited can be in the form of a thin film with a dense structure or porous-type structure. The films can be crystalline, amorphous, single phase or multi-phase. It is widely used to deposit non-metallic thin film compounds such as chalcogenides, oxides, halides, and carbonates through chemical reactions that occur in the solution bath. It is based on controlled chemical reaction producing the desired compound from chemical precursors dissolved in the solution.

CBD is based on chemical transformations of precursors and exchanged of define quantity during the reaction as opposed to the precipitation method, in which, the reactions occur from supersaturated solutions of the material to be deposited. This entity can be an electron, a chemical element or chemical group. Different CBD processes can be classified into three categories depending on the reactions involve in the formation of the thin film. The CBD classes, namely: (i) redox CBD - the reaction involves exchange of electrons, (ii) ligand exchange CBD – the reaction only involves ligand exchange, and (iii) complex reaction CBD, which involves decomposition of precursor species are identified and distinguished by simple general reactions illustrated and presented in details by Lincot et. al [105]. The growth of the film can also be obtained on the substrate surface either by ion by ion process or by aggregation of clusters (cluster growth) [106].

The advantages of CBD technique are low cost, large area deposition and relatively low deposition temperature. CBD is becoming an alternative deposition technique to produce thin films of compound materials like chalcogenides [107], oxides (TiO_2, ZrO_2, YtO_2, ZnO, VaO_2, SnO_2, Cu_2O) [108-118] and halides. Ion by ion growth mechanism is the most dominant mechanism for oxide materials produced by CBD. Additionally, a major success can be found in the recent period with the deposition of semiconducting cadmium sulfide (CdS) or zinc sulfide (ZnS) buffer or window layers in efficient copper indium diselenide (CISe) or cadmium telluride (CdTe) thin film solar cells.

However, CBD has some drawbacks that limit the quality of the grown or deposited thin films: (1) in the classical beaker configuration, the material yield during film formation is very low that can lead to an undesirable waste production, increased treatment time and production costs. The possible reason is that the formation of colloidal particles or precipitates usually occurs during deposition [107].

2.5.3 Spin-Coating or Sol-Gel Method

Spin-coating or sol-gel process (also known as soft chemistry) is another wet chemical technique to deposit thin films on a substrate (usually glass substrate or TCO coated-substrate). It is used primarily for the fabrication of materials starting from a chemical solution, which acts as the precursor for the formation of gel of either discrete particles or network polymers. Typical precursors are metal alkoxides and metal chlorides, which undergo various forms of hydrolysis and polycondensation reactions [119]. The sol-gel precursor is subsequently spun at a high speed (typically around 3000 rpm) to centrifugally spread the solution over the substrate. Various factors such as viscosity, drying rate, percent solids, and surface tensions are seriously considered to determine the terminal (final) thickness of the films. Deposition process can be repeated several times to increase the thickness of the desired films. Hence, this method involves a multi-step process in obtaining thicker samples. One of the most important factors in spin coating is repeatability. Any slight variations in the parameters that define the spin process can result in drastic change in the spin-coated film. Thermal treatment is often carried out in order to crystallize the amorphous spin coated film or to remove the excess solvent. Thin film preparation in sol-gel process can be summarized into three parts: (i) preparation of the precursor solution, (ii) deposition of the film from the prepared sol onto the chosen substrate, and (iii) heat treatment.

The sol-gel technique gains much interest in the field of thin films deposition due to the simplicity in performing the deposition, low processing temperature, stoichiometry control and its ability to produce uniform and chemically homogenous films over large areas. It is also feasible for doping process to be performed with ease. The sol-gel method has been successfully utilized for the preparation of various metal oxides such as ZnO [120-127], CuO [128], Cu_2O [129], and SnO_2 [130-133] that have shown potential characteristics for photovoltaic devices fabrication.

However, several disadvantages can be considered: (a) difficult to maintain purity, (b) multi-step process (which affects the reproducibility and productivity), (c) high-temperature process, (d) it requires costly chemicals, and (e) the preparation of the desired gel usually requires longer time for aging process to be completed (several hours to few days depending on the deposition conditions).

2.5.4 Spray Pyrolysis

Spray pyrolysis (SP) technique has been one of the major processing methods considered in the preparation and deposition of thin and thick films, ceramic coatings, and powders. Spray pyrolysis does not require high-quality substrates or chemicals. The method has been employed for the deposition of dense films, porous films, and for powder production. Owing to its versatility, multilayered films can be easily prepared and achieved [134]. Spray pyrolysis has been utilized for several decades in the glass industry [135] and in solar cell production [136]. The prime requisite for obtaining quality thin film is the optimization of preparative conditions such as substrate temperature, spray rate, concentration of solution and others. It has been observed that the properties of thin films strongly depend on the preparative conditions. Hence, tailoring the thin film properties can be made possible by adjusting or optimizing these conditions [137].

Typical spray pyrolysis equipment consists of an atomizer, precursor solution, substrate heater, and temperature controller. Thin film deposition using spray pyrolysis can be divided into three main steps: (i) atomization of the precursor solution, (ii) transportation of the resultant aerosol, and (iii) decomposition of the precursor on the substrate [134].

Various thin films-based materials have been chemically deposited by spray pyrolysis. These include metal oxides such as undoped and fluorine-doped SnO_2 [138-139], Cu_2O [108, 140], zinc oxide (ZnO) [141-143], and Ga_2O_3 [144] and sulfides such as tin sulfide (SnS) [145-147] and zinc sulfide (ZnS) [148].

2.5.5 Photochemical Deposition (PCD)

Photochemical deposition (PCD) technique gains attention in the field of thin film technology because of its simplicity to deposit very thin films depending on the substrate and the reaction conditions, which utilize direct irradiation from ultraviolet light source to activate the reaction on the substrate. It has been reported and demonstrated that electrons maybe promoted to excited states through photon absorption. Two possible methods that describe the deposition of thin films via PCD technique, these include: (1) thin film is being deposited by irradiation onto the substrate, which is immersed in a solution during the entire deposition process and (2) a small amount of solution that is dropped on top of the horizontally-positioned substrate and subsequently irradiated by a light source (an ultra-high pressure - 500 W - mercury arc lamp). The details of the PCD process are explained and described by A. Dengbaoleer [38]. Deposition parameters such as concentrations of working solution, deposition time, intensity of irradiation, and immersion depth can be varied to produce high quality thin films. Various sulfides (such as ZnS, Cu_xS_y, and GaS_xO_y) and selenides [149-154] have been deposited using this approach.

Accordingly, PCD technique is relatively simple and inexpensive method to produce thin films with better controllability and also capable for large area deposition. Several advantages of PCD can be considered: (1) low temperature deposition, (2) any substrate can be used, (3) reaction can be controlled by optical modulation, (4) simple process, and (5) broad range of chemical precursors can be utilized. However, deposition issues such as low deposition rate and difficulty in controlling the substrate position that affects the film thickness [154] cannot be ignored and disregarded during photochemical deposition. Modification of the set-up may solve these problems or issues.

2.5.6 Electrodeposition (ED)

Electrodeposition (ED) has been widely used as simple and inexpensive method to produce or deposit quality thin films with micro- and nano-structures at room or elevated temperatures. Serious scientists and technologists are still fascinated and excited with this method because it offers remarkable surprises in the atomic level and exceptionally versatile that makes it more attractive for wide range of applications. It has been considered as a technology for the future [155].

Basically, the film is deposited on an electrically conducting substrates (with flat or complex surfaces), which is immersed in the solution/electrolytes containing ions (cations and anions). Generally, gas (oxygen, nitrogen or argon) bubbling is also carried out either to eliminate undesired oxygen in the film for sulfide-based materials electrodeposition or to facilitate the deposition of metal oxide films onto the substrate from an oxygen-bubbled solution (dissolved oxygen serves as the oxygen precursor). The electrochemical reaction that occurs at the electrode-electrolyte interface is the main attraction in the electrodeposition process.

The electrode reaction is a heterogeneous reaction occurring only at the electrode-electrolyte interface. This includes: (1) diffusion, migration and convection of metal ion to the electrode surface, (2) ion adsorption at the surface by an electron discharge reaction, and (3) the growth of the deposit which may involve solid state diffusion processes. Either one or many of these can limit the rate of deposition process. The simplest reactions involve only mass transfer of a reactant to the electrode, electron transfer involving non-adsorbed species, and the mass transfer of the product to the bulk solution. When a steady-state current is obtained, the rates of all reaction steps in a series are the same. The rate determining steps can be determined from the magnitude of this current which is often limited by the inherent sluggishness of one or more reactions.

The electrode reaction can be represented by the movement of the free electrons in the conduction zone in the form of wave motion according to the band theory of metal. The reaction involves movement of free electrons at extremely rapid rate equal to the speed of light and random movement of ions in the electrolyte at normal temperature. Moreover, when the electrode is polarized by applying external potential, a local depletion of available species can be observed. This is because the diffusion of species from the bulk solution to the interface is extremely sluggish compared to the electron movement in the conductor. Since the regeneration of the species near the electrode is slow, the current density is reduced. Stirring the solution or inert gas purging can help the transport of the species from the solution bulk to the interface [156].

It is important to note also that in practical electrodeposition metal ions cannot be expected to be deposited as continuous layer or sheet from one edge of the electrode to the other. Rather, metal ions become attached to the electrode at certain favored sites. This can possibly lead to different forms of discontinuities such as pores, cracks, non-uniformities or other irregularities [157].

The process involves in the electrochemical system can be classified into two categories: (1) galvanostatic and (2) potentiostatic processes. In the former, a constant current is applied into the system, while in the latter, a constant potential (DC) or a periodic potential (two- or three-step potential, pulsed-ED). Potential values in (2) can be varied to control the physical, morphological, compositional, and structural properties of the deposit. Other electrochemical parameters such as deposition time, temperature, and pH are also essential factors to be considered in the deposition. In pulse-ED, potential values and duration of each potential step have significant role in controlling the properties of the deposits. Meanwhile, the current density in (1) plays a crucial role in obtaining good quality thin films. The electrodeposit can have undesired impurities depending on the applied current density.

Figure 2.5 shows the schematic diagram of the electrodeposition system used to deposit *n-type* transparent oxide and *p-type* semiconductor thin films. The system is mainly composed of three-electrode cell: {working electrode (WE), reference electrode (RE), and counter electrode (CE)}, function generator and potentiostat or galvanostat controller. Saturated calomel electrode (SCE) is used as the reference electrode and immersed in a saturated potassium chloride (KCl) solution. The three electrodes are connected to the potentiostat or galvanostatic controller. In typical three-electrode ED shown in Fig. 2.5, the applied potential is usually measured with respect to the reference electrode (SCE is used in this work). The essential role of the reference electrode is to establish a relatively stable potential in the considered electrochemical system throughout the deposition process. Different types of reference electrodes can be utilized in ED method. Commonly used reference electrodes are Ag/AgCl, Hg/HgCl, H_2/Pa, and SCE.

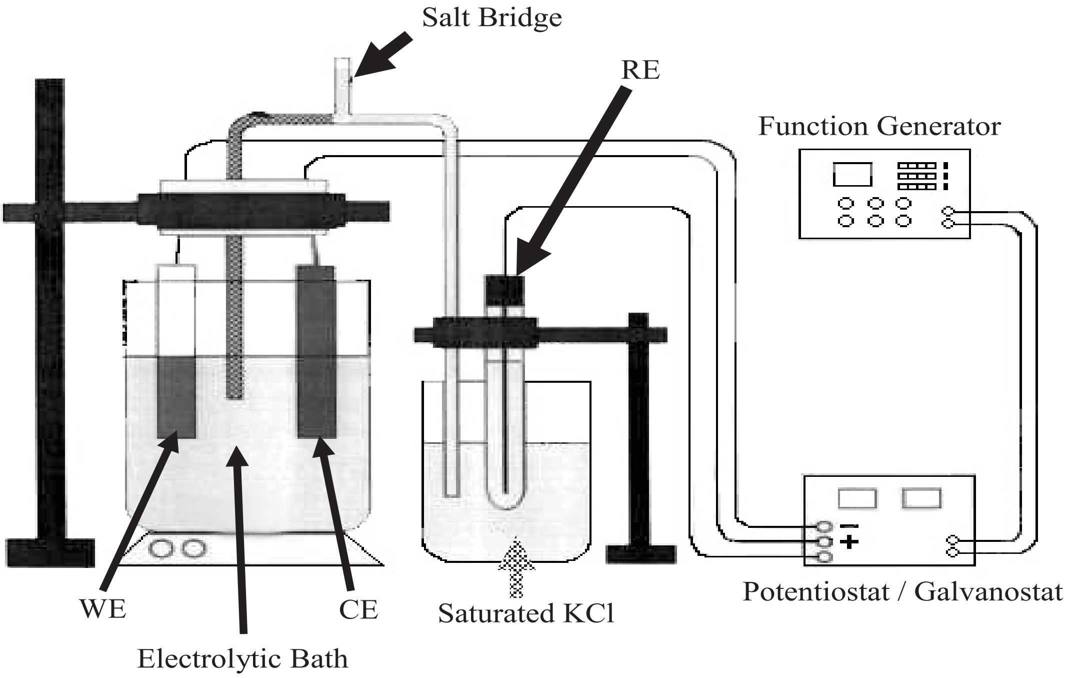

Fig. 2.5 Schematic diagram of the main components in the three-electrode electrochemical cell system.

The versatility of ED has shown wonders in thin film deposition, that is, from appealing colorful metal coatings to continuous layer of micro- and nano-structured semiconducting thin films. Various semiconducting thin film materials such as metal oxides, sulfides, selenides and tellurides can be produced by employing facile ED process near or at room temperature. For instance, successful electrodeposition of strongly adherent ZnO thin films has been achieved by several researchers from aqueous solution at room temperature and at elevated temperature of 60-

80°C with the help of dissolved oxygen, nitrate ions, and hydrogen peroxide (H_2O_2) as oxygen precursors [158-162]. Furthermore, electrodeposition of Cu_2O films has been reported to be successful at slightly higher temperature of 40-65°C in basic aqueous solutions [163-165]. In fact, Katayama et al. and Ichimura et al. have also reported and demonstrated that the fabrication of heterojunction solar cells made up of Cu_2O and ZnO thin films can be achieved by employing electrodeposition technique as step by step process in depositing each layer [165-167]. Other reports on successful fabrication of heterojunction solar cells by ED include InS_xO_y-SnS heterostructure with both layers deposited at room temperature as studied by Abdel Haleem [119]. These reports provide additional experimental proofs of the flexibility and simplicity of ED method.

References

[1] T. J. Clough, V. L. Grosvenor, and N. Pinsky: US Patent 5317132 (1994).

[2] A. Mukherjee: US Patent 4959257 (1990).

[3] S. Kim, J.-W. Chung, H. Lee, J. Park, Y. Heo, and H.-M. Lee: Sol. Energy Mater. Sol. Cells **119** (2013) 26.

[4] P. J. van der Put: *The Inorganic Chemistry of Materials: How to Make Things Out of Elements* (A Division of Plenum Publishing Corporation, New York, 1998) Chap. 10 Sec. 10.3.1.

[5] K. H. Houng: Bull. Inst. Chem., Acad. Sin. **29** (1982) 19.

[6] R. Gazdag, E. Seyfried, and Z. Ligeti: Adv. Liq. Cryst. Res. Appl. Proc. Liq. Cryst. Conf. Soc. Countries, **3** (2) (1981) 1137.

[7] J. Kane and M. Ling: US Patent 4728581 (1988).

[8] F. Berger, E. Beche, R. Berjoan, D. Klein, A. Chambaudet: Appl. Surf. Sci. **93** (1996) 9.

[9] K. H. Kim and C. G. Park: J. Electrochem. Soc. **138** (8) (1991) 2408.

[10] F. Dimeo Jr., S. Semancik, R. E. Cavicchi, J. S. Suehle, P. Chaparala, and N. H. Tea : Mater. Res. Soc. Symp. Proc. **415** (1996) 231.

[11] J. R. Brown, M. T. Cheney, P. W. Haycock, D. J. Houlton, A. C. Jones, and E. W. Williams: J. Electrochem. Soc. **144** (1) (1997) 295.

[12] R. G. Gordon, J. Proscia, F. B. Ellis Jr., and A. E. Delahoy : Sol. Energy Mater. **18** (1989) 263.

[13] R. Plättner, W. Stetter, and P. Köhler: Siemens Forsch.- u. Entwick.-Ber. **17** (3) (1988) 138.

[14] B. T. Boiko, G. I. Kopach, N. P. Klochko, V. R. Kopach, G. S. Khripunov, and A. I. Chernikov: Appl. Sol. Energy **26** (5) (1990) 40.

[15] A. Greenwald, J. Bragagnolo, and M. Leonard: Conf. Rec. IEEE Photovoltaic Spec. Conf. 19th (1987) 621.

[16] A. K. Saxena, S. P. Singh, and O. P. Agnihotri : Sol. Cells **19** (2) (1986) 163.

[17] K. Sato, Y. Gotoh, Y. Hayashi, K. Adachi, and H. Nishimura, Reports Res. Lab. Asahi Glass Co., Ltd. 1990, 40 (2), 233.

[18] K. Singh and R. Y. Tamakloe: Sol. Energy **56** (4) (1996) 343.

[19] M. Nakagawa, T. Amano, and S. Yokokura : J. Non-Cryst. Solids **218** (1997) 100.

[20] G. H. Lindner: US Patent 4737388 (1988).

[21] P. F. Gerhardinger and R. J. McCurdy: Mat. Res. Soc. Symp. Proc.**426** (1996) 399.

[22] G. A. Neumann and R. L. Stewart-Davis: US Patent 5395698 (1995).

[23] M. J. Soubeyrand and A. C. Halliwell: US Patent 5698262 (1997).

[24] P. R. Athey, D. S. Dauson, D. E. Lecocq, G. A. Neuman, J. F. Sopko, and R. L. Stewart-Davie: US Patent 5464657 (1995).

[25] R. D. Goodman, W. M. Greenberg and P. J. Tausch: US Patent 4847157 (1989).

[26] V. A. Henery: US Patent 4853257 (1989).

[27] D. J. Middleton and J. I. Grenier: US Patent 4548836 (1985).

[28] T. J. Coutts, X. Li, and T. A. Cessert: J. Vac. Sci. Technol. **B2** (1984) 140.

[29] T. J. Coutts, X. Li, and T. A. Cessert: IEEE Electron Lett. **26** (1990) 660.

[30] J. W. Gardener, H. V. Shurmer, and P. Corcoran: Sensors & Actuators **B4** (1991) 117.

[31] S. Mishra, C. Ghanshyam, N. Ram, S. Singh, R. P. Bajpai and R. K. Bedi: Bull. Mater. Sci. **25** (3) (2002) 231.

[32] A. M. B. van Mol: *Chemical Vapour Deposition of Tin Oxide Thin Films*, **Ph.D. Thesis** (2003) & references therein.

[33] A. Dengbaooler and M. Ichimura: Solid-State Electronics **69** (2012) 1.

[34] M. Ichimura, A. Baoleer, and T. Sueyoshi: Phys. Stat. Solidi C **7** (3-4) (2010) 1168.

[35] A. Dengbaooler and M. Ichimura: J. Non-crystalline Solids **358** (2012) 2470.

[36] A. Dengbaooler and M. Ichimura: IEEJ Trans. Fundamental Mat. **133** (1) (2013) 28.

[37] A. Dengbaooler and M. Ichimura: Trans. Mat. Res. Soc. Japan **37** (3) (2012) 377.

[38] A. Dengbaooler: Photochemical Deposition of SnO_2 Thin Films for Hydrogen Sensor Application, **Ph.D. Thesis** (2013).

[39] G. Korotcenkov, V. Brinzari, and I. Boris: J. Mater. Sci. **43** (2008) 2761.

[40] A. M. Bernardus van Mol: *Chemical Vapor Deposition of Tin Oxide Thin Films*, **Ph.D. Thesis** (2003).

[41] A. K. Ghosh, C. Fishman and T. Feng: J. Appl. Phys. **50** (1979) 3454.

[42] R. Sigh, K. Rajkanan, D. E. Brodie, and J. H. Morgan: IEEE Trans. Electron Devices **27** (1980) 656.

[43] J. Shewchun, D. Burk, and M. B. Spitzer: IEEE Trans. Electron Devices **27** (1980) 705.

[44] M. S. Tomar and F. J. García: Prog. Cryst. Charact. **4** (3) (1981) 221.

[45] F. J. García and J. Muci: Thin Solid Films **97** (1982) 51.

[46] J. A. Ayllon and M. Lira-Cantu: Appl. Phys. A **95** (2009) 249.

[47] F. So, J. Kido, and P. Borrows: Mater. Res. Soc. Bull. **33** (2008) 663.

[48] N. A. Anderson, E. Hao, X. Ai, G. Hastings, and T. Lian: Physica E Low-Dimens. Syst. Nanostruct. **14** (2002) 215.

[49] M. A. Mäki-Jaskari and T. T. Rantala: Physical Review B **65** (2002) 245428.

[50] M. Batzil, A. M. Chaka, and U. Diebold: Europhys. Lett. **65** (2004) 61.

[51] W. Bergermayer and I. Tanaka: App. Phys. Lett. 84 (2004) 909

[52] M. Batzil and U. Diebold: Progress in Surface Sci. **79** (2003) 47.

[53] Y. Muraoka, N. Takubo, and Z. Hiroi: J. Appl. Phys. **105** (2009) 103702.

[54] Z. M. Jarzebski and J. P. Marton: J. Electrochem. Soc. **123** (1976) 199C.

[55] J. A. Kohn, G. Katz, and J. D. Broder: Am. Mineral. **42** (1957) 398.

[56] S. Geller: J. Chem. Phys. **33** (1960) 676.

[57] L. Pauling: *Nature of the Chemical Bond* (Cornell University Press, Ithaca, New York, 1960) 3rd ed. Chap. 13, Sec. 6.

[58] L. M. Foster and H. C. Stumpf: J. Am. Chem. Soc. **73** (1951) 1590.

[59] L. Binet, D.Gourier, and C. Minot: J. Solid State Chem. **113** (1994) 420.

[60] M. Orita, H. Ohta, M. Hirano, and H. Hosono: Appl. Phys. Lett. **77** (25) (2000) 4166.

[61] R. Jalilian, M. M. Yazdanpanah, B. K. Pradhan, and G. U. Sumanasekera: Chem. Phys. Lett. **426** (2006) 393.

[62] M. Ogita, K. Higo, Y. Nakanishi, and Y. Hatanaka: Appl. Surf. Sci. **175-176** (2011) 721.

[63] M. Fleischer and H. Meixner: Sens. Actuators B **4** (1991) 437.

[64] S. Nakagomi, M. Kaneko, and Y. Kokubun: Sens. Lett. **9** (1) (2011) 35.

[65] S. Nakagomi, M. Ikeda, and Y. Kokubun: Sens. Lett. **9** (2) (2011) 616.

[66] S. Nakagomi, T. Momo, S. Takahashi, and Y. Kokubun: Appl. Phys. Lett. **103** (2013) 072105.

[67] B. Zhao and P. Zhang: Catalysis Comm. **10** (2009) 1184.

[68] Y. D. Hou and M. A. A. Schoonen: Am. Mineral **85** (2000) 543.

[69] T. Sato and T. Nakamura: Thermochimica Acta **53** (1982) 281.

[70] S. Fujihara, Y. Shibata, and E. Hosono: J. Electrochem. Soc. **152** (11) (2005) C764.

[71] A. Klug and L. Farkas: Phys. Chem. Miner. **7** (1981) 138.

[72] A. C. Tas, P. J. Majewski, and F. Aldinger: J. Am. Ceram. Soc. **85** (2002) 1421.

[73] H. K. Lee, D. H. Joo, M. S. Kim, and J. S. Yu: Nanoscale Res. Lett. **7** (2012) 458.

[74] J. Qiu, M. Guo, and X. Wang: ACS Appl. Mater. Interfaces **3** (2011) 2358.

[75] J. Lee and Y. Tak: Electrochem. Solid-State Lett. **4** (9) (2001) C63.

[76] M. Izaki and T. Omi: J. Electrochem. Soc. **143** (1996) L53.

[77] W. Wang et al.: Catalysis Lett. **81** (1-2) (2002) 63.

[78] F. Shi et al.: J. Molecular Catalysis A: Chemical **292** (1-2) (2008) 28.

[79] R. Schrebler et al. : Electrochem. Solid-State Lett. **9** (7) (2006) C110.

[80] A. B. Murphy, P. R. F. Barnes, L. K. Randeniya, I. C. Plumb, I. E. Grey, M. D. Horne, and J. A. Glasscock: Int. J. Hydrogen Energy **31** (2006) 1999.

[81] Ref. [79] & references therein

[82] W. A. A. T. Sayed Ahmed: *Hydrogen Production by Ethanol Partial Oxidation over Nano-Iron Oxide Catalyst Produced by Chemical Vapour Synthesis*, **Ph.D. Thesis** (2011).

[83] J. E. Greedon: *Magnetic Oxides: Encyclopedia of Inorganic Chemistry* (R. Bruce King, John and Wiley Sons, New York, 1994) ISBN 0-471-93620-0.

[84] C. E. Housecroft and A. G. Sharpe: *Chapter 22: d-block metal chemistry: the first row elements: Inorganic Chemistry* (Pearson, 2008) **3ed**. ISBN 978-0-13-175553-6.

[85] Shmakov et al: J. Appl. Crystallography **28** (1995) 141

[86] Y. Mamindy-Pajany, C. Hurel, N. Marmier and M. Romeo: C. R. Chim. **12** (2009) 876.

[87] M. Jonsson, P. Persson, S. Sjoberg, and J. S. Loring: Environ. Sci. Technol. **42** (2008) 2464.

[88] Y. Jia, T. Luo, X.-Y. Yu, Z. Jin, B. Sun, J.-H. Liu, and X.-J. Huang: New J. Chem. (2013).

[89] K. Norén, J. S. Loring, and P. Persson: J. Colloid Interface Sci. **319** (2) (2008) 416.

[90] P. M. A. de Bakker, E. De Grave, R. E. Vanderghe, and L. H. Bowen: Hyperfine Interactions **54** (1990) 493.

[91] S. Das, M. J. Hendry, and J. Essilfie-Dughan: Appl. Geochem. **28** (2013) 185.

[92] J. Majzlan, L. Mazeina, and A. Navrotsky: Geochim. Cosmo-chim. Acta **71** (2007) 615.

[93] R. F. Chen, H. X. Chen, Y. Wei, and D. L. Hou: J. Phys. Chem. C **111** (2007) 16453.

[94] R. Lin, R. Spicer, F. L. Tungate, and B.H. Davis: Colloids and Surfaces A **113** (1-2) (1996) 79.

[95] M. Kiyama, N. Jikuhara, and T. Takada: Bull. Chem. Soc. Japan **46** (1973) 323.

[96] M. Kiyama and T. Takada: Bull. Chem. Soc. Japan **45** (1972) 1923.

[97] M. Kiyama, T. Akita, S. Shimizu, Y. Okuda and T. Takada: Bull. Chem. Soc. **45** (1972) 3422.

[98] M. Kiyama: Bull. Chem. Soc. Japan **47** (1974) 1646.

[99] H. O. Pearson: *Handbook of Chemical Vapor Deposition (Principles, Technology and Applications)*, **2ed.** (Noyes Publications/William Andrew Publishing LLC 1999) 25.

[100] D. L. Smith: *Thin Film Deposition: Principles and Practice*, (McGraw-Hill Professional, 1995).

[101] C. G. Borman and R. G. Gordon: J. Electrochem. Soc. **136-12** (1989) 3820.

[102] C. F. Wan, R. D. McGrath, W. F. Keenan, and S. N. Franck: J. Electrochem. Soc. **136-5** (1989) 1459.

[103] R. C. Gordon, J. Proscia, F. R. Ellis, and A. E. Delahoy: Solar Energy Mater. **18** (1989) 263.

[104] S. Yu-Sheng and Z. Yuying: *Proc. 10th Int. Conf. on CVD, (G. Cullen, ed.),* Electrochem. Soc. (1987).

[105] D. Lincot and G. Hodes: *Chemical Solution Deposition of Semiconducting and Non-metallic Films*, Electrochem. Soc. Proceedings **2003-32** (2006) 1.

[106] Ref. **[105]** & references therein.

[107] M. Muhibbullah: *Deposition of Copper Oxide Thin Films by Chemical Techniques*, **Ph.D. Thesis** (2012)

[108] J. Emerson-Reynolds: J. Chem. Soc. **45** (1884) 162.

[109] M. Froment, M. C. Bernard, R. Cortes, B. Mokili, and D. Lincot: J. Electrochem. Soc. **142** (1995) 2642.

[110] T. Saeed and P. O'Brien: Thin Solid Films **27** (1995) 351.

[111] H. Shin, R. J. Collins, M. R. DeGuire, A. H. Heuer, and C. N. Sukenik: J. Mater. Res. **10**

(1995) 692.

[112] M. Izaki and T. Omi: J. Electrochem. Soc. **144** (1997) L3.

[113] M. Agarwal, M. R. DeGuire, and A. H. Heuer: J. Am. Ceram. Soc. **80** (1997) 2967.

[114] H. Nagayama, H. Honda, and H. Kawahara: J. Electrochem. Soc. **138** (1988) 2013

[115] D. Raviendra and J. K. Sharma: Phys. Chem. Solids **46** (1985) 945.

[116] J. Ino, A. Hishinuma, H. Nagayama, and H. Kawahara: US Patent 4, 882 (1989) 183.

[117] S. Deki, Y. Aoi, Y. Miyake, A. Gotoh, and A. Kajinami: Mater. Research Bull. **31** (1996) 1399.

[118] I. Grozdanov: Mater. Lett. **19** (1994) 281.

[119] A. M. Abdel Haleem Hassan: *Electrochemical Deposition of InS-based Thin Films for Photovoltaic Applications*, **Ph.D. Thesis (**2010) & references therein.

[120] C. Shaoqiang, Z. Jian, F. Xiao, W. Xiaohua, L. Laiqiang, S. Yanling, X. Qingsong, W. Chang, Z. Jianzhong, and Z. Ziqiang: Appl. Surf. Sci. **241** (2005) 384.

[121] T. Okamura, Y. Seki, S. Nagakari, and H. Okushi: Jpn. J. Appl. Phys. **31** (1992) L762.

[122] Y. Ohya, H. Saiki, and Y. Takahashi: J. Mater. Sci. **29** (1994) 4099.

[123] M. Ohyama, H. Kozuka, T. Yoko, and S. Sakka: J. Ceram. Soc. Jpn. **104** (1996) 296.

[124] D. Bao, H. Gu, and A. Kuang: Thin Solid Films **312** (1998) 37.

[125] L. Znaidi, G.J.A.A. Soler Illia, R. Le Guennic, C. Sanchez, and A. Kanaev : J. Sol–Gel Sci. Technol. **26** (2003) 817.

[126] L. Znaidi, G.J.A.A. Soler Illia, S. Benyahia, C. Sanchez, and A.V. Kanaev : Thin Solid Films **428** (2003) 257.

[127] S. Ben Yahia, L. Znaidi, A. Kanaev, and J. P. Petitet: Spectrochim. Acta Part A **71** (2008) 1234.

[128] S. Saadat Niavol and F. E. Ghodsi: Rus. J. Phys. Chem. A **87** (1) (2013) 84.

[129] R. Abd-Shukor, R. Awang, M. Deraman, M. M. Kamisah and R. Shamsudin: Adv. Mater. Res. **501** (2012) 247.

[130] A. Fukuda and M. Ichimura: Mater. Sci. Applications **4** (2013) 1.

[131] S. Shukla, S. Patil, S. C. Kuiry, Z. Rahman, T. Du, L. Ludwig, C. Parish, and S. Seal: Sens. Actuators B **96** (1-2) (2003) 343.

[132] S.-S. Park and J. D. Mackenzie: Thin Solid Films **274** (1996) 154.

[133] G. Sakai, N. S.Baik, N. Miura, and N. Yamazoe: Sens. Actuators B **77** (2001) 116.

[134] D. Perednis and L. J. Gauckler: J. Electroceram. **14** (2005) 103.

[135] J. M. Mochel: US Patent 2564707 (1951).

[136] J. E. Hill and R. R. Chamberlain: US Patent 3148084 (1964).

[137] P. S. Patil: Mater. Chem. Phys. **59** (3) (1999) 185.

[138] W. M. Sears and M. A. Gee: Thin Solid Films **165** (1) (1988) 65.

[139] M. A. Sánchez-García, A. Maldonado, L. Castañeda, R. Silva-González, and M. dela Luz Olvera: Mater. Sci. Applications **3** (2012) 690.

[140] T. Kosugi and S. Kaneko: J. Amer. Ceram. Soc. **81** (12) (1998) 3117.

[141] N. Lehraki, M. S. Aida, S. Abed, N. Attaf, and M. Poulain: Current Appl. Phys. **12** (5) (2012) 1283.

[142] M. Quintana, E. Ricra, J. Rodŕiguez and W. Estrada: Catalysis Today **76** (2-4) (2002) 141.

[143] R. S. Gaikwad, G. R. Patil, M. B. Shelar, B. N. Pawar, R. S. Mane, S. H. Han, and O. S. Joo: Int. J. Self-Propagating High-Temperature Synthesis **21** (3) (2012) 178.

[144] J. Hao and M. Cocivera: J. Phys. D: Appl. Phys. **35** (2002) 433.

[145] B. Thangaraju and P. Kaliannan: J. Phys. D: Appl. Phys. **33** (2000) 1054.

[146] N. Koteswara Reddy, K. T. Ramakrishna Reddy, G. Fisher, R. Best and P. K. Dutta: J. Phys. D: Appl. Phys. **32** (1999) 988.

[147] T. H. Sajeesh, K. B. Jinesh, M. Rao, S. Kartha, and K. P. Vijayakumar: Phys. Stat. Solidi **209** (7) (2012) 1274.

[148] O. Mustafa, M. Bedir, S. Ocak, and R. G. Yildrim: J. Mater. Sci. Mater. Electron. **18** (5) (2007) 505.

[149] F. Goto, M. Ichimura, and E. Arai : Jpn. J. Appl. Phys. **36** (1997) L1146.

[150] M. Ichimura, F. Goto, Y. Ono, and E. Arai : J. Cryst. Growth **198-199** (1999) 308.

[151] M. Ichimura, A. Nakamura, K. Takeuchi, and E. Arai : Thin Solid Films **384** (2001) 157.

[152] J. Podder, R. Kobayashi, and M. Ichimura : Thin Solid Films **472** (2005) 71.

[153] R. Kumaresan,M. Ichimura, and E. Arai : Thin Solid Films **414** (2002) 25.

[154] S. Chowdhury and M. Ichimura: Jpn. J. Appl. Phys. **49** (2010) 062302.

[155] W. Schwarzacher: The Electrochem. Soc. Interface (2006) 32.

[156] A. J. Bard and L. R. Faulkner: *Electrochemical Methods: Fundamentals and Applications*, **2ed**. (John Wiley & Sons, Inc. 2001) 228-231.

[157] M. Paunovic and M. Schlesinger: *Fundamentals of Electrochemical Deposition*, **3ed.** (John Wiley & Sons, Inc. 2006) 211-212.

[158] S. Peulon and D. Lincot: Adv. Mater. **8** (2) (1996) 166.

[159] S. Peulon and D. Lincot: J. Electrochem. Soc. **145** (1998) 864.

[160] A. I. Inamdar, S. H. Mujawar, S. B. Sadale, A. C. Sonavane, M. B. Shelar, P. S. Shinde, and P. S. Patil: Sol. Energy Mater. Sol. Cells **91** (2007) 864.

[161] J. Lee and Y. Tak: Electrochem. Solid-State Lett. **4** (9) (2001) C63.

[162] D. Ramírez, D. Silva, H. Gómez, G. Riveros, R. E. Marotti, and E. A. Dalchiele : Sol. Energy Mater. Sol. Cells **91** (2007) 1458.

[163] J. A. Switzer, C.-J. Hung, L.-Y. Huang, F. S. Miller, Y. Zhou, E. R. Taub, M. G. Shumsky and E. W. Bohannan: J. Mater. Res. **13** (1998) 909.

[164] T. D. Golden, M. G. Shumsky, Y. Zhou, R. A. V. Werf, R. A. V. Leeuwen, and J. A. Switzer: Chem. Mater. **8** (1996) 2499.

[165] J. Katayama, K. Ito, M. Matsuoka, and J. Tamaki: J. Appl. Electrochem. **34** (2004) 687.

[166] M. Ichimura and Y. Song: Jpn. J. Appl. Phys. **50** (2011) 051002.

[167] Y. Song and M. Ichimura: Jpn. J. Appl. Phys. **51** (2012) 10NC39.

CHAPTER 3

Electrodeposition and Characterization of SnO_2 Thin Films from Aqueous Tin Sulfate Solutions

(I. Oxygen Bubbling Employed During Deposition)

3.1 Introduction

Tin oxide (SnO_2) is an important semiconducting material and considered as one of the promising transparent conducting oxides (TCO) because of its wide direct band gap (~ 3.8 eV), large mobility, high conductivity, and high transparency in the visible region. It can also be used as a window layer in solar cell fabrication, an anode material for Li-ion batteries [1], and gas sensors [2-3]. Various techniques have been employed to fabricate tin oxide films such as chemical bath deposition [4], spray pyrolysis [5], sol-gel process [6], metal organic deposition [7], liquid flow deposition [8], and electrodeposition (electrochemical deposition). Electrodeposition is considered as one of the low-cost methods and an effective tool for solar cell fabrication. It can deposit considerably large area films on a complex surface. The surface morphology and composition of the films can also be controlled by electrochemical parameters. For electrodeposition of SnO_2 or any metal oxides, it is necessary to consider the source of oxygen precursor. Different kinds of oxygen precursor have been reported for the fabrication of metal oxide films (*e.g.*, ZnO, SnO_2), namely, nitrate ions [9], dissolved oxygen [10], and hydrogen peroxide [11]. For instance, nitrate ions contribute to the electrodeposition of ZnO following the reactions:

$$NO_3^- + H_2O + 2e^- \rightarrow NO_2^- + 2OH^-, \tag{3.1}$$

$$Zn^{2+} + 2OH^- \rightarrow Zn(OH)_2, \tag{3.2}$$

$$Zn(OH)_2 \rightarrow ZnO + H_2O. \tag{3.3}$$

However, the decomposition of $Zn(OH)_2$ to form ZnO in eq. (3) is remarkably slow at room temperature. Due to this reason, the deposition of ZnO films at elevated temperature, preferably 60^0C or above has been performed [12-13].

Hosono et al. reported highly porous and micro-patterned SnO_2 films by electrochemically assisted chemical bath deposition with overall reactions between tin ions and oxygen gas generated by an anodic applied potential [14],

$$Sn(OH)_4 + Sn(OH)_4 \leftrightarrow Sn_2O(OH)_6 + H_2O \leftrightarrow 2SnO_2 + 4H_2O. \qquad (3.4)$$

Chang *et al.* reported fabrication of nanostructured SnO_2 films by electrodeposition from a solution containing nitrate ions and at elevated temperature of 85°C [15]. Although electrodeposition of SnO_2 has been successfully carried out at elevated temperatures, to our knowledge, no studies have been reported regarding electrodeposition of SnO_2 from an oxygen-bubbled solution at room temperature. The present work aims to report and discuss the DC electrodeposition of SnO_2 from aqueous tin sulfate solution with very low pH (~ -0.03). The working solution was bubbled with oxygen to facilitate the formation of SnO_2 on the substrate. It was considered in Ref. 15 that SnO_2 is synthesized according to the reactions similar to reactions (1)-(3), but we propose a different deposition reaction in this study.

3.2 Experimental Details

SnO_2 films are deposited by using the conventional DC electrodeposition from an aqueous solution containing 30 mM $SnSO_4$ and 1.07 M HNO_3. The electrodeposition is performed in a conventional three-electrode electrochemical cell. An indium-tin-oxide (ITO) coated glass substrate, a platinum sheet, and a saturated calomel electrode (SCE) in a saturated potassium chloride (KCl) solution are utilized as the working, counter, and reference electrodes, respectively (the schematic diagram of the three-electrode electrochemical cell is presented and described in **Chapter 2**). During the deposition, the working solution is bubbled by oxygen at a rate of 0.5 L/min. After the deposition, all the samples are washed softly in water and naturally dried in air.

Pre-deposition Preparation

Prior to deposition, both the ITO substrate (with an area of 2.5 cm^2) and the platinum sheet are ultrasonically cleaned using alkyl benzene solution and deionized water, respectively. The pre-cleaned substrate and Pt sheet are then subsequently dried in N_2 gas. The deposition area is made by masking some portions of the ITO side of the substrate such that only 1 cm^2 area is exposed to the electrolyte during deposition. The entire glass side of the substrate is also masked to avoid some depositions on this region. Solution preparation is performed by dissolving $SnSO_4$ salt in deionized water and then HNO_3 is added to adjust the pH.

Film Characterizations

The as-deposited films are characterized by a double beam spectrometer for transmission studies (using the JASCO U-570 UV/VIS/NIR spectrometer with ITO substrate as the reference for the wavelength ranges from 300 to 1500 nm), photochemical (PEC) measurement (using the three-electrode electrochemical cell) for conductivity type and photosensitivity confirmation, X-ray diffraction (XRD) using RIGAKU RINT diffractometer equipped with monochromatic Cu $K_{\alpha 1}$ radiation at 40 kV and 30 mA for crystallinity study, Auger electron spectroscopy (AES) using JEOL JAMP 7800 Auger microprobe at probe voltage (10 kV) and current (2×10^{-8} A) for the composition study, scanning electron microscopy (SEM) using HITACHI S-2000S SEM model at an acceleration voltage of 10 kV for the surface morphology study and Accretech Surfcom-1400D profilometer for the thickness measurements.

3.3 Results and Discussion

3.3.1 pH optimization

Without nitric acid, $SnSO_4$ salt was not completely dissolved in water. At pH in a range 0.6 – 1.3, the salt was dissolved, but the solution became cloudy because of the precipitation of solid products during deposition. These solid products were avoided by adding a significant amount of nitric acid into the solution. The suitable pH (-0.03) was obtained by adding 1.07 M HNO_3 to avoid precipitation prior to and during deposition.

3.3.2 Cyclic voltammetry

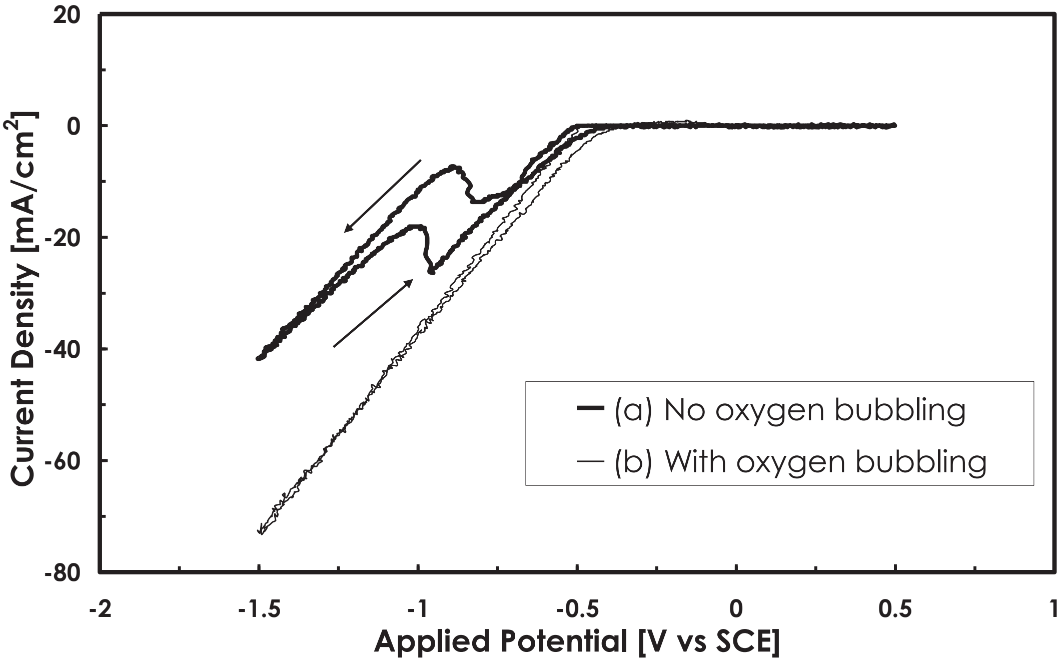

Fig. 3.1 Cyclic voltammetry curves recorded at the scan rate of 20 mV s^{-1} of 30 mM $SnSO_4$ and 1.07 M HNO_3 aqueous solution in the (a) absence and (b) presence of O_2 bubbling.

Cyclic voltammetry (CV) is an effective tool in analyzing the electrochemical process that involves in thin film deposition by electrodeposition method. The solution is prepared in the same manner of preparation for film deposition. The current response in the electrochemical system is measured and monitored with the application of a triangular potential scan. The typical electrochemical system utilized in this measurement is similar to the ED system shown in Fig. 2.5 (in **Chapter 2**). CV is usually considered as an initial step in ED to have insights on the possible redox reactions that can occur during film deposition. Reactions that can describe the deposition of the film can be identified in the obtained CV curve. The suitable reduction and oxidation potentials of a certain compound can be determined and analyzed by closely monitoring the measured current response. Essentially, the potential window for the electrodeposition of compound semiconductor materials such as tin oxides can be explicitly extracted from the CV curves (applied potential versus current response).

Figure 3.1 shows the cyclic voltammetry (CV) curves of (a) absence of O_2 bubbling and (b) presence of O_2-bubbling. The potential is scanned from 0 V, reversed at -1.5 to +0.5 V, and terminated at 0 V. All potential values are measured with respect to SCE. Without oxygen bubbling (curve a) as shown in Fig. 3.1, there is no electrochemical reaction observed for applied potentials between 0 and -0.5 V. From -0.5 to -1.5 V, an increase in cathodic current is attained. A well-defined cathodic peak is discernable at -0.83 V. From -0.83 to -0.90 V, a decrease in cathodic current is observed. The decrease in cathodic current is recovered at more negative potential (lower than -0.90 V). During the reverse scan, the current decreased rapidly up to -0.99 V followed by an increase up to -0.95 V and decreased again until it reaches zero value at -0.39 V. With the presence of oxygen bubbling (curve b), the reduction and oxidation peaks are not observed.

The difference in CV curves may imply that the film growth is enhanced with the aid of oxygen bubbling. The peak at -0.83 V in curve (a) would correspond to the deposition reaction of SnO_2. With the oxygen bubbling, the reduction current started to increase at a less negative voltage. This will be because the oxygen bubbling enhanced the SnO_2 deposition reaction and shifted the equilibrium potential so that the reaction started at less negative voltage. There is no discernable peak near -0.9 V with the oxygen bubbling. This could be due to stirring effects of the gas bubbling. In general, a peak appears in a CV curve because of the following reason: with increasing applied voltage, some reaction is activated and the current once increases, but the initially accessible species near the electrode will immediately discharge, leading to a local depletion of the species close to the electrode and the decrease in the current density. Thus, if the stirring enhances the supply of the ions from the solution bulk to the electrode, the peak can disappear. Similar cyclic voltammetry results are observed in slightly different solution conditions.

3.3.3. Deposition potential and time optimization

Applied potential (V)	Deposition time (min)	AES result (Sn/O)	Thickness (μm)
-0.9	7.5	0.565	~ 0.07
	10	0.61	~ 0.10

Table 3.1 Film thickness and composition ratio (Sn/O) for samples deposited at shorter times.

Try-test deposition is performed to obtain suitable potential and optimize deposition time. The applied potential values (-1.0, -0.9, and -0.8 V) employed in the try-test deposition are decided from the observed reduction peak without oxygen bubbling. Using these potential values and the considered solution with the presence of oxygen bubbling, thin continuous films with aggregated grains on the surface are obtained for 5 min deposition. For a relatively short deposition time performed in the try-test deposition, the occurrence of larger particle formation is favored compared with continuous film deposition at -1.0 V. Lesser particle formation is observed at -0.9 V than at -1.0 V. In this case, the continuous film growth is comparatively dominant as deposition time is extended. On the other hand, even though particle formation at -0.8 V was minimal, less deposition is observed, that is, the thickness of the continuous film is considerably small compared to -0.9 V. Due to these observations, -0.9 V is chosen to be the suitable potential for the electrodeposition of SnO_2 films from the oxygen-bubbled aqueous tin sulfate solution. This potential value is utilized to optimize deposition time necessary for the deposition of SnO_2 thin films with considerable thickness as a buffer layer for solar cell fabrication. Deposition time is varied from 7.5 to 35 min. For longer deposition time (20 and 35 min), white and thick films are obtained. Cracks are evident as viewed in the surface morphology of the deposited film. On the other hand, thin and transparent films are obtained from short time deposition (7.5 and 10 min). The thickness of the films is measured by profilometry and summarized in Table 3.1.

3.3.4 Effect of oxygen bubbling and temperature on the appearance of the film

In the absence of oxygen bubbling and at an applied potential of -0.9 V, a very thin and weak film is attained, that is, the film peeled off when washed softly in water. This observation could be associated with minimal presence of oxygen precursor and/or weak surface adhesion between the film and the substrate. On the other hand, the film did not peel when deposited with the aid of oxygen bubbling.

Deposition at relatively high temperature (~60^{o}C) was performed to investigate the effect of temperature on the appearance of the film. The film was deposited at a potential of -0.9 V for 10 min and oxygen was bubbled through the solution during deposition. The solution became cloudy because of the precipitation of solid products during deposition. The deposited film appeared white, thick and rough. This appearance is not suitable for window or buffer layers in solar cell fabrication, in which, the general requirement is as much as possible the layer must have high transparency to avoid photon absorption losses as it passes the layer. The observed precipitation did not occur when the deposition was performed at room temperature.

3.3.5 Surface morphology and structural studies

The surface morphologies of the as-deposited samples are shown in Fig. 3.2. Both samples have defined grains and good surface coverage. The samples are transparent as viewed by the naked eye but non-uniformity in the surface is apparent. This is maybe due to the aggregation of smaller particles forming larger nodules and these particles reside on top of the continuous thin film layer.

The crystal structure of the as-deposited SnO_2 sample deposited for 35 min is determined by X-ray diffraction shown in Fig. 3.3. Patterns (a) and (b) depict the diffraction patterns of the sample and the bare ITO-glass substrate, respectively. As shown in Fig. 3.3, a broad signal is observed and could be associated to SnO_2 (110) diffraction near $2\theta = 26°$. This broad peak indicates the possibility of either the amorphous-like or nanocrystalline structure of SnO_2. However, other than the broad peak that represents the diffraction of SnO_2, two unidentified sharp peaks were observed at 32 and 63.75^{o}. Further studies should be carried out to resolve the existence of the unknown peaks.

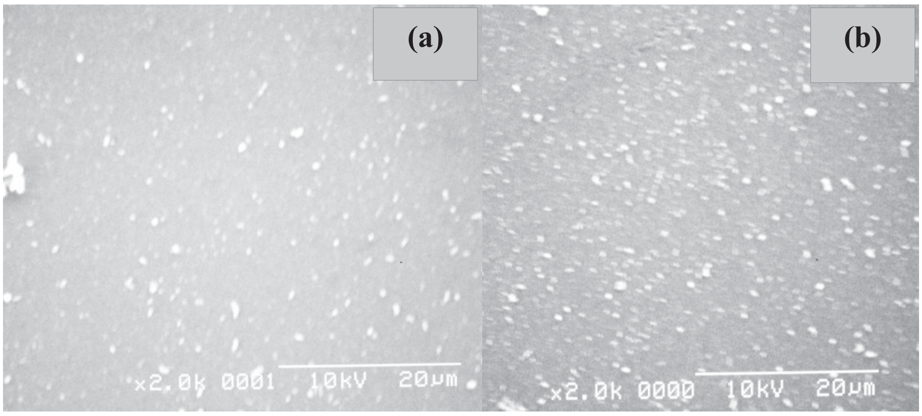

Fig. 3.2 SEM photographs of SnO_2 samples deposited for (a) 7.5 and (b) 10 min.

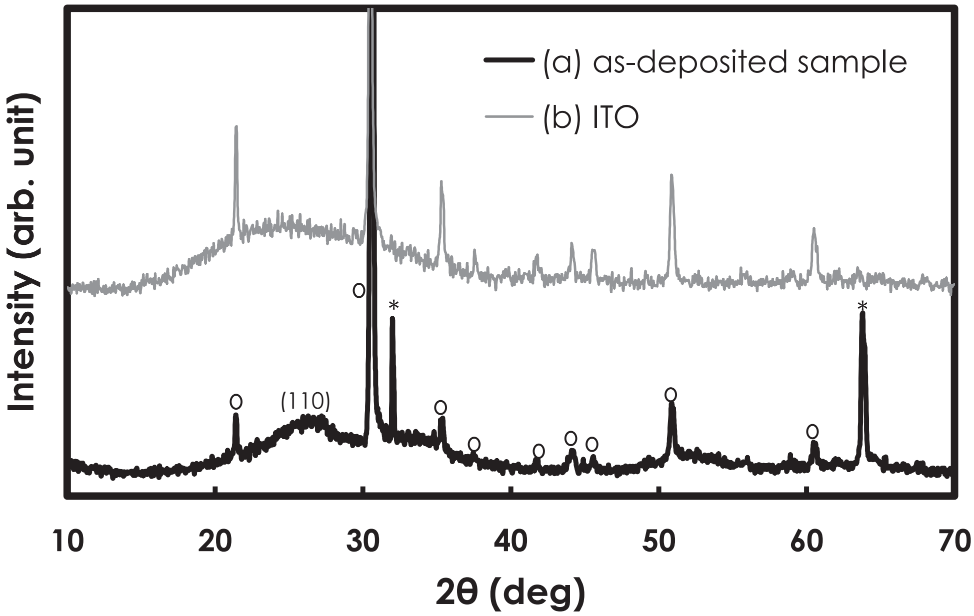

Fig. 3.3 XRD spectra of (a) as-deposited SnO_2 sample deposited for 35 min and (b) indium tin oxide (ITO). (Open circles and * denote ITO and unknown peaks, respectively.)

3.3.6 Composition studies

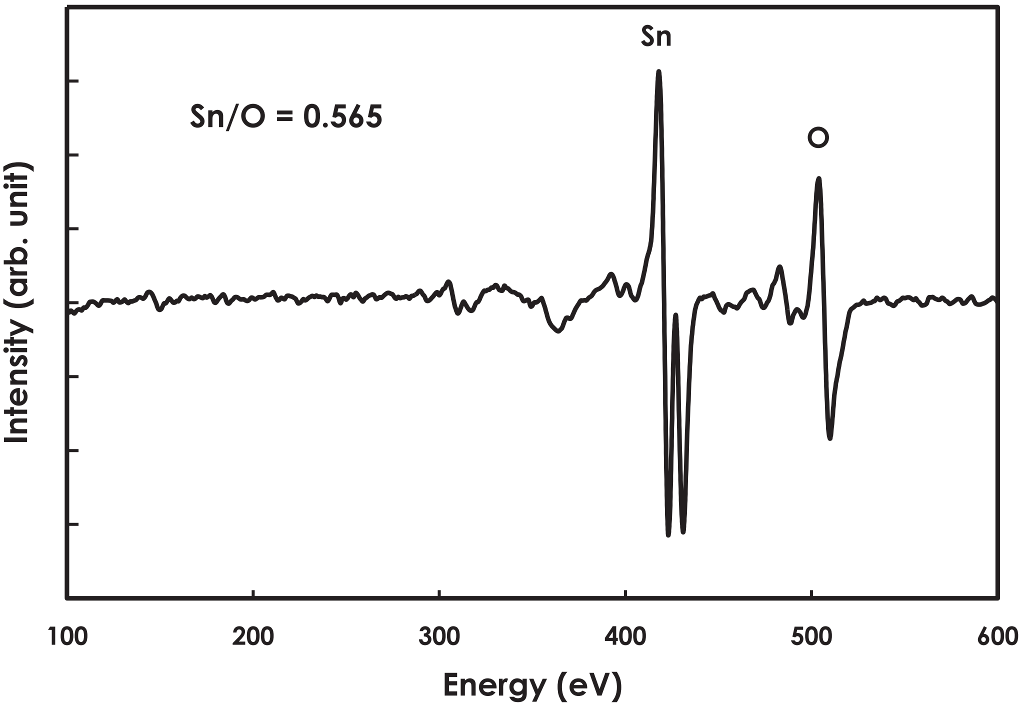

Fig. 3.4 AES spectrum for the as-prepared SnO_2 thin film deposited at -0.9 V for 7.5 min

Figure 3.4 shows the Auger electron spectrum of the Argon-sputtered sample deposited for 7.5 min. Impurities due to carbon contamination are removed after 5 s sputtering. The result confirms the presence of Sn and O Auger peaks with a ratio of Sn/O = 0.565, a 13% deviation from stoichiometric ratio. This ratio is calculated by using the Auger spectrum of fluorine-doped SnO_2 as a standard. As portrayed in the SEM photographs, particles are observed on the surface of a continuous film. The Auger spectra of these particles are also measured to verify their composition. However, no significant difference is found in the composition ratios when the electron beam is illuminated on these particles or illuminated on the background area. For 10 min deposition, Sn and O peaks are also clearly observed in the Auger spectrum as shown in Fig. 3.5. The calculated Sn/O ratio for this sample is 0.61; a 22% deviation from stoichiometry is obtained.

Considering the accuracy of the AES analysis and the obtained Sn/O ratios, we may conclude that the deposited films were slightly Sn-rich films.

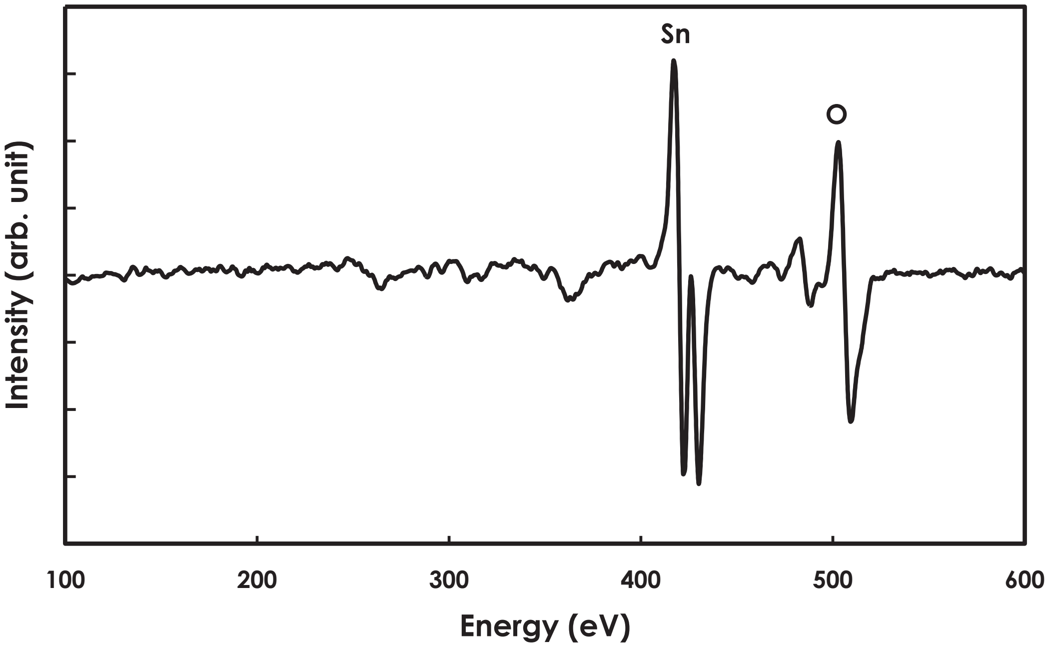

Fig. 3.5 AES spectrum for the as-prepared SnO_2 thin film deposited at -0.9 V for 10 min.

3.3.7 Optical transmission analysis and PEC measurement

Figure 3.6 shows the optical transmission spectra of the as-deposited samples with respect to the ITO substrate as reference. It is found that the estimated transmission averages in the visible region are 70.8% and 70.4% for the sample deposited for (a) 10 and (b) 7.5 min, respectively. No significant difference on the transmission values and this confirms the surface morphology result shown in Fig. 3.2. However, the results still indicate that the as-deposited films are transparent under visible light. However, no clear absorption edge for both samples is observed. Thus, the band gap of the as-deposited SnO_2 films could not estimated. Apparently, the band gap of the films seems larger than the reported value in the literature (~ 3.6-3.8 eV). The presence of the aggregated particles may affect the transmission result.

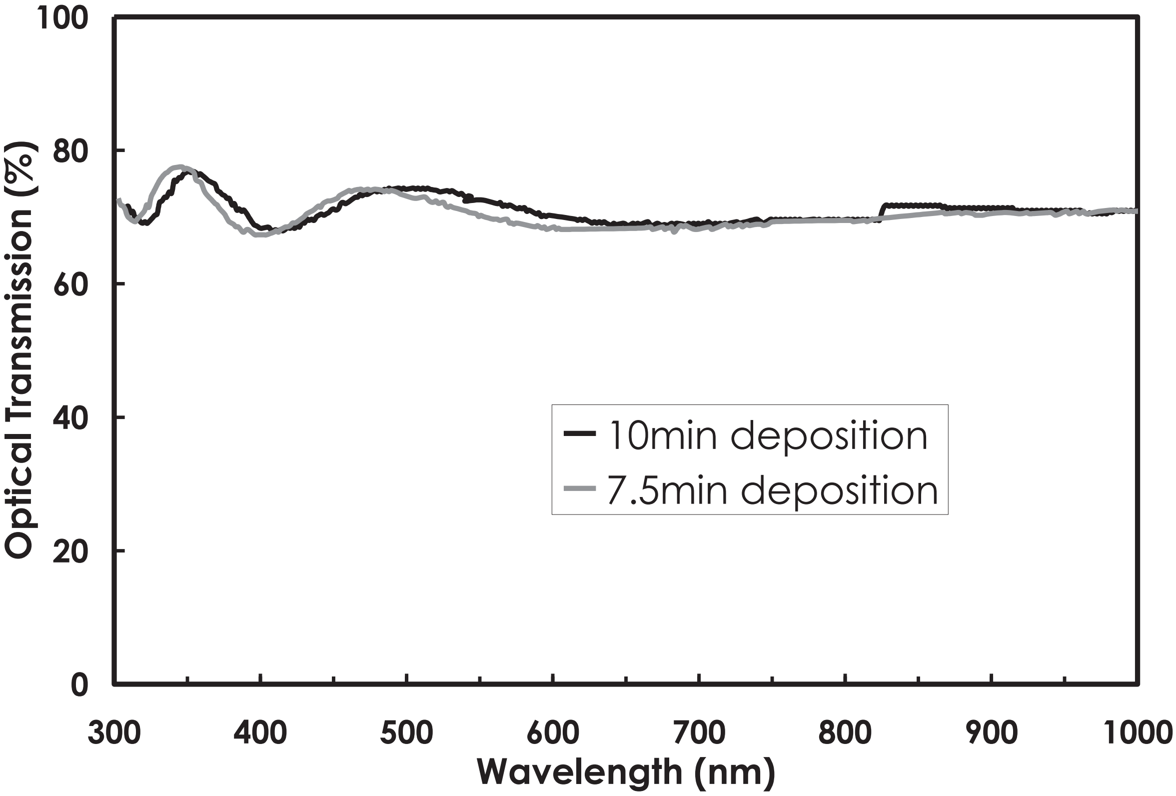

Fig. 3.6 Optical transmission curves for the as-deposited SnO_2 films.

The conductivity type and photosensitivity estimation of the deposited films are confirmed and evaluated from PEC measurement. The schematic diagram of this characterization is exhibited in Fig. 3.7. As shown in the figure, the components of the three-electrode electrochemical cell are similar in ED. The working solution used in the measurement contains 100 mM Na_2SO_4 as an electrolyte. Though various aqueous electrolytes can also be used as working solution; however, the dissolution of SnO_2 can be expected especially in strongly acidic aqueous solution. But it is already known that SnO_2 is stable in Na_2SO_4 solution. Light from the source is chopped by blocking the source (a Xe lamp with radiation power of about 100 mW/cm^2) using the shutter in the figure in an alternating manner ("on" and "off" states can be achieved). When the light is in the "on" state, it is directed through the solution and illuminated the portion of the sample from the transparent (glass) side of the substrate/film for 5 s. In the "off" state, light is blocked for 5 s. The process is repeated until the potential scan stops.

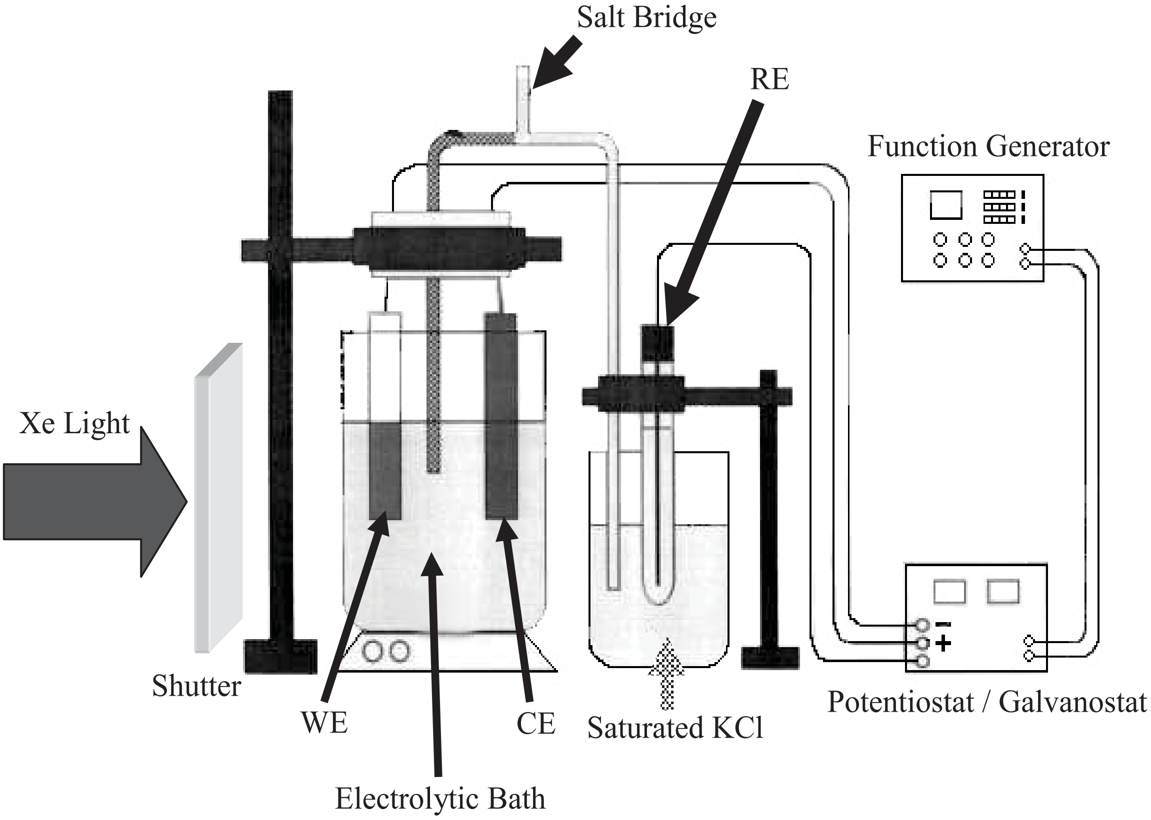

Fig. 3.7 Schematic diagram of the three-electrode system utilized for photoelectrochemical (PEC) measurement of the thin film.

The observed photocurrent responses under linearly increasing bias from -0.5 to +0.5 V for the samples and bare ITO are shown in Fig. 3.8. Under illumination, an essential increase in current response for the samples deposited for 7.5 and 10 min is attained compared to that observed in ITO only. This suggests that the deposited SnO_2 films have significant photosensitivity. Under both cathodic (from 0 to -0.5 V) and anodic bias (0 to +0.5 V), the photocurrent is positive, that is, the positive current density increased or negative current density decreased when light illumination is turned on. This behavior can be explained in terms of the excitation of carriers in the thin film upon light illumination. The photogenerated minority carriers flow and participate in the electrochemical reaction at the film-electrolyte interface. Since the observed photocurrent is positive, the photogenerated minority carriers are holes. Thus, the results confirm that SnO_2 thin film exhibits n-type conductivity with significant photosensitive behavior.

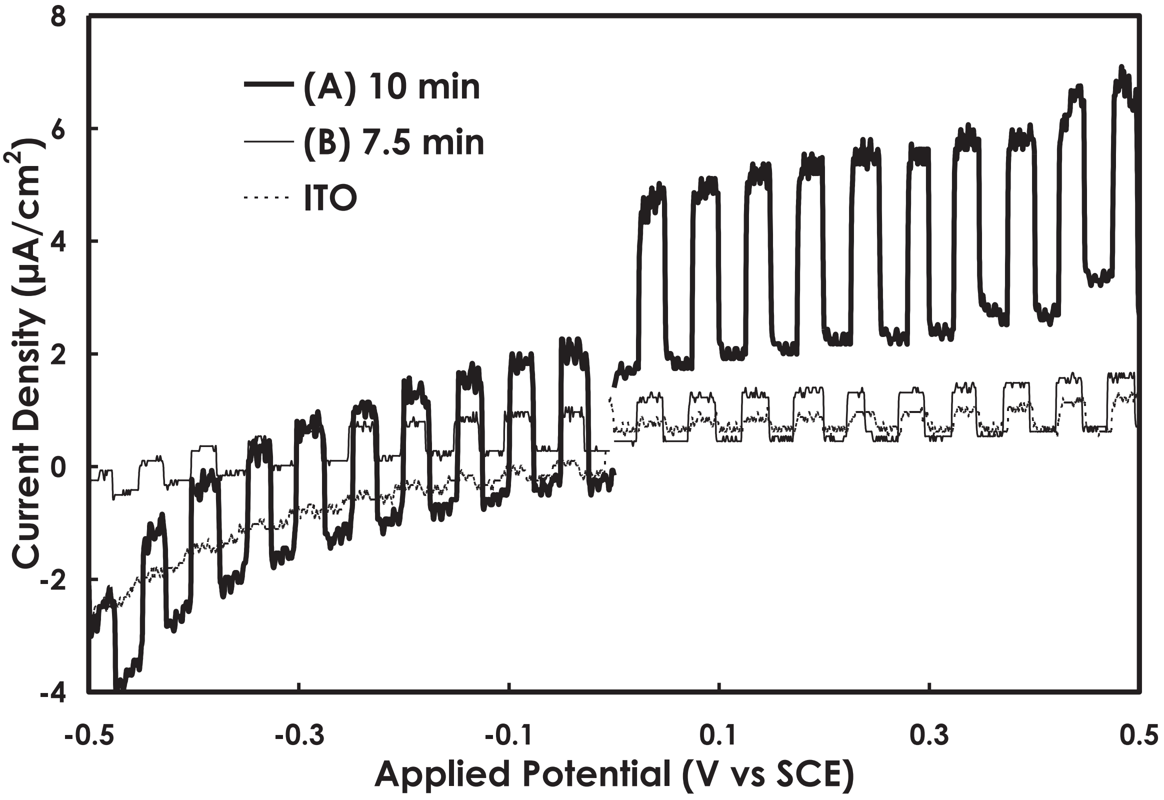

Fig. 3.8 Photosensitivity measurements under linearly increasing bias (from -0.5 to +0.5 V) for ITO and the SnO_2 samples deposited for (a) 10 and (b) 7.5 min.

3.3.8 Deposition mechanism

As noted in Sec. 3.2.2, the deposition reaction for SnO_2 formation is much enhanced by the oxygen bubbling. Therefore, dissolved oxygen from O_2 bubbling is the considered source of oxygen precursor. Under the constant negative voltage, the Sn^{2+} ions and the dissolved oxygen in the solution combine to deposit SnO_2 on the substrate following the reaction

$$Sn^{2+} + O_2 + 2e^- \rightarrow SnO_2. \tag{3.5}$$

In comparison to the cathodic electrodeposition of SnO_2 reported in Ref. 15, the following differences in the deposition process are regarded: (a) oxygen is blown through the solution, (b) the deposition is performed at room temperature, and (c) the solution pH is significantly lower than in the reported solution condition.

To verify if there is a change in pH during deposition, a pH meter is used to measure the pH change. It is found that the solution's pH has increased from the initial value (-0.03) to around 1.35 after 10 min deposition. This could signify that OH^- ions are generated in the solution during deposition. However, these OH^- ions may not contribute to the formation of SnO_2 according to reaction (3.2) since the solution is still strongly acidic. It is considered that the concentration of OH^- ions is relatively low because their presence will be neutralized by H^+ ions. Therefore, the source of oxygen in our work on SnO_2 deposition will be dissolved O_2 rather than OH^- ions.

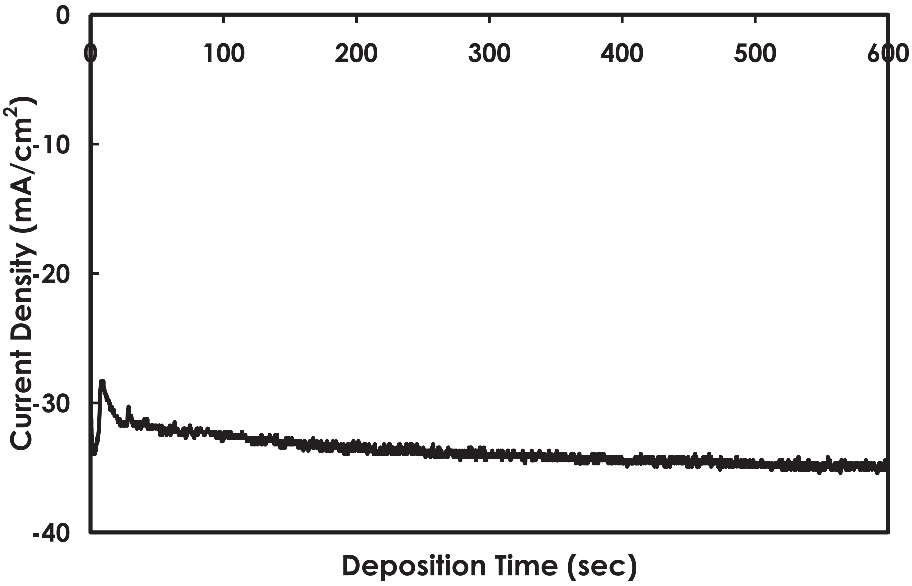

Fig. 3.9 Deposition current density plotted against time for the as-deposited SnO_2 film.

The current versus time profile of the sample deposited for 10 min is shown in Fig. 3.9. The deposition current first decreased within initial 10 s, and then increased gradually with deposition time. The initial decrease could be due to the change in the overpotential when coating of the electrode surface with SnO_2 progresses. As discussed in the CV results, the migration of Sn ions would be enhanced by the bubbling and thus the depletion of Sn ions near the cathode could not be the main reason for the current decrease. The reason of the gradual increase after the initial decrease is not clear. It may be related to the increase of the surface roughness, which means increase of nucleation sites can be expected. The change in the Sn ion concentration should have negligible influence on the current. To verify this, the amount of electrolyzed Sn ions during 10 min electrodeposition is estimated and it is approximately 1.0 x 10^{-4} mole. The value suggests that only a small amount of Sn ions is dissipated during deposition.

If all electrons of the deposition current are used in reaction (5), the thickness of the films can be calculated as follows based on Faraday's law

$$t = \frac{M_{film} J\, t'}{zF\rho_{film}}, \tag{3.6}$$

where M_{film} (*150.71 g/mol*) is the molecular weight, ρ_{film} (*6.95 g/cm^3*) is the density of deposited film, J is the current density, t' is deposition time, z is the number of transferred electrons according to the reaction given in eq. (3.5), and F (*9.65 x 10^4 C/mol*) is the Faraday's constant. Using the obtained absolute value (*~0.034 A/cm^2*) of current density (as shown in Fig. 3.8) for 10 min deposition, the thickness of the film according to Eq. (3.6) would be 22.7 μm. This value is much larger than the obtained thickness of the deposited film (0.1 μm). This indicates that only a small part of the current was utilized for the deposition of SnO_2 films on ITO. We found no gas generation in the vicinity of the substrate or formation of precipitates. Apparently, the SnO_2 film on the substrate is the only product of the electrochemical reactions. Hence, we may suppose that majority of the current charge is utilized for the generation of OH^- ions, which could be immediately neutralized by H^+ ions and contribute to the increase in pH during the deposition.

3.4 Conclusions

Transparent SnO_2 thin films were successfully electrodeposited onto ITO substrates from a very acidic tin sulfate solution at room temperature. Dissolved oxygen was considered as oxygen precursor. Sn-rich films were obtained as reflected in the AES analysis. The as-deposited films were considered either amorphous or nanocrystalline structure as revealed from diffractions peaks obtained in XRD. From PEC measurement results, the n-type conductivity and the good photosensitivity of the films were confirmed. Further studies are still needed to improve the uniformity and crystallinity of the film in order to have efficient window or buffer layer for heterojunction solar cell fabrication.

References

[1] C. Li, W. Wei, H. Wang, S. Wu, S. Fang, and R. Chen: J. Phys.: Conf. Ser. **152** (2009) 012035.

[2] I. Aruna, F. E. Kruis, S. Kundu, M. Muhler, R. Theissman, and M. Spasova: J. Appl. Phys. **105** (2009) 064312.

[3] H. Keskinen, A. Tricoli, M. Marjaki, J. M. Makela, and S. E. Pratsinis: J. Appl. Phys. **106** (2009) 084316.

[4] H. Ohgi, T. Maeda, E. Hosono, S. Fujihara, and H. Imai: Cryst. Growth Des. **5** (2005) 1079.

[5] D. Perednis and L. J. Gauckler: J. Electroceram. **14** (2005) 103.

[6] T. M. Racheva and G. W. Critchlow: Thin Solid Films **292** (1997) 299.

[7] T. Tsuchiya, K. Daoudi, A. Watanabe, T. Kumagai, and S. Mizuta: J. Phys.: Conf. Ser. **59** (2007) 224.

[8] S. Supothina, M. R. De Guire, and A. H. Heuer: J. Am. Ceram. Soc. **86** (2003) 2074.

[9] M. Izaki and T. Omi: J. Electrochem. Soc. **144** (1997) 1949.

[10] S. Peulon and D. Lincot: J. Electrochem. Soc. **145** (1998) 864.

[11] D. Ramirez, D. Silva, H. Gomez, G. Riveros, R. E. Marotti, and E. A. Dalchiele: Sol. Energy Mater. Sol. Cells **91** (2007) 1458.

[12] S. Otani, J. Katayama, H. Umemoto, and M. Matsuoka: J. Electrochem. Soc. **153** (2006) C551.

[13] S. Yamabi and H. Imai: J. Mater. Chem. **12** (2002) 3773.

[14] E. Hosono, S. Fujihara, H. Imai, I. Honma, and H. Zhou: Chem. Commun. (2005) 2609.

[15] S. T. Chang, I. C. Leu, and M. H. Hon: Electrochem. Solid-State Lett. **5** (2002) C71.

CHAPTER 4

Electrodeposition and Characterization of SnO_2 Thin Films from Aqueous Tin Sulfate Solutions

(II. Oxygen Bubbling Employed Before Deposition)

4.1 Introduction

It has been reported that agitation incurred by either gas bubbling or stirring (mechanical agitation) during deposition could enhance the removal of hydrogen bubbles discharged at the cathode and provide sufficient mixing of the chemical precursors in the electrolyte [1]. However, the physical appearance of the SnO_2 thin films electrodeposited in aqueous solution with oxygen bubbling during deposition (as discussed and presented in **Chapter 3**) contains white residual aggregate particles. Preliminary results on the electrodeposition of SnS on as-deposited SnO_2 revealed that the presence of these aggregates hinder the deposition of quality SnS layer (as *p-type* absorber layer) to fabricate SnS/SnO_2 superstrate heterostructure. The apparent effects of these aggregate could be the intensified surface roughness that limits the electrodeposition of the absorber layer. Due to this encountered problem, the deposition condition for *n-type* SnO_2 layer needs to be modified before the fabrication of the desired superstrate structure (combination of *p-type* material and SnO_2). The SnO_2 window layer should have at least minimal roughness to have smooth or flat surface and highly transparent to be an effective layer for photon transmission. The following modifications in the deposition process have been made and presented in this chapter: (a) the working solution or electrolyte is bubbled with oxygen through the solution only before deposition. This is done to ensure a quiescent solution during deposition. This bubbling process has been reported to be successful in the electrodeposition of ZnO from quiescent aqueous solution [2-3]. As a result, the solution is not affected by the stirring effects incurred by gas bubbling; and (b) after bubbling through the solution, oxygen purging continues but it is now carried out above the surface of the electrolyte to minimize, if not completely removed, other gas impurities from the surrounding that may participate in the deposition process. The schematic diagram of the closed electrochemical cell with oxygen bubbling employed prior to deposition is illustrated in Figure 4.1. The prepared electrolytes with different pH values: (a) pH = -0.03 (similar to the pH condition described in the **Chapter 3**) and (b) pH = 0.4 are performed in this study to determine the suitable deposition condition for heterojunction fabrication. Cyclic voltammetry and pre-test deposition experiments are carried out initially to determine the appropriate potential to deposit better SnO_2 thin film.

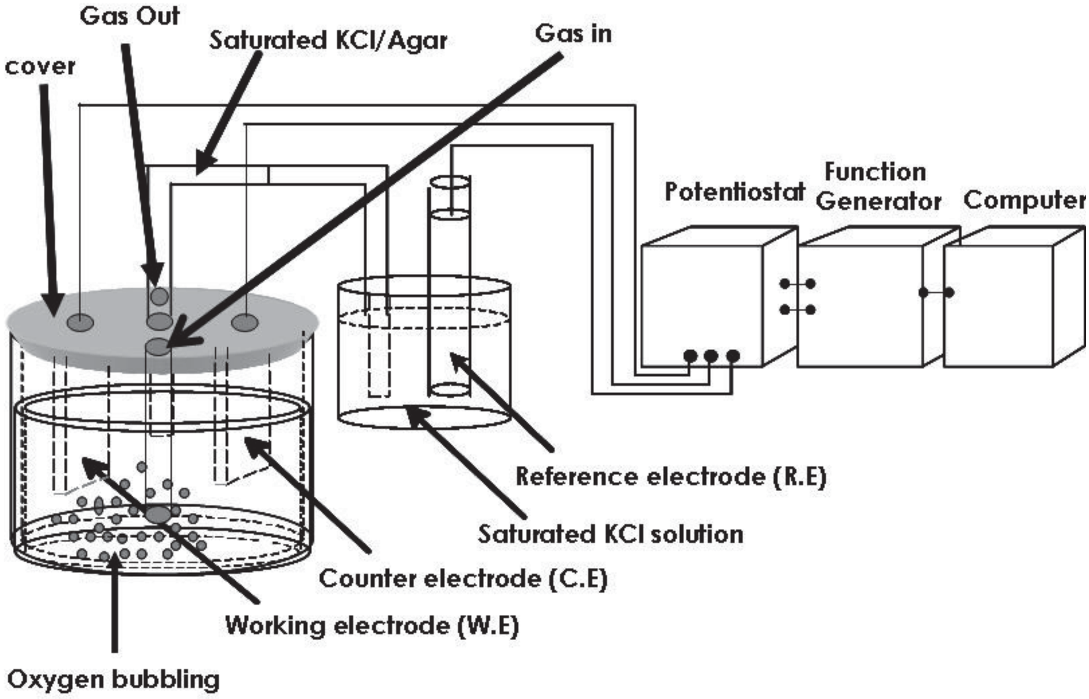

Fig. 4.1 Schematic diagram of the three-electrode electrochemical cell with oxygen bubbling employed prior to electrodeposition.

4.2 Cyclic voltammetry study

Figure 4.2 shows the cyclic voltammetry (CV) curves of (*a*) no oxygen bubbling and (*b*) 10 min oxygen bubbling before deposition for electrolytes with pH = -0.03. As depicted in this figure, the electrochemical reactions revealed from CV results for the two electrolytes start at relatively the same potential (~ -0.5 V). When this potential is attained, the current density started to increase until the reduction peak is reached and it is discernable near -0.95 V for un-bubbled (curve *a*) and pre-bubbled solution (curve *b*). This signifies that the deposition potential window to obtain SnO_2 thin films occurs at similar potential range and the presence of oxygen in the solution did not change the overpotential to activate the electrochemical reaction. It should be noted that extending the bubbling time did not change the CV curve, that is, very similar CV as depicted in curve (*b)*. Comparing the CV curves obtained in oxygen-bubbled solution shown in Fig. 3.1 (**in Chapter 3**) and Fig. 4.2; the observed reduction peak in the pre-oxygen-bubbled solution is the remarkable results attained from a quiescent solution during deposition. This result also verifies the disappearance of the peak due to the stirring effects incurred by bubbling if stirring is employed during deposition.

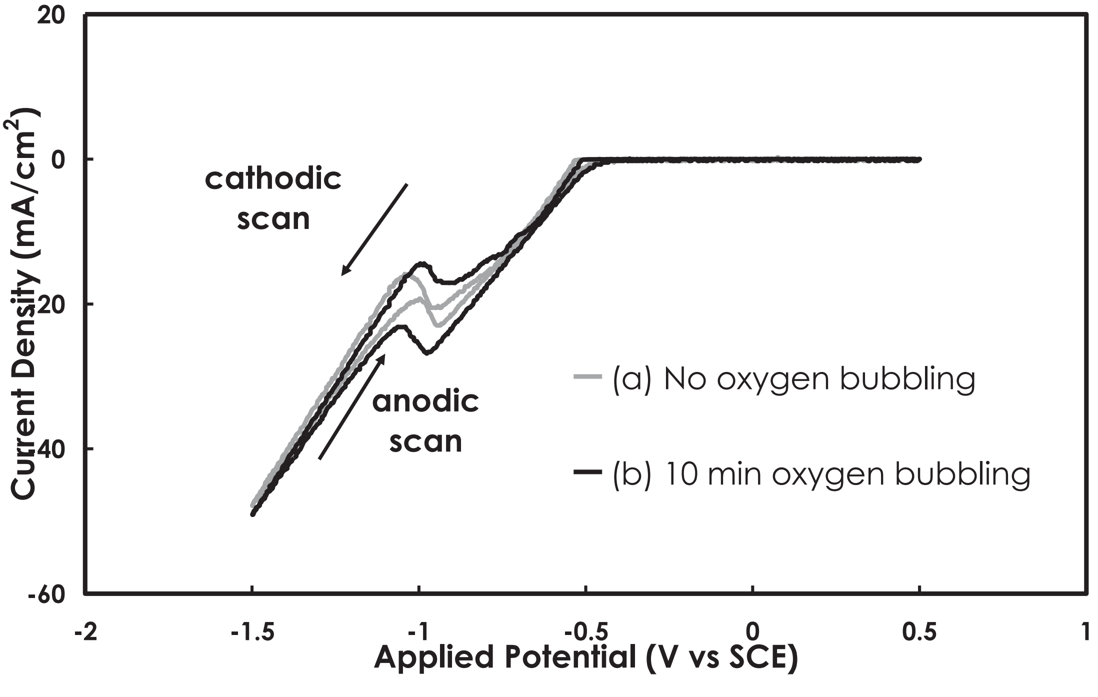

Fig. 4.2 Cyclic voltammetry curves for solutions with (a) no O_2 and (b) 10 min O_2 bubbling recorded at a constant scan rate of 20 mV s^{-1} and at pH = -0.003 (Similar to the pH condition employed in Chap. 3).

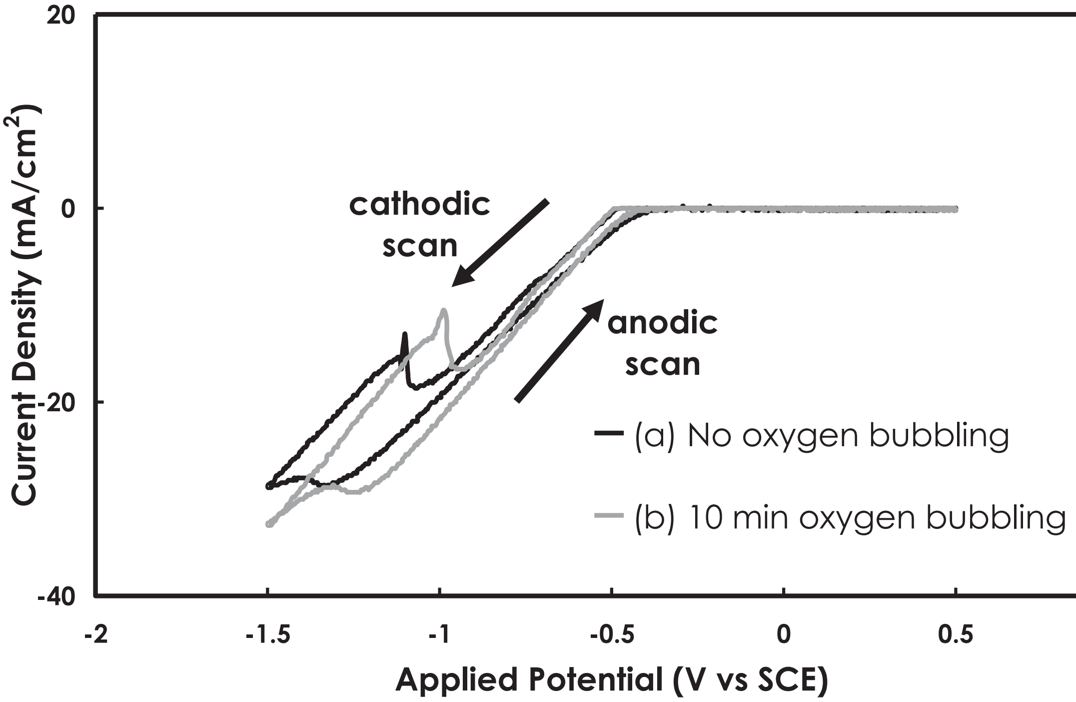

Fig. 4.3 Cyclic voltammetry curves for solutions with (a) no oxygen and (b) 10 min O_2 bubbling recorded at a fixed scan rate of 20 mV s^{-1} and at pH = 0.4.

Fig. 4.3 shows the CV curves of (*a*) no oxygen bubbling and (*b*) 10 min oxygen bubbling before deposition for electrolytes with pH = 0.4. As revealed in this figure, discernable reduction peaks near -1.08 and -0.95 V for un-bubbled and pre-oxygen-bubbled solution are attained, respectively. Comparing Figs. 4.2 *(b)* and 4.3 *(b)*, the observed reduction peak is located at almost the same potential. However, a shift of the reduction peak is evident for un-bubbled and bubbled solutions, as seen in curves 4.3 *(a)* and 4.3 *(b)*. The shift is directed towards less negative potential. It could mean that the overpotential is also shifted in the same direction and this may imply that the potential needed to activate the electrochemical reaction at the substrate/electrolyte interface is reduced with the presence of oxygen bubbling. Hence, an enhanced deposition reaction of SnO_2 thin films on the substrate can be expected.

4.3 Deposition potential, pH and deposition time optimization

In the preliminary stage of electrodeposition, try-test deposition is usually carried out to optimize electrochemical parameters such as deposition potential, deposition time, and to determine the quality of the deposits with respect to these parameters. The potential values (-0.92, -0.90, and -0.88 V) are decided from the CV results shown in Figs. 4.2 and 4.3. However, very thin films are obtained from the solution with pH = -0.03. Similarly, in the absence of oxygen and at pH = 0.4, very weak adhesion between the film and substrate is observed even after 10 min deposition. However, at the same deposition time and pH = 0.4, transparent thin films are attained from oxygen-bubbled solution. Hence, all the succeeding depositions are focused at this pH condition. From visual observation during deposition, it seems that white and thick films could be achieved; but when deposition ended after 10 min, some weakly-adhered white aggregates were removed by careful washing of the freshly deposited film, leaving a thinner and smoother film appearance. It should be noted that at more negative potential (e.g. -0.95 and -1.05 V), aggregation of white particles (powder-like) is more intensified and highly favored; thus, some of these aggregates could not be removed by washing in deionized water. Therefore, the considered potential values are between -0.88 to -0.92 V. All the films deposited at -0.92, -0.90, and -0.88 V, have similar physical appearance and the thickness is approximately 0.07 - 0.1 μm, which can be considered thickness of strongly-adhered film on the substrate.

When the duration of oxygen bubbling and deposition time are extended, the obtained films are translucent in appearance and strongly-adhered white particulates are highly favorable. This leads to a less transparent films and significant increase in the roughness of the films can be attained. Hence, 10 min oxygen bubbling prior to deposition (considered as electrolyte preparation or pre-deposition preparation) and another 10 min for deposition are already appropriate to produce SnO_2 thin films at room temperature under quiescent solutions with suitable thickness and relatively reduced roughness, which is necessary for heterostructure fabrication.

4.4 Morphological, compositional, and optical transmission studies: as-prepared and annealed SnO_2 thin films

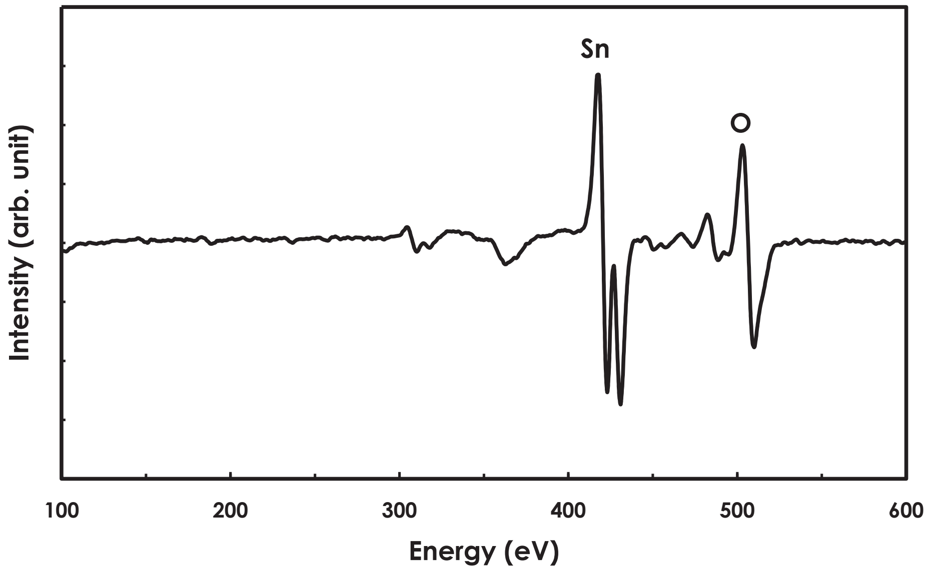

Fig. 4.4 Differential AES spectrum of as-deposited SnO_2 film deposited at -0.90 V.

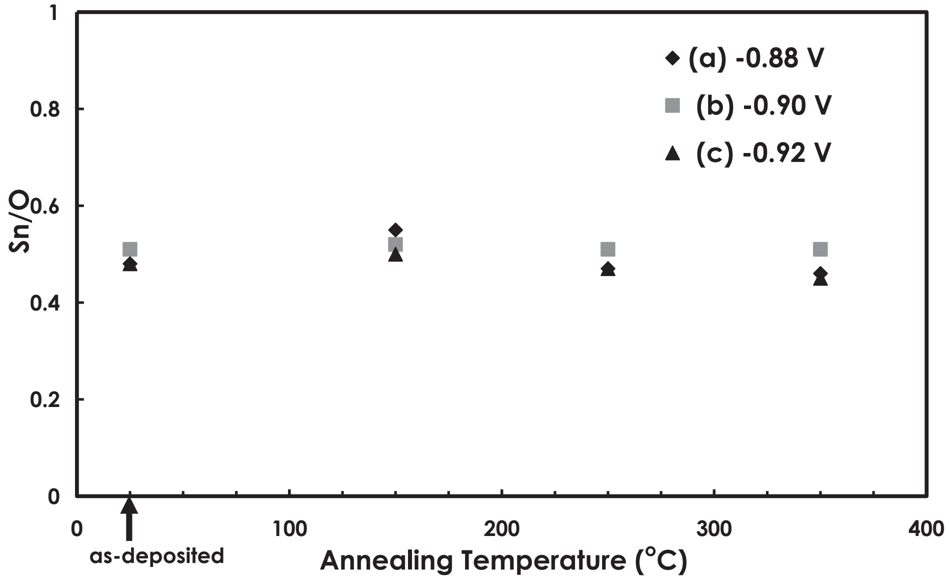

Fig. 4.5 Relationship of Sn/O ratio with annealing temperature for SnO_2 thin films at different potentials: (a) -0.92, (b) -0.90 and (c) -0.88 V.

The Auger differential spectrum of the as-prepared sample deposited at -0.9 V after 10 s Argon-ion sputtering is shown in Figure 4.4. Impurities due to carbon and sulfur contaminations are removed after sputtering. As depicted in this figure, only Sn and O peaks are clearly observed in the spectrum. The calculated Sn/O ratio for the as-deposited sample is about 0.51, which is near the stoichiometric ratio of SnO_2 (Sn/O = 0.5). This signifies that SnO_2 film is formed on the substrate.

Thermal annealing is also performed to study its effect on the composition. The annealing process is carried out in a tube furnace under air ambient with heating rate of ~10°C/min and the considered temperatures are 150, 250, and 350°C. For 250°C-annealed sample deposited at -0.9 V, the calculated Sn/O ratio is 0.51, which is similar to the Sn/O ratio for the as-deposited sample. The relationship of the composition ratio against annealing temperature is plotted and summarized in Figure 4.5. As seen in this figure, the Sn/O values are all closer to 0.5 with variation of about ± 0.05. These results imply that no big difference is obtained in the Sn to O ratios (still close to stoichiometric ratio). Thus, it is difficult to decide the optimum annealing temperature based on AES results only.

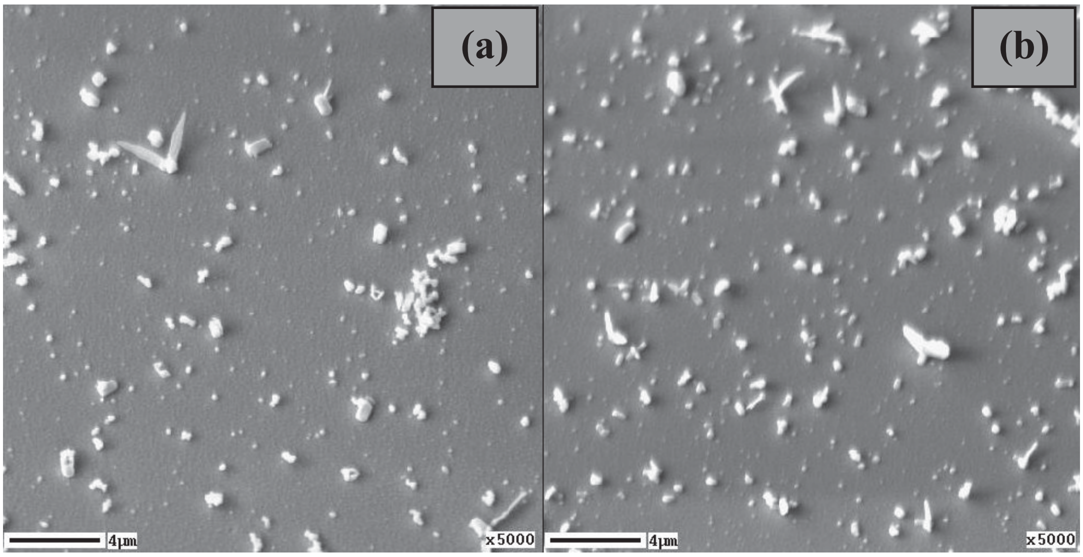

Fig. 4.6 Surface morphologies of (a) as-deposited and (b) 250°C-annealed samples deposited for 10 min at reduction potential of -0.90 V.

Figure 4.6 shows the morphologies of the as-prepared and 250^{o}C-annealed SnO$_2$ thin films deposited at -0.9 V for 10 min. As can be seen, both surfaces are similar and contain a flat background with some aggregates. No big difference can be observed in the morphologies of as-deposited and annealed SnO$_2$. Also, similar morphologies as depicted in this figure are attained for as-prepared and annealed samples deposited at -0.88 and -0.92 V at the same deposition time.

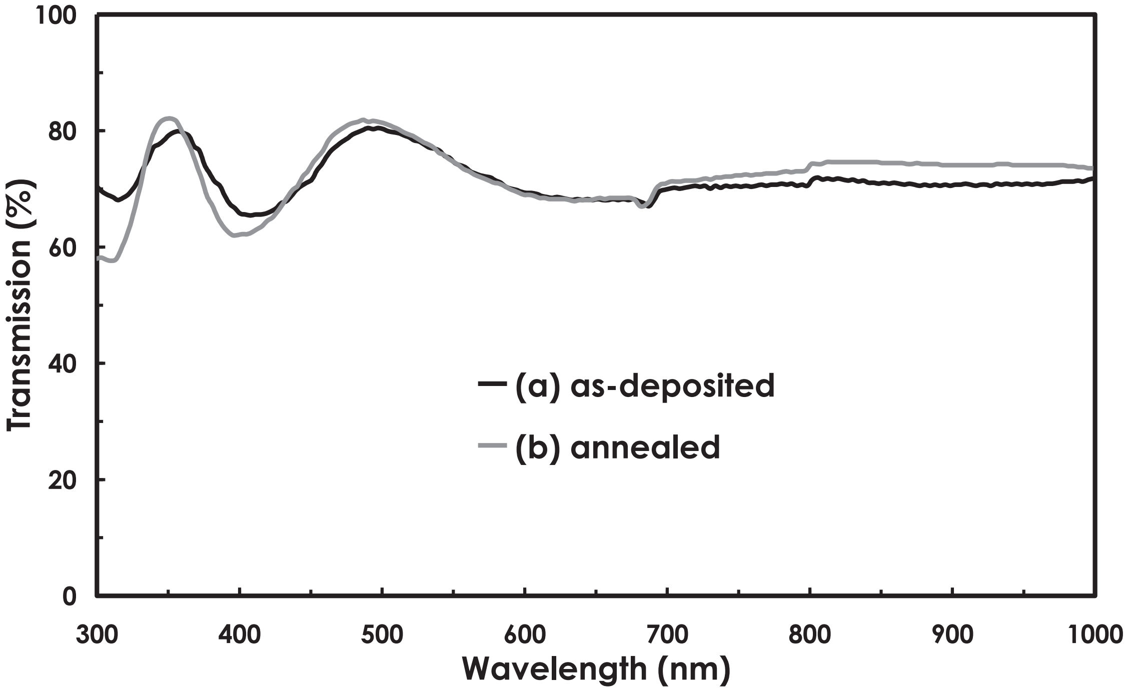

Fig. 4.7 Optical transmission of (a) as-deposited and (b) 250^{o}C-annealed SnO$_2$ thin films deposited for 10 min at deposition potential of -0.90 V.

Figure 4.7 shows the transmission curves of as-prepared and annealed SnO$_2$ films deposited at -0.90 V for 10 min. Both films exhibit ~ 71-73 % average optical transmission from 400 – 1000 nm wavelength range. Slight variation in the transmission is observed at 300 – 400 nm wavelengths. For instance, 12 % and 24 % decrease in transmission is attained for as-deposited and annealed films from 350 – 300 nm, respectively. It seems that the absorption edge for both samples is located in this wavelength range. However, the band gap could not be estimated precisely. Moreover, similar transmission curves as depicted in Fig. 4.7 are also attained for as-prepared and annealed SnO_2 films deposited at -0.88 and -0.92 V at the same deposition time.

Meanwhile, comparing the transmission results obtained for SnO_2 films deposited from pre-oxygen-bubbled solution with the transmission data presented in Fig. 3.6 (in **Chapter 3**), it appears that almost similar optical transmission properties are obtained. In fact, no significant change in the transmission averages are observed for films produced from different oxygen bubbling condition. The possible effect of deposition from quiescent solution is the improvement in the smoothness of the as-deposited and annealed samples.

4.5 XPS study of annealed SnO_2 thin film

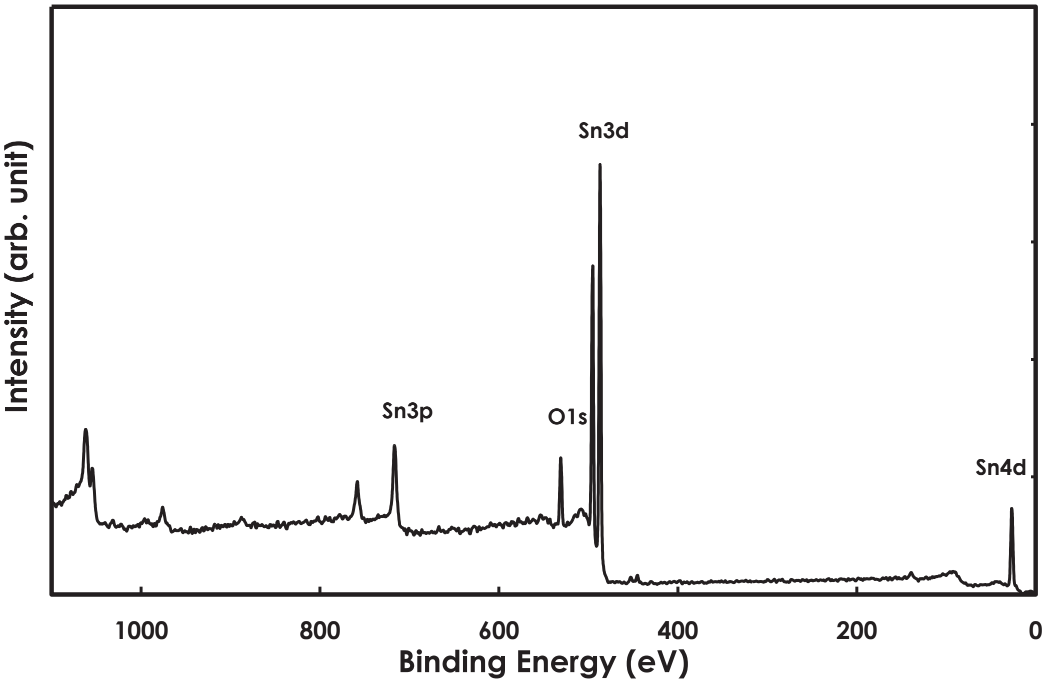

Fig. 4.8 Wide scan XPS spectrum obtained after 30s sputtering for 250°C-annealed SnO_2 thin film.

X-ray photoelectron spectroscopy (XPS) is carried out to further study the chemical state at the surface and the inner part (bulk) of the 250°C-annealed SnO_2 thin film. Figure 4.8 shows the wide scan XPS spectrum after 30 s of sputtering for the annealed film at the bulk. Similar pattern is attained after 120 s sputtering. The Auger peaks of the constituents of the film are evident in the higher binding energies. It should be noted that the surface of the annealed sample contains some ubiquitous carbon impurities as reflected by the C 1s peak located at a binding energy (E_B) of 285 eV. After sputtering, the peak due to carbon contamination is not detected in the spectrum as shown in Fig. 4.8.

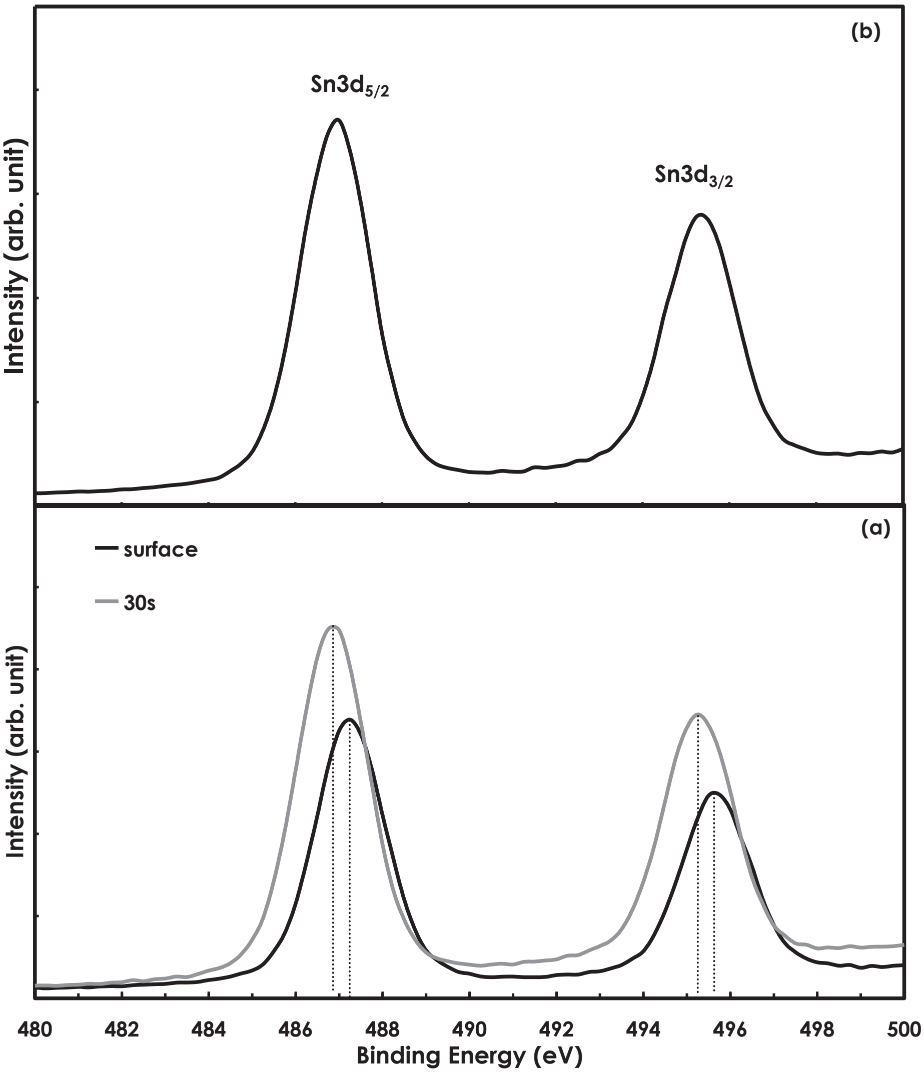

Fig. 4.9 Sn3d spectra for 250°C-annealed SnO_2 film (a) at the surface, after 30 s, and (b) after 120 s of sputtering.

The Sn 3d levels of the annealed film are also obtained at the surface and after 30 and 120 s of sputtering as depicted in Figure 4.9 (a) and (b). It is clear that the spectra taken at the surface and bulk of the film exhibit two peaks associated to Sn $3d_{5/2}$ and Sn $3d_{3/2}$ levels: one is at 486.75 (487.25) eV and the other is located at 495.25 (495.75) eV at the bulk (surface), respectively. The simple shape of the Sn 3d peaks suggests that only one chemical state of Sn atoms [4]. The binding energy of Sn $3d_{5/2}$ peak at 486.75 eV may indicate the presence of SnO or SnO_2 since their binding energies are almost similar [5-8]. In the literature, the reported binding energies of 486.5 and 486.25 eV are assigned to Sn^{4+} (for SnO_2) and Sn^{2+} (for SnO) peaks, respectively [5]. No evidence is observed from the contribution of elemental Sn^0 atoms at E_B of ~ 485 eV. However, a slight shift (about 0.5 eV) observed for Sn 3d levels towards lower binding energy is attained at the bulk (after sputtering) relative to that obtained at the surface. In addition to that, the Sn 3d peaks at the bulk are slightly broaden, which may imply a little increase in the FWHM of the peaks. This effect is likely to happen due to the partial reduction of Sn^{4+} since oxygen may be removed during Argon ion sputtering [6].

Figure 4.10 (a) and (b) represent the XPS spectra of O 1s core level of the annealed film at the surface and bulk (after 30 and 120 s sputtering). Different types of oxygen can demonstrate various binding energies such as 530.70 eV for O^-, 530.15 eV for O^{2-}, 530.6 eV and 532.8 eV for O_2^- [9]. The XPS spectrum shows that at the surface shows a main peak at 531.25 eV with a very slight shoulder located near 532 eV. The main peak at 531.25 eV can be assigned to O^-, O^{2-}, O_2^- that can either form O-Sn^{4+} or O-Sn^{2+} bonds and the slight shoulder may be attributed to oxygen impurities or oxygen in the adsorbed hydroxyl groups [10]. The presence of these oxygen impurities can contribute to the O/Sn composition ratio of the film attained in the AES analysis. After 30 s of sputtering, the O 1s main peak is located at 530.75 eV, which is much closer to the literature binding energy assignment for O^{2-} in SnO_2 material. Similar binding energy for O 1s peak is obtained after 120 s of sputtering as shown in Fig. 4.10 (b). This could imply that at the bulk it is more likely that the bond form is for SnO_2. In a similar manner, the main O 1s peak at the bulk is also shifted towards lower E_B by 0.5 eV with respect to that obtained at the surface.

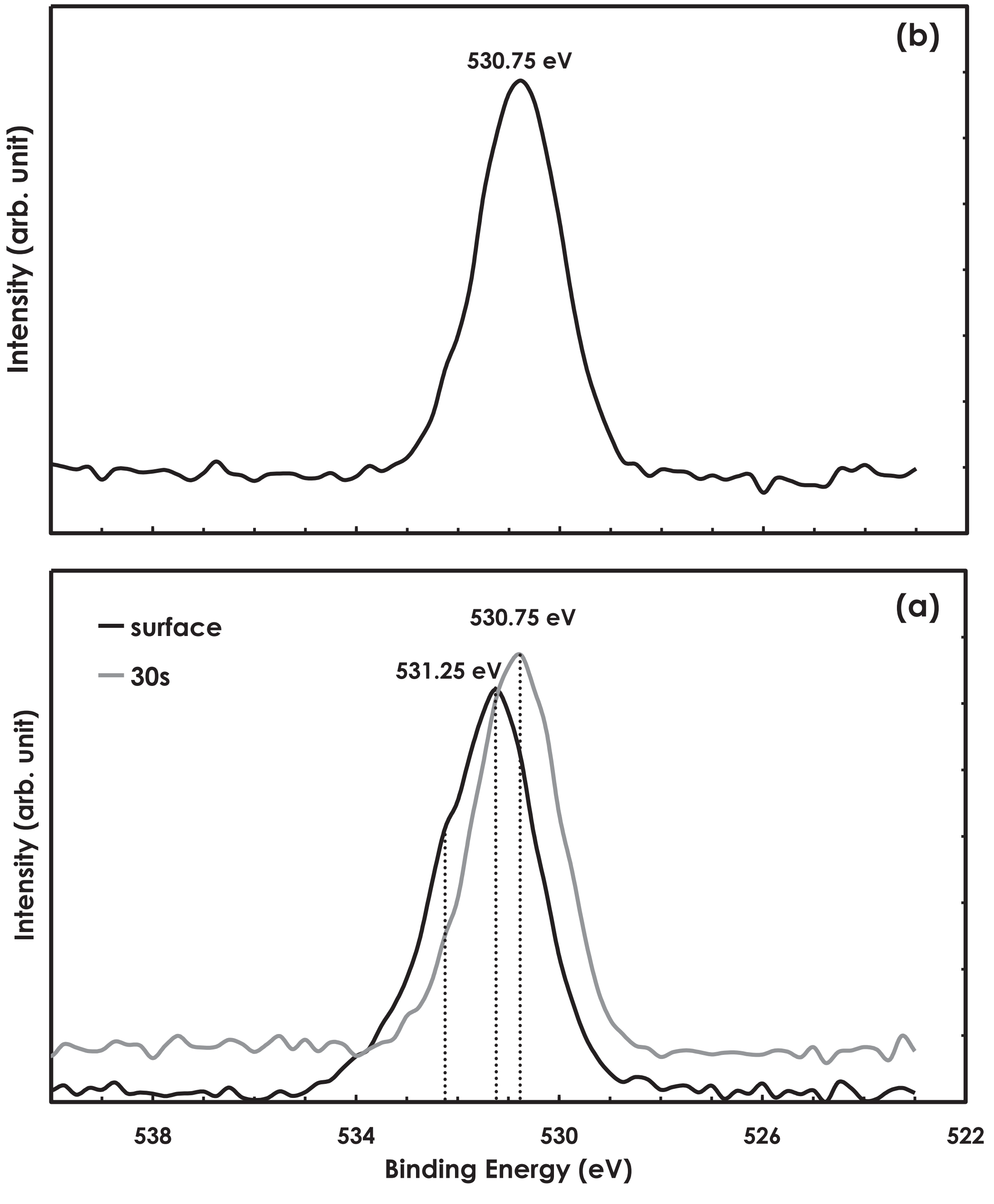

Fig. 4.10 O1s XPS spectra (a) at the surface and after 30 s sputtering and (b) after 120 s sputtering for the 250°C-annealed SnO_2 film.

In order to separate the chemical shift of binding energy corresponding to a change of the sample stoichiometry from the shift of interface Fermi level position $\Delta E_F = E_F - E_v$ in the band gap, several researchers proposed new procedure for the deconvolution of Sn $3d_{5/2}$ and O1s peaks core levels. Based on this proposed procedure, two additional assumptions can be considered: [11-14]

- The Sn $3d_{5/2}$ peak in SnO_x is built-up of the following three components: Sn^{4+}, Sn^{2+} and Sn^0 components; Sn^{2+} and Sn^0 components shifted towards the lower binding energy (E_B) by 0.7 and 2.2 eV with respect to Sn^{4+} component, respectively.
- The O 1s peak in SnO_x is built-up of the following two components: O-Sn^{4+} and O-Sn^{2+} components; O-Sn^{2+} component shifted towards lower binding energy (E_B) by 0.6 eV with respect to the O-Sn^{4+} component.

Based on the above assumptions and the observed shift in the Sn $3d_{5/2}$ and O 1s peaks at the bulk relative to that at the surface, it seems that this shift in Sn $3d_{5/2}$ as well as the O 1s are still not clear whether these are due to the chemical shifting of Sn^{2+} and O-Sn^{2+} components with respect to Sn^{4+} and O-Sn^{4+} components, respectively. Additional information is needed to explain the reasons behind this shift.

It has been reported that thermal treatment on SnO_2 surfaces can activate surface reduction and consequently a transformation of Sn surface from Sn^{4+} to Sn^{2+} could be achieved. This can result to the occupation of mainly empty Sn 5s states in Sn^{4+}. These 5s electrons form lone pair electrons and can be associated with band gap surface states at the reduced surface. As a result, a higher concentration of oxygen vacancies in SnO_2 would be expected, that is, O/Sn composition ratio is reduced. Moreover, the occupation of Sn 5s states can be explained from the apparent change in the valence band maximum (VBM) spectrum. The VBM spectra at the surface and after sputtering for the annealed SnO_2 are shown in Figure 4.11. As depicted in this figure, an additional broad peak near 2.6 eV referenced to the Fermi level is observed at the bulk compared to that at the surface of the sample. This observed peak represents the reduction of Sn surface from Sn^{4+} to Sn^{2+} that happens upon annealing at high temperature or under oxygen atmosphere condition. The transformation can be regarded as Sn 5s derived surface states [15-17].

Additionally, as a consequence of the higher concentration of oxygen vacancies, the VBM is also shifted by approximately 0.8 eV towards lower E_B at the bulk (from VBM ~ 3.8 eV at the surface to 3.0 eV after sputtering). These observations could be the reasons why Sn $3d_{5/2}$ and O 1s are shifted by 0.5 eV towards lower binding energy.

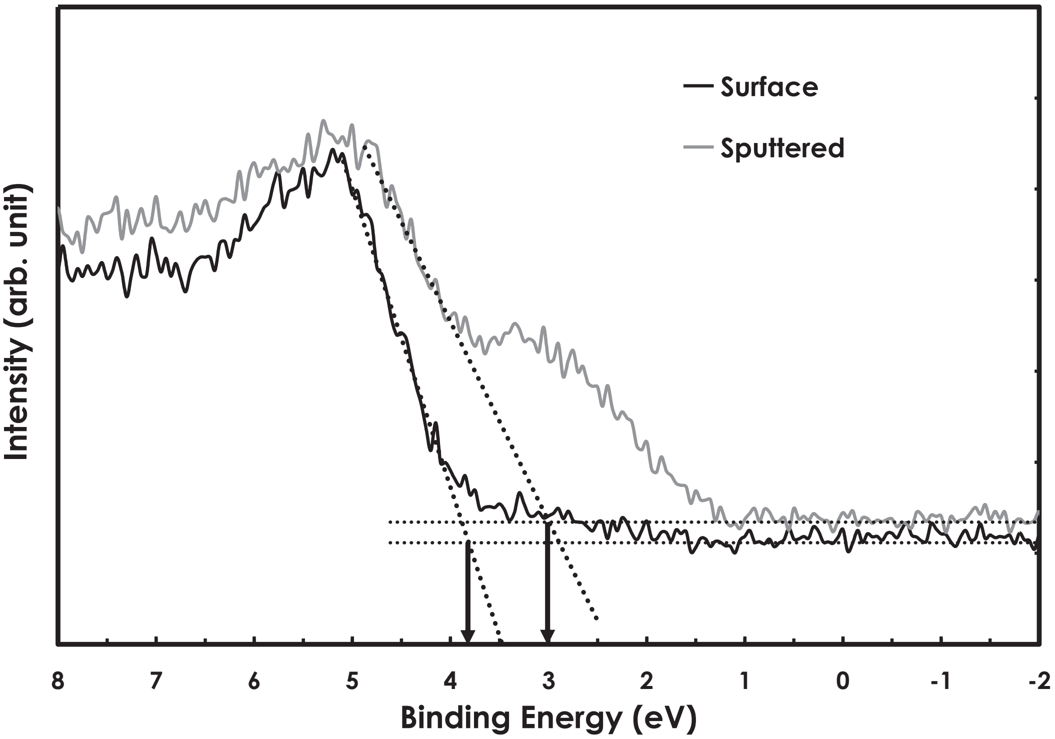

Fig. 4.11 Valence band maximum (VBM) spectrum at the surface and bulk of the 250°C-annealed SnO_2 film. Extrapolation of the linear region is shown to determine VBM.

4.6 Conclusion

SnO_2 thin films were successfully electrodeposited from pre-bubbled oxygen aqueous solution on ITO-glass coated substrate. From CV results, the suitable deposition potential is close to -0.90 V. SnO_2 thin films electrodeposited at -0.88, -0.90 and -0.92 V exhibited very similar appearance and morphologies. Thermal annealing of the films at temperatures of 150, 250 and

350°C did not change the Sn/O ratio significantly. As-prepared and annealed films exhibited nearly stoichiometric ratio of SnO_2 and no significant difference was obtained in their respective optical transmittance in the visible wavelength region. From XPS study carried out for annealed SnO_2 film, the binding energies obtained for Sn $3d_{5/2}$ and O 1s levels revealed the characteristics of O-Sn chemical state. A shift of about 0.5 eV towards lower E_B is attained for both Sn $3d_{5/2}$ and O 1s peaks evaluated at the bulk with respect to that of the film surface. Furthermore, the VBM spectrum at the bulk showed additional broad peak near 2.6 eV, which can be attributed to the Sn 5s-derived surface states due to the transformation of Sn surface from Sn^{4+} to Sn^{2+}. In addition to that, a shift of about 0.8 eV in the VBM at the bulk compared to that attained at the surface. The considered possible effect of the deposition from quiescent solution is the improvement in the roughness of the as-deposited and annealed films, in which, the deposition of SnS as *p-type* layer could be successfully electrodeposited at room temperature.

References

[1] A. V. Espelt: *Multifunctional Electrodeposited Nanocrystalline Cu-Ni Films*: **Ph.D. Thesis** (2012).

[2] A. I. Inamdar, S. H. Mujawar, S. B. Sadale, A. C. Sonavane, M. B. Shelar, P. S. Shinde, and P. S. Patil: Sol. Energy Mater. Sol. Cells **91** (2007) 864.

[3] A. I. Inamdar, S. H. Mujawar, V. Ganesan, and P. S. Patil: Nanotech. **19** (2008) 1.

[4] I. D. Shcherba, K. Zakrzewska, J. Szuber, G. Czempic, A. I. Senkevich, and I. I. Kravchenko: Phys. Stat. Solidi. (B) 238 (2003) 7.

[5] J. F. Moulder: *Handbook of X-ray Photoelectron Spectroscopy* (Perkin-Elmer Corp., Eden, Prairie, 1992).

[6] P. Stefanov, G. Atanasova, E. Manolov, Z. Raicheva, and V. Lazarova: J. Phys.: Conf. Ser. 100 (2008) 082046.

[7] D. Barreca, S. Garon, E. Tondello and P. Zanella: Surf. Sci. Spectra **7** (2000) 81.

[8] P.A Grutsch, M.V Zeller, and T.P. Fehlner: *Inorg. Chem.* **12** (1973) 1432.

[9] W.-S. Choi: Trans. Elect. Electron. Mater. **10** (6) (2009) 200.

[10] A. M. Abdel Haleem Hassan: *Electrochemical Deposition of InS-based Thin Films for Photovoltaic Applications*, **Ph.D. Thesis (**2010) & references therein.

[11] J. M. Themlin, M. Chtaib, L. Henrard, P. Lambin, J. Darville, and J. M. Gilles: Phys. Rev. B **46** (1992) 2460.

[12] B. Yea, H. Sasaki, T. Osaki, K. Sughara, and R. Konishi: Jpn. J. Appl. Phys. **38** (1999) 2103.

[13] R. Larciprete, E. Borsella, P. De Padova, P. Perfetti, G. Faglia, and G. Sberveglieri : Thin Solid Films **323** (1998) 291.

[14] J. Szuber, G. Czempik, R. Larciprete, and D. Koziej, and B. Adamowicz: Thin Solid Films **391** (2001) 198.

[15] M. Batzill: Sensors **6** (2006) 1345.

[16] M. Batzill and U. Diebold: Prog. Surf. Sci. **79** (2005) 47.

[17] M. Batzill, et al.: Phys. Rev. B **72 (**2005) 165414-1.

CHAPTER 5

Fabrication of Electrodeposited SnS/SnO$_2$ Heterojunction Solar Cells

5.1 Introduction

Fabrication of cost-effective and environmentally benign semiconductor materials such as tin oxide (SnO_2) and tin sulfide (SnS) for solar cell applications is certainly possible by employing facile electrodeposition (ECD) methods. SnO_2 has been considered as one of the popular transparent conducting oxides and a promising window or buffer layer material in heterojunction solar cells because of its wide band gap (3.6 - 3.8 eV) characteristics and high transparency in the visible region. SnS has a direct energy band gap of 1.3 eV and is regarded as a good candidate for absorption layer because of its high absorption coefficient. Moreover, the advantage of utilizing SnO_2 and SnS for solar cell devices is that the constituent elements are relatively economical, abundant, and non-toxic. So far, SnS has been partnered with ZnS [1], $ZnS_{1-x}O_x$ [2], ZnO [3], F:SnO_2 [4], TiO_2 [5], InS_xO_y [6], CdS [6-11], $Cd_{1-x}Zn_xS$ [12], SnS_2 [13], and a-Si [14] to fabricate heterojunction solar cells. All of these fabricated SnS-based heterostructures share common problem: low conversion efficiency. To date, the reported highest solar conversion efficiency of 1.3% in SnS-related heterojunction devices was obtained from CdS/SnS heterostructure [7].

One of the possible reasons for the poor performance of the SnS-based solar cell is the band alignment at the heterointerface. The band offset has been experimentally evaluated for SnS-based heterojunctions [6, 15]. Sugiyama *et al.* have reported and fabricated the SnS/SnO_2 heterojunction by sulfurization growth of SnS on SnO_2-coated glass substrate and reported the band offsets at the interface by X-ray photoelectron spectroscopy (XPS). The estimated valence band offset (ΔE_V) is 3.5 eV, which indicates that the valence band maximum (VBM) of SnS is located very near to the conduction band minimum (CBM) of SnO_2. Hence, degenerate SnO_2 tends to inject electrons into the SnS, and the junction is expected to be ohmic [15].

To avoid the toxicity of CdS layer, in this work, SnO_2 is utilized as the SnS heterojunction partner. It should be noted that the SnS/F:SnO_2 heterostructure in Ref. 3 was fabricated by a combination of chemical bath deposition (CBD) and spray pyrolysis techniques. To our knowledge, no studies on the fabrication of SnS/SnO_2 heterojunction via electrochemical route have been reported. The photovoltaic characteristics of electrodeposited SnS/SnO_2 superstrate heterostructure are evaluated and reported in this chapter. Moreover, the band alignment between SnS and SnO_2 materials is also presented based on the XPS core level spectroscopy and the relation between the photovoltaic characteristics and the band alignment is discussed.

5.2 Experimental Methods

5.2.1 SnO_2-SnS heterostructure fabrication

ECD has been successfully applied for SnO_2 [16-17] and SnS [2, 11, 18-24]. It should be noted that the method of preparation of SnO_2 is adopted from our previous work on electrodeposition of SnO_2 from aqueous solution [16] with modifications on the bubbling process and pH (as discussed in the previous chapter). Prior to the electrodeposition process, the indium-tin-oxide (ITO) coated glass substrate is ultrasonically degreased in alkyl benzene and deionized water. SnO_2 thin films are then electrodeposited on the pre-cleaned ITO substrate from an aqueous solution containing 30 mM $SnSO_4$ at room temperature. The pH is adjusted to 0.4 by adding adequate amount of HNO_3. The solution is pre-bubbled with oxygen at a constant rate of 0.5 L/min before deposition. Various deposition potentials between -0.88 and -0.92 (V versus SCE) are employed to deposit SnO_2 thin films onto the ITO substrate. These potential values are considered from the cyclic voltammetry (CV) results presented in **Chapter 4**. All samples are electrodeposited for 10 min. After the deposition, all the films are naturally dried in ambient air. Prior to SnS deposition, the as-deposited SnO_2 thin films are annealed in air using a tube furnace at temperatures between 150 and 350 ^oC for 1 h. SnS thin films were then electrodeposited on the annealed SnO_2 films using an aqueous solution containing $SnSO_4$-$Na_2S_2O_3$ salts with corresponding concentrations of 30 mM and 100 mM, respectively. A three-step pulsed voltage

(V_1 = -1.0, V_2 = -0.6, and V_3 = 0 V versus SCE) with equal pulse time ($t_1 = t_2 = t_3$ = 10 s) is employed for 20 min to deposit SnS at room temperature [23]. All depositions (for SnO$_2$ and SnS) are performed in a quiescent solution.

5.2.2 SnS-SnO$_2$ heterostructure characterizations

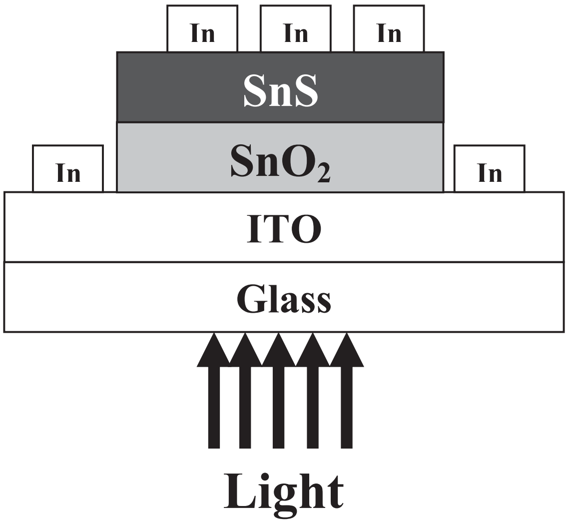

Fig. 5.1 Schematic representation of the fabricated SnS/SnO$_2$ heterojunction solar cells with indium metal as electrical contacts.

The thickness of the SnO$_2$ sample was measured by a profilometer. Indium electrodes with 1 mm^2 area each were evaporated on top of the fabricated SnS/SnO$_2$ heterojunction to provide electrical contacts during current-voltage (J-V) measurement. The schematic representation of the fabricated SnS/SnO$_2$ heterostructure is shown in Figure 5.1. The fabrication was performed layer by layer via electrodeposition method. The surface morphology and chemical composition of the individual layers were analyzed by scanning electron microscopy (SEM) and Auger electron spectroscopy (AES) using JEOL JAMP-9500F, respectively. Argon ion sputtering (with an etching rate of 10 nm/min) was performed for 10 s to remove carbon impurities in the surface of SnO$_2$ layer. Current-voltage (J-V) measurement was done using 100-mW/cm^2-solar simulated light to confirm rectification property and evaluate the solar cell performance of the fabricated

SnS/SnO$_2$ heterostructures. XPS measurement was carried out using XPS PHI-5000 (ULVAC-PHI) with the Al Kα used as an X-ray source to study the interface between SnS and SnO$_2$ layers.

5.3 Results and Discussion

5.3.1 SnO$_2$-SnS deposition and solar cell fabrication

SnO$_2$ thin films adhered well on the ITO substrate. The thickness of the films as measured by a profilometer was approximately 70-100 nm. Figures 5.2 (a) and (b) showed the surface morphology of the as-deposited and 250^{o}C-annealed SnO$_2$ films deposited at -0.92 V. As seen in these figures, small and aggregated grains were present on the surface. No significant difference was observed on the morphologies of as-deposited and 250^{o}C-annealed films. Similar effects on the morphology were observed at annealing temperature of 150 and 350^{o}C.

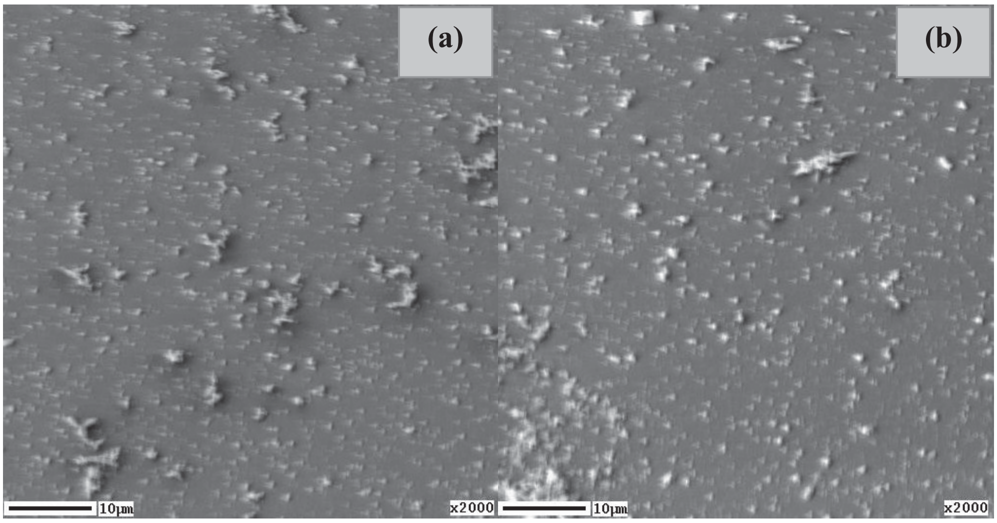

Fig. 5.2 Surface morphologies for (a) as-deposited and (b) 250^{o}C-annealed SnO$_2$ thin films deposited at -0.92 V for 10 min.

The Auger spectra of as-deposited and 250^{o}C-annealed samples deposited at -0.92 V after 10 s Ar ion sputtering are shown in Figure 5.3. As depicted in Fig. 5.3(a) for as-deposited film, only Sn and O peaks were observed with Sn:O ratio of 1:1.96, which signifies that nearly stoichiometric film is obtained. Similar Auger spectrum, shown in Fig. 5.3(b), was observed for 250°C-annealed sample with Sn to O ratio close to 1:2. Moreover, for samples annealed at 150 and 350°C, the composition ratios (Sn/O) are still near the stoichiometric ratio (refer to Fig. 4.5 in

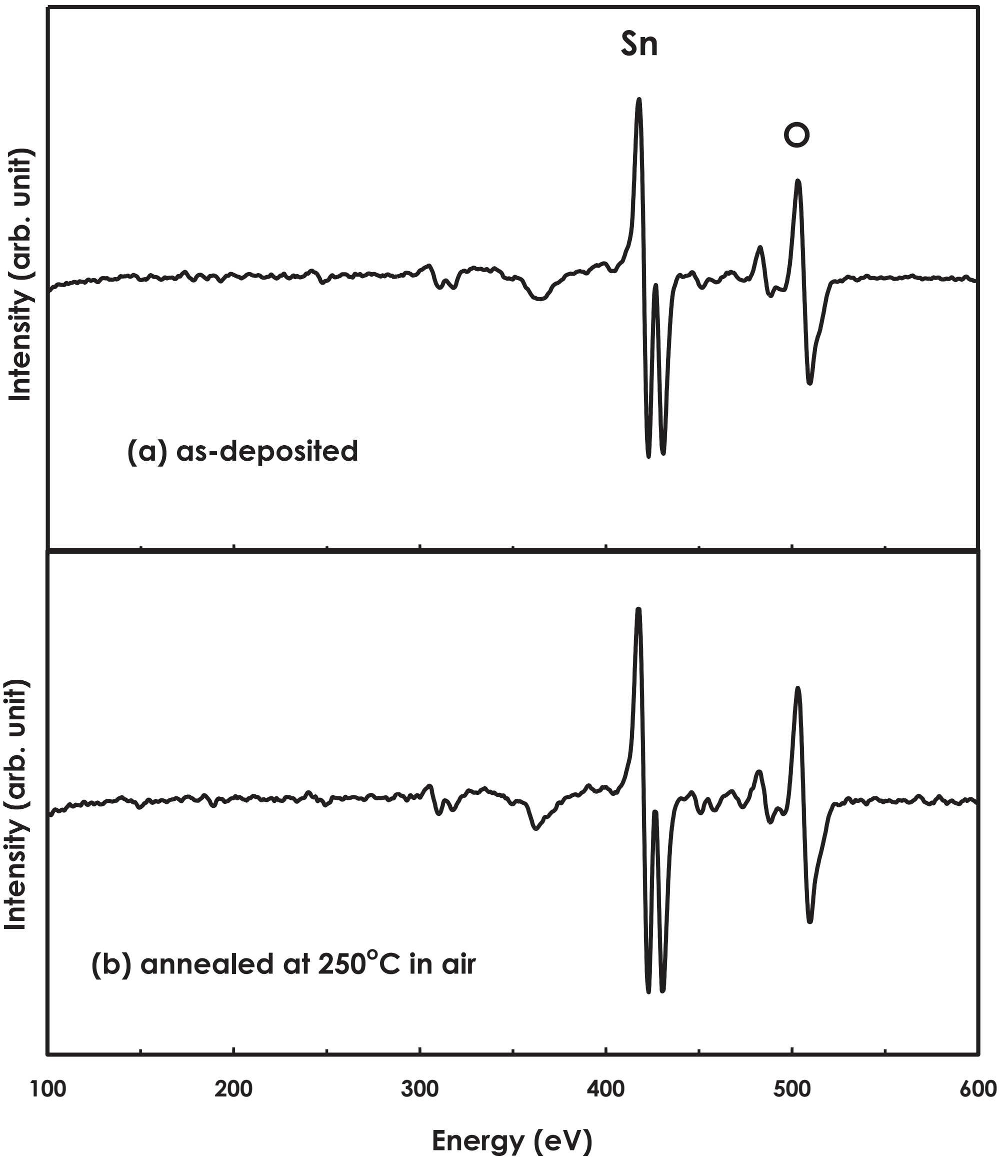

Fig. 5.3 Differential Auger spectrum of (a) as-deposited and (b) annealed SnO$_2$ thin films deposited at -0.92 V.

Chapter 4). Hence, annealing in air did not significantly affect the composition of the SnO$_2$ films.

Preliminary fabrications were conducted on both as-deposited and annealed SnO$_2$ thin films to fabricate SnS/SnO$_2$ heterostructures. However, relatively good adherence of SnS on annealed SnO$_2$ was obtained compared to SnS on as-deposited SnO$_2$. Possibly, some modification of the surface of SnO$_2$ layer after annealing is obtained. Thus, all the heterostructures presented in the succeeding discussion were fabricated using the annealed SnO$_2$ thin films as window layers.

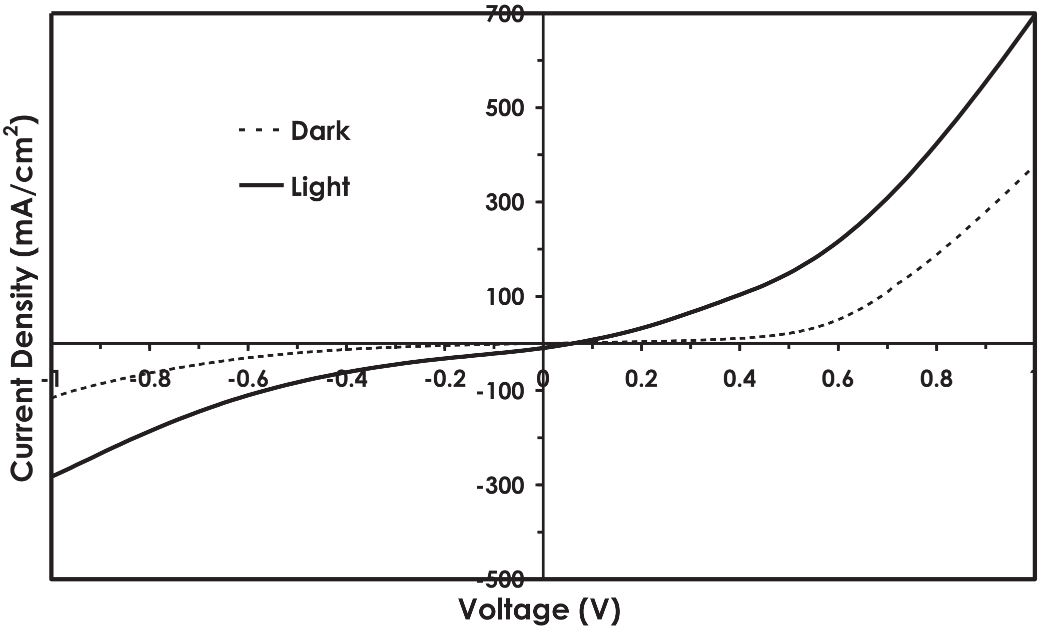

Fig. 5.4 Current-voltage (J-V) characteristics of electrodeposited SnS/SnO$_2$ heterojunction with 250^{o}C-annealed SnO$_2$ layer under dark and light conditions.

The characteristics of SnS/SnO$_2$ superstrate heterostructure under dark and light conditions with SnO$_2$ layer deposited at -0.90 V and subsequently annealed in air at 250^{o}C prior to SnS deposition are shown in Figure 5.4. The SnS/SnO$_2$ heterostructure is further analyzed by considering the current-voltage (I-V) curve under dark condition as shown in Figure 5.5. Several features can be deduced from this I-V curve. First, in the forward bias, three possible regions are attainable. Namely, region I ($0 \text{ V} < V_{forward} \leq 0.3 \text{ V}$) displays linear relation of current with respect to voltage. Region II ($0.3 \text{ V} \leq V_{forward} \leq 0.72 \text{ V}$) shows exponential behavior of current with $\beta \sim 7.5\ V^{-1}$. Region III ($0.72\ V < V_{forward} \leq 1.0\ V$) demonstrates linearity of the current-voltage relationship at high forward bias. It should be noted that the steepness of this linear region would correspond to high or low series resistance of the device that has significant effect on the solar cell characteristics. The series resistance R_s can be estimated from the slope of the I-V curve in this region (the diode R_s is equal to the inverse of the slope when linearity is obtained in high forward bias region). The calculated R_s is ~ 108.6 Ω. This value is much larger than the expected values for efficient solar cells (R_s << 1 Ω). Second, it seems that the current starts to increase between 0.3 – 0.4 V. This means that the cut-in voltage is located in this voltage range (cut-in or threshold potential corresponds to the potential barrier that the carriers needed to overcome in order to contribute to the forward current). Fourth, it is apparent that the heterojunction exhibits some rectifying behavior (exponential I-V characteristics were observed). Fifth, in the reverse scan, it appears that the leakage current started to be visible between -0.3 to -0.4 V and exponentially increases after that. These observed features in some ways contribute to the photovoltaic performance of the solar cell device.

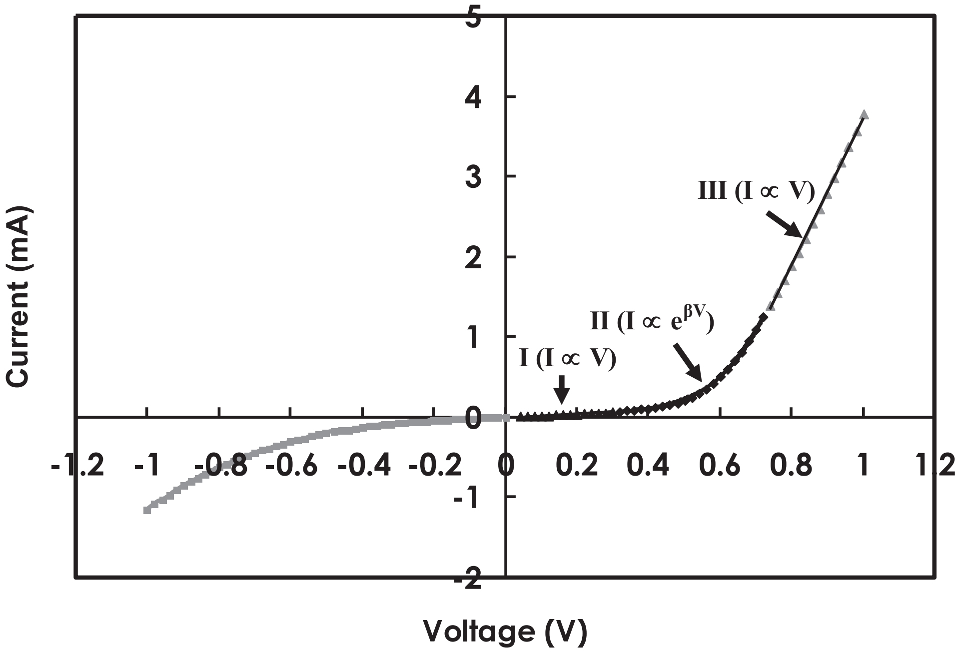

Fig. 5.5 Current-voltage (I-V) curve of SnS/SnO$_2$ heterojunction under dark condition.

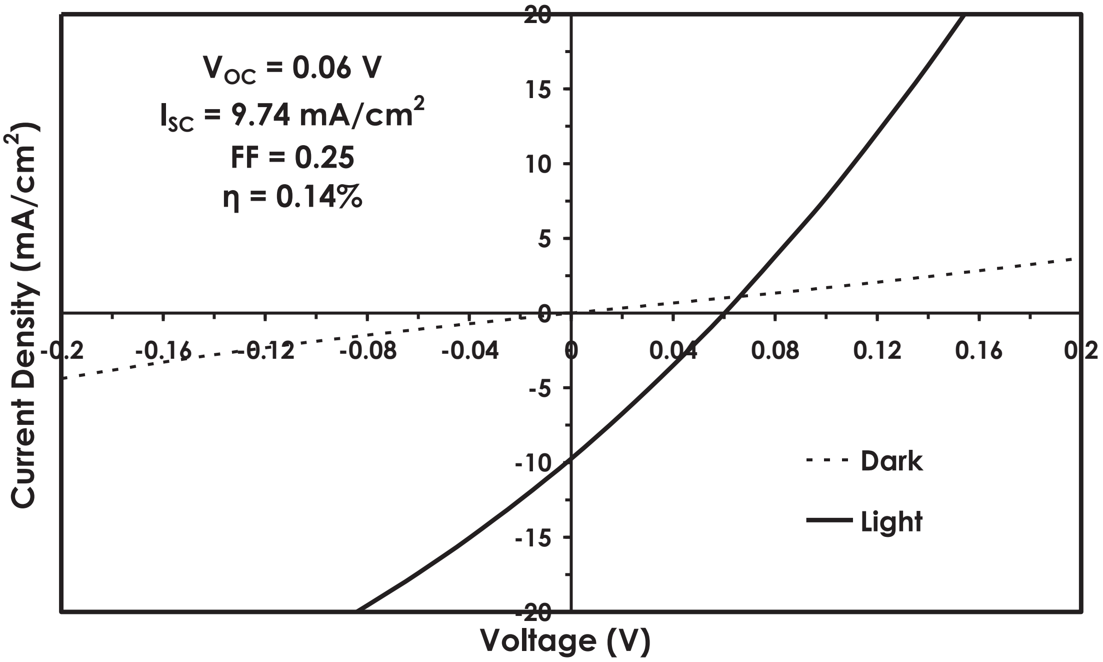

Fig. 5.6 The J-V curve shown in Fig. 5.4 is expanded near 0 V to estimate the photovoltaic parameters such as V_{OC} and J_{SC} under illumination.

The open circuit voltage (V_{OC}) and short circuit current density (J_{SC}) are determined by expanding the region near 0 V of the J-V curve, as depicted in Figure 5.6. The estimated V_{OC} and J_{SC} were found to be 60 mV and 9.74 mA/cm^2, respectively. The solar cell conversion efficiency is approximately 0.14%. The same cell showed variation of the values of the solar cell parameters: for instance, V_{OC} (40 - 60 mV) and J_{SC} (6.32 – 9.74 mA/cm^2) were attained from one electrode point to another. This may indicate that the fabricated layers of the SnS/SnO_2 heterostructure have significant non-uniformity. Similar behavior of J-V curves were observed for heterostructures with 250^{o}C-annealed SnO_2 layer deposited at -0.88 and -0.92 V with variations of the estimated solar cell parameters as illustrated in Figure 5.7. The best values of (V_{OC}, J_{SC}) for SnS/SnO_2 heterostructures with annealed SnO_2 layer were approximated to be (90 mV, 1.54 mA/cm^2) and (70 mV, 3.94 mA/cm^2) for the -0.88 and -0.92 V deposition potentials, respectively. The solar conversion efficiency is approximately in the order of 10^{-2} - 10^{-1} %. These results suggest that the fabricated SnS/SnO_2 heterojunctions exhibit rectifying and photovoltaic characteristics. However, the output voltages for all cells are small (less than 0.1 V) and the reproducibility is very poor: sometimes the cell showed poor rectification properties and negligible photocurrent. For SnS/SnO$_2$ heterostructures with 150- and 350°C-annealed SnO$_2$ layers, the J-V characteristics showed very poor rectification (nearly ohmic type behavior) and insignificant photovoltaic effect was attained.

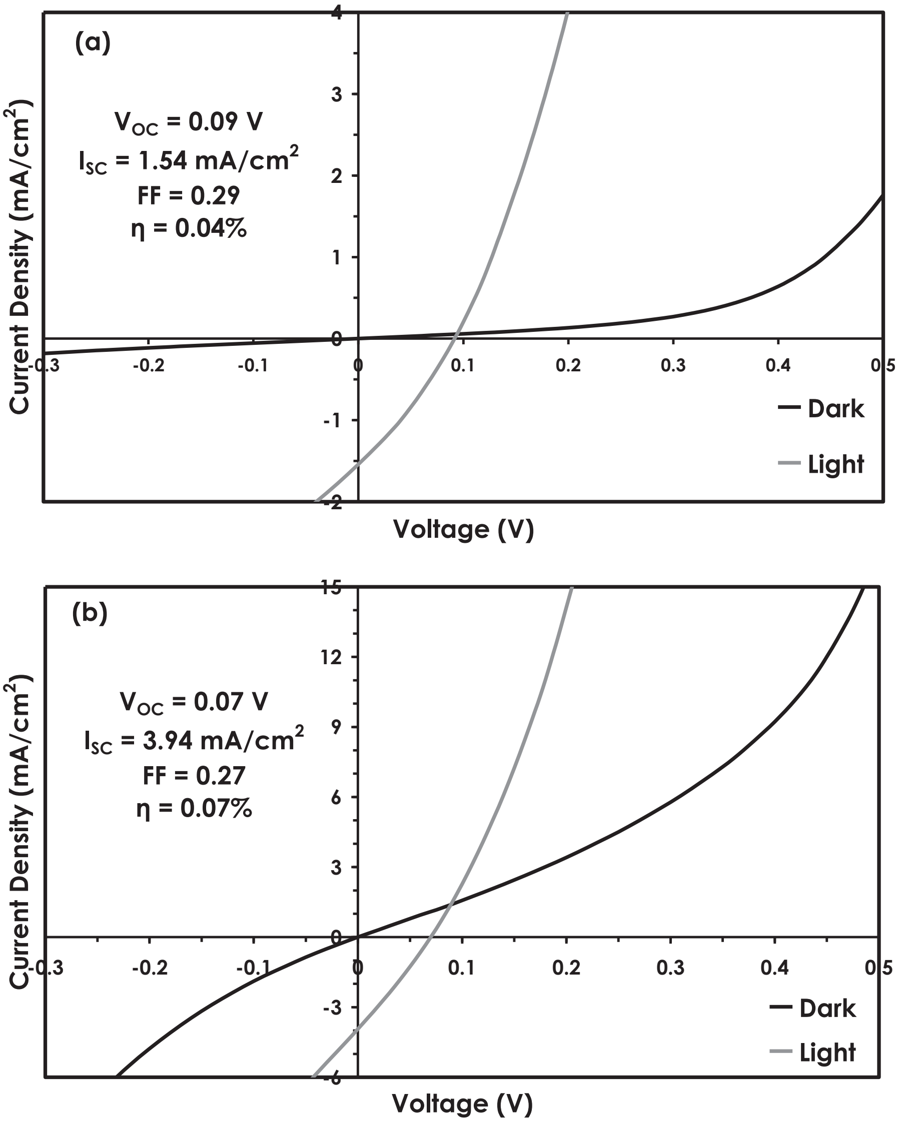

Fig. 5.7 Current-voltage curves for SnS/SnO$_2$ heterojunctions with SnO$_2$ annealed at 250°C and deposited at (a) -0.88 and (b) -0.92 V for 10 min.

5.3.2 XPS measurement

The band alignment between SnS and SnO$_2$ is developed based on core-level spectroscopy [25-26]. The valence and conduction band offsets of SnS/SnO$_2$ heterostructure can be determined by using the following relations:

$$\Delta E_V = \left(E_{Sn4d}^{SnS} - E_V^{SnS}\right) - \left(E_{Sn4d}^{SnO_2} - E_V^{SnO_2}\right) - \Delta E_{CL} \tag{5.1}$$

$$\Delta E_C = \Delta E_g - \Delta E_V \tag{5.2}$$

The expressions inside the parentheses in Eq. (5.1) represent the difference of the energy position of Sn 4d levels in SnS-SnO$_2$ individual layers and the corresponding VBM in each layer. ΔE_{CL} is the difference in the Sn 4d level between SnS and SnO$_2$ and determined at the interface of SnS/SnO$_2$ bilayer. ΔE_g corresponds to the band gap difference of the two materials.

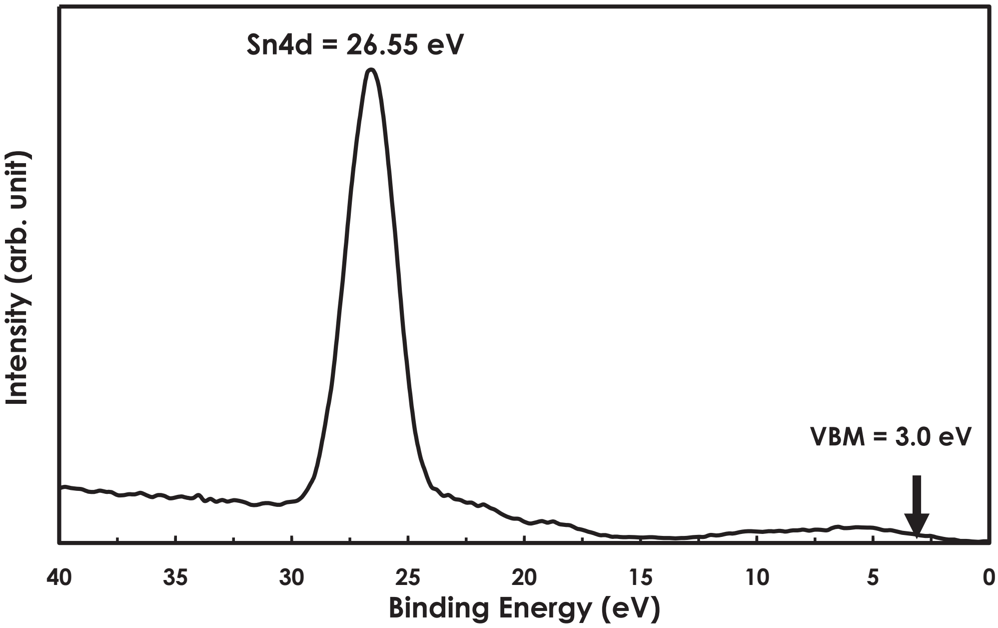

Fig. 5.8 Sn4d spectrum of the SnO$_2$ thin film annealed at 250^{o}C in air for 1 hour.

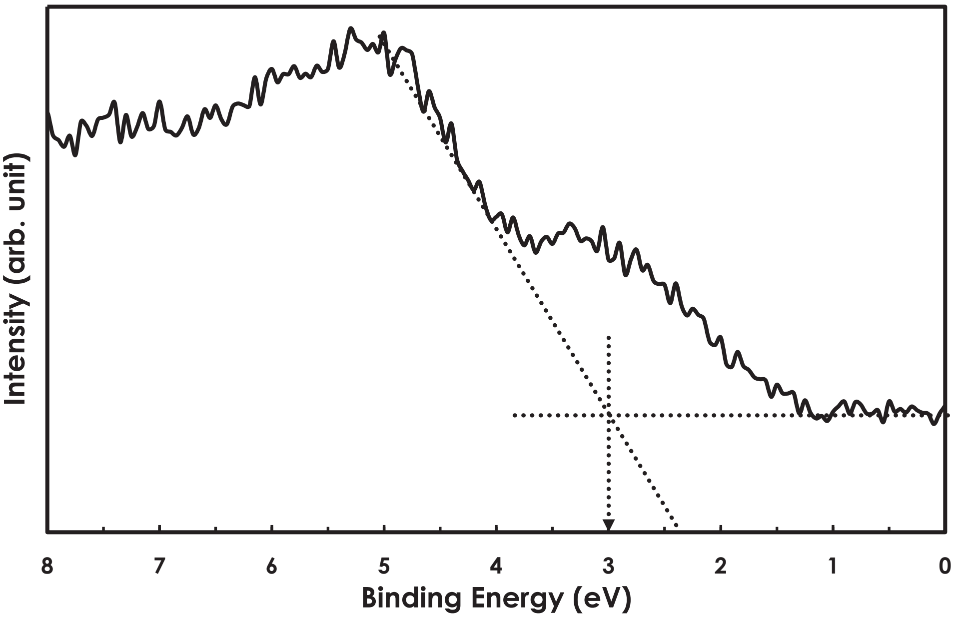

Fig. 5.9 The spectrum near the VBM in Fig. 5.7 is expanded to determine the VBM position of SnO$_2$.

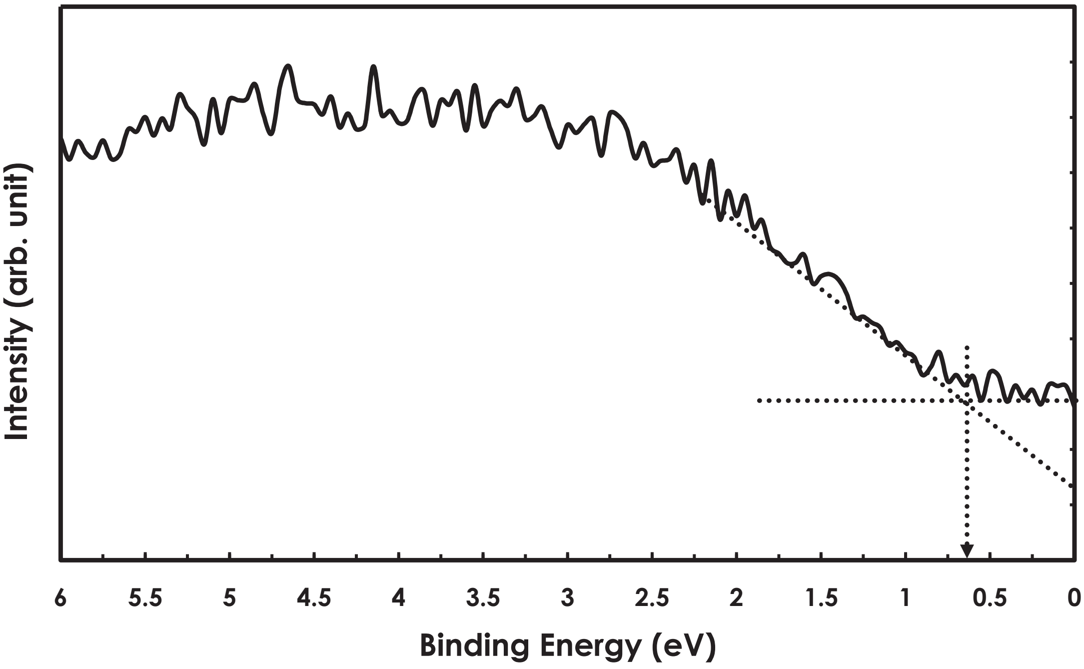

Fig. 5.10 The linear region in the VBM spectrum (Sn 4d) of SnS is extrapolated to determine the VBM position of the material.

The Sn 4d and VBM spectra of SnO_2 are shown in Figures 5.8 and 5.9, respectively. Two broad peaks are observed near 2.6 and 5.0 eV in the VBM spectrum. The peak near 5.0 eV can be extrapolated, as depicted in Fig. 5.9, to determine the VBM of the SnO_2 layer. The value of VBM was approximated to be 3.0 eV, and $E_{Sn4d} - E_v = 23.55$ eV. In addition, the weak signal near 2.6 eV may be associated to the Sn-derived surface states. Batzill *et al.* extensively studied these surface states on different SnO_2 surfaces through different treatments, such as annealing at high temperature and exposure to oxygen gas [27-28]. On the other hand, the VBM spectrum for the SnS layer showed only one broad peak centered at around 4.0 eV (as shown in Fig. 5.10). By extrapolation of the leading edge, the VBM of SnS was estimated to be 0.65 eV, and $E_{Sn4d} - E_v = 25.40$ eV, which is in good agreement with previous results [6].

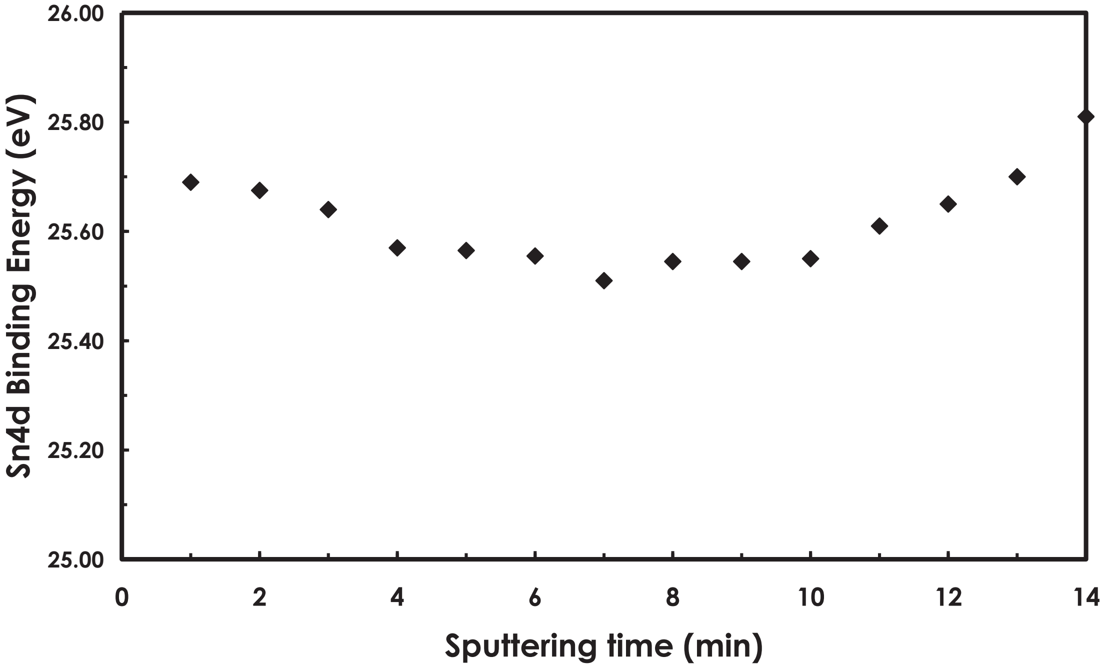

Fig. 5.11 Relative energy position of Sn4d levels for the SnS/SnO_2 heterojunction as a function of sputtering time.

The relative position of Sn 4d levels at SnS/SnO_2 interface is evaluated from the Sn 4d spectrum of the heterostructure to determine ΔE_{CL}. The spectra were taken repeatedly with continual Ar sputtering for the sample with a thin SnS over layer. It should be noted that after 14 min sputtering the In 4d peak near 18.25 eV from the ITO substrate started to appear in the spectrum. Additionally, the intensity of the S 2p and O 1s signals of the heterostructure decreases and increases with sputtering time, respectively. However, it is still difficult to identify the interface between SnO$_2$ and SnS based on those intensity variations. One possible reason is that the individual layers of the heterostructure have considerable roughness. The approximated energy positions of the Sn 4d levels for the SnS/SnO$_2$ heterojunction are shown in Figure 5.11. Considering the accuracy of XPS machine, the relative energy positions of Sn 4d levels are almost the same, that is, the energy position of Sn 4d levels for SnS/SnO$_2$ heterostructure is almost constant. This suggests that the core levels of SnO$_2$ and SnS might be assumed to coincide, i.e., $\Delta E_{CL} \approx 0$.

With the results on the relative energy position of Sn 4d levels of SnS and SnO$_2$ and the values of VBM of the individual layers, the valence band offset was found to be 1.85 eV. Using this value and the band gaps of individual layers, the conduction band minimum of SnO$_2$ is predicted to be higher than that of SnS by 0.65 eV. Thus, a Type-I heterostructure shown in Figure 5.12 was developed. Based on this structure, considerably large output voltage is expected to be attained for SnS/SnO$_2$ heterojunction. However, the values of solar cell parameters presented in the J-V curves under illumination did not confirm the possibility to have large open circuit voltage. The discrepancy can be explained from the presence of the defects in the SnO$_2$ layer in the form of surface states, as evidenced in the XPS spectrum in Fig. 5.9 (as described also in **Chapter 4**). These defects can contribute to the high density of interface states in the heterostructure and act as recombination centers for the current through the junction. Saad et al. reported that the presence of high interface density in the heterostructure can increase the junction ideality factor n ($n > 2$) and saturation current density due to the interface recombination, resulting in the decrease in V_{OC} and fill factor [29]. The n value obtained from the current-voltage (J-V) curve shown in Fig. 5.5 under dark condition is approximated to be 2.3 in the forward voltage range of $0 \text{ V} < V_{forward} < 0.1 \text{ V}$. This result indicates that the current is dominated by recombination at the interface defects.

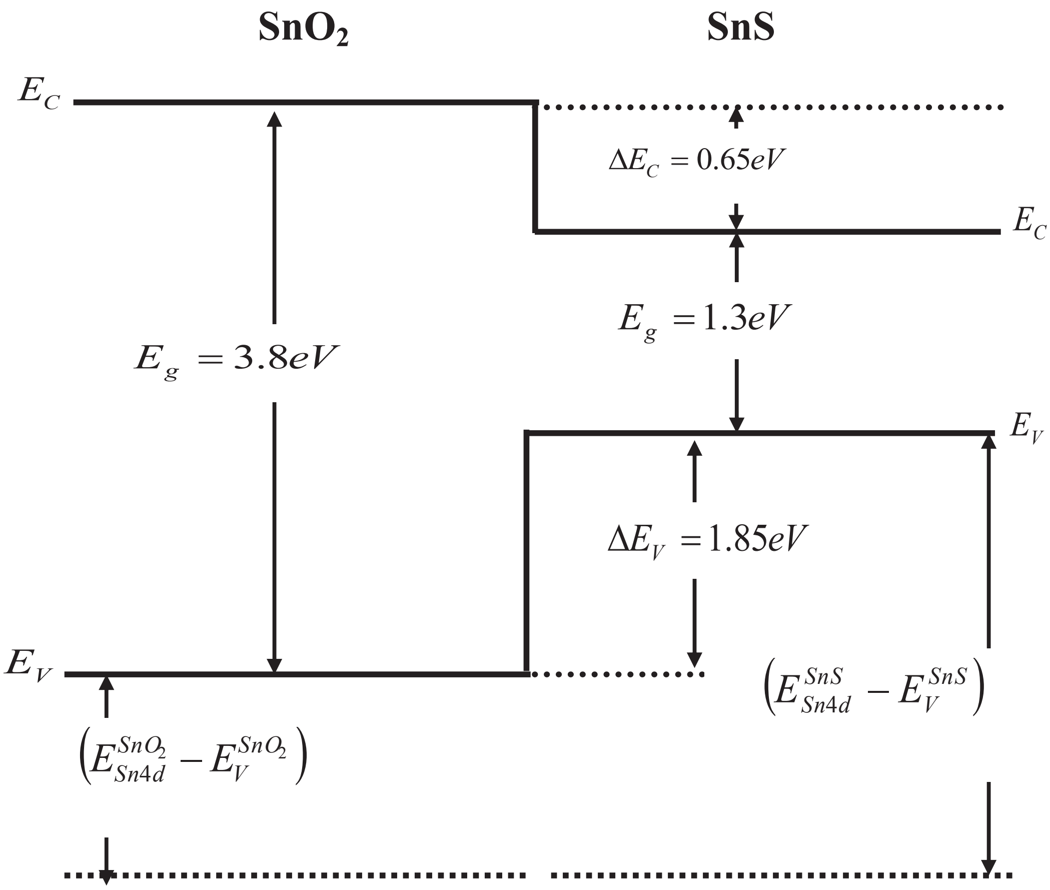

Fig. 5.12 Band alignment of SnS/SnO$_2$ heterostructure based on the results provided by XPS measurement. E_C and E_V are the CBM and VBM, respectively.

As noted in the introduction, Sugiyama et al. reported ΔE_v of 3.5 eV, significantly larger than the value obtained in this work (1.85 eV). According to their results, the SnS/SnO$_2$ heterojunction is Type-II, with VBM of SnS is very close to CBM of SnO$_2$. The reason of this discrepancy is not clearly understood. Since they used degenerate F-doped SnO$_2$, its metallic nature may influence the apparent band offset. If VBM of SnS nearly coincides with CBM of SnO$_2$, the junction will exhibit complete ohmic behavior. However, as shown in Figs. 5.4 and 5.6, rectification and photovoltaic properties were observed for the SnS/SnO$_2$ heterojunction. Therefore, it seems that ΔE_V was somewhat overestimated in their analysis.

5.4 Conclusions

SnS/SnO$_2$ heterojunction was successfully fabricated by electrodeposition method. As-deposited and annealed SnO$_2$ thin films had similar surface morphology with nearly stoichiometric Sn:O ratio. SnS films adhered well on annealed SnO$_2$ layer during the fabrication of SnS/SnO$_2$ bilayer. The fabricated heterojunction solar cells exhibited rectification and photovoltaic characteristics, but reproducibility was very poor. One of the reasons might be the presence of surface states in the SnO$_2$ layer as evidenced by the valence band XPS spectrum. The heterojunction showed a series resistance about 108.6 Ω, which is much higher than the reported values for highly efficient solar cells (usually << 1 Ω). The evaluated ΔE_V for SnS/SnO$_2$ heterostructure was 1.85 eV and a Type-I heterostructure was developed according to the obtained value of ΔE_V.

References

[1] T. Miyawaki and M. Ichimura: Mater. Lett. **61** (2007) 4683.

[2] M. Ichimura and K. Akita: Phys. Stat. Solidi C **7** (3-4) (2010) 929.

[3] M. Ichimura and H. Takagi: Jpn. J. Appl. Phys. **47** (2008) 7845.

[4] M. Ristov, G. Sinadinovski, M. Mitreski, and M. Ristova: Sol. Energy Mater. Sol. Cells **69** (2001) 17.

[5] Y. Wang, H. Gong, B. Fan, and G. Hu: J. Phys. Chem. C **114** (2010) 3256.

[6] A. M. Abdel Haleem and M. Ichimura: J. Appl. Phys. **107** (2010) 034507.

[7] K. T. Ramakrishna Reddy, N. Koteswara Reddy, and R. W. Miles: Sol. Energy Mater. Sol. Cells **90** (2006) 3041.

[8] H. Noguchi, A. Setiyadi, H. Tanamura, T. Nagatomo, and O. Omoto: Sol. Energy Mater. Sol. Cells **35** (1994) 325.

[9] M. Gunasekaran and M. Ichimura: Sol. Energy Mater. Sol. Cells **91** (2007) 774.

[10] D. Avellaneda, G. Delgado, M. T. S. Nair, and P. K. Nair: Thin Solid Films **515** (2007) 5771.

[11] B. Ghosh, R. Roy, S. Chowdhury, P. Banerjee, and S. Das: Appl. Surf. Sci. **256** (2010) 4328.

[12] M. Gunasekaran and M. Ichimura: Sol. Energy Mater. Sol. Cells **91** (9) (2007) 774.

[13] A. Sanchez-Juarez, A. Tiburcio-Silver, and A. Ortiz: Thin Solid Films **480** (2005) 452.

[14] F. Jiang, H. L. Shen, W. Wang, and L. Zhang: J. Electrochem. Soc. **159** (3) (2012) H235.

[15] M. Sugiyama, Y. Murata, T. Shimizu, K. Ramya, C. Venkataiah, T. Sato, and K. T. Ramakrishna Reddy: Jpn. J. Appl. Phys. **50** (2011) 05FH03.

[16] J. J. M. Vequizo, J. Wang, and M. Ichimura: Jpn. J. Appl. Phys. **49** (2010) 125502.

[17] S. T. Chang, I. C. Leu, and M. H. Hon: Electrochem. Solid-State Lett. **5** (2002) C71.

[18] Z. Zainal, M. Z. Hussein, and A. Ghazali: Sol. Energy Mater. Sol. Cells **40** (1996) 347.

[19] M. M Kamel and M. M. Ibrahim: J. Solid State Electrochem. **15** (2010) 683.

[20] S. Cheng, Y. Chen, Y. He, and G. Chen: Mater. Lett. **61** (2007) 1408.

[21] J. R. S. Brownson, C. Georges, and C. Levy-Clement: Chem. Mater. **18** (2006) 6397.

[22] N. R. Mathews, H. B. M. Anaya, M. A. Cortes-Jacome, C. Angeles-Chavez, and J. A. Toledo- Antonio: J. Electrochem. Soc. **157** (2010) H337.

[23] K. Omoto, N. Fathy, and M. Ichimura: Jpn. J. Appl. Phys. **45** (2006) 1500.

[24] F. Kang and M. Ichimura: Thin Solid Films **519** (2010) 725.

[25] E. A. Kraut, R. N. Grant, J. R. Waldrop, and S. P. Kowalczyk: Phys. Rev. Lett. **44** (1980) 1620.

[26] A. J. Nelson: J. Appl. Phys. **78** (1995) 5701.

[27] M. Batzill: Sensors **6** (2006) 1345.

[28] M. Batzill and U. Diebold: Prog. Surf. Sci. **79** (2005) 47.

[29] M. Saad and A. Kassis: Sol. Energy Mater. Sol. Cells **79** (2003) 507.

CHAPTER 6

Electrodeposition and Characterization of Ga-O Thin Films from Aqueous Gallium Sulfate Solutions

6.1 Introduction

Gallium oxide (Ga_2O_3) is considered as one of the most suitable materials for high temperature gas sensing due to its high melting point and stable structure. In addition, its wide band gap (~4.8 eV) [1] characteristics make it also applicable for solar cell fabrication, deep UV transparent conducting oxide [2], anti-reflection [3] and passivation coatings [4]. Ga_2O_3 could exist in five different crystalline phases, among which are well known α-, β-, γ-, δ-, and rare ε-structures. The most stable form is the monoclinic structured β-Ga_2O_3 [5].

Several methods such as sol-gel [5-7], spray pyrolysis [8], molecular beam epitaxy (MBE) [9], pulsed laser deposition (PLD) [10], plasma enhanced atomic layer deposition (PEALD) [11], and chemical vapor deposition (CVD) [12] have been performed to prepare Ga_2O_3 thin films. Recently, Ga_2O_3-based nanostructured materials: nanorods, nanobelts, nanotubes, and nanowires [13-17] have attracted a great deal of attention due to their fascinating properties such as superior catalytic behavior [18] and enhanced luminescence efficiency [19]. The growth or deposition of Ga_2O_3 nano- or micron-sized structures may involve either direct thermal activation of Ga and O precursors or indirect process that follows the growth of intermediary products such as gallium oxide hydroxide (GaOOH) or gallium hydroxide [$Ga(OH)_3$] from the starting precursors. Calcination of these intermediaries at higher temperature can produce Ga_2O_3 as product. Interestingly, researches on GaOOH have been increasing rapidly due to its significant role in the synthesis of Ga_2O_3 and gallium nitride (GaN) materials. Extensive studies have been carried out to GaOOH nanostructures for optoelectronics and photonics applications [6, 20-22]. Rod-like GaOOH nanostructures can be done by hydrothermal synthesis and chemical solution deposition

(CSD) [23-24]. Recently, GaOOH nanorods have been synthesized by electrodeposition from gallium nitrate-ammonium nitrate aqueous solution at elevated temperature of 80^{o}C [25]. Moreover, several works are devoted to the preparation of GaS_xO_y thin films via electrodeposition [26] and photochemical deposition (PCD) [27] methods from the solutions containing gallium sulfate [$Ga_2(SO_4)_3$] and sodium thiosulfate ($Na_2S_2O_3$). In these works, it is found that the addition of $Na_2S_2O_3$ in the solution favors the inclusion of S forming GaS_xO_y instead of Ga_2O_3 thin films. The reaction mechanism is reported to be similar to the deposition of other sulfide-based semiconductors that involves release of sulfur from thiosulfate ions [28-31].

In this recent study, gallium sulfate [$Ga_2(SO_4)_3$] and hydrogen peroxide (H_2O_2) are utilized to electrodeposit Ga-O thin films. The role of H_2O_2 as an oxygen source has been considered and investigated in ZnO thin films electrodeposited from the following solutions: $ZnCl_2$-LiCl-H_2O_2 [32] and $ZnCl_2$-KCl-H_2O_2 [33]. Additionally, the significant contribution of H_2O_2 on the electrodeposition of zinc peroxide (ZnO_2) from $Zn(NO_3)_2$-H_2O_2 working solution has been studied and reported [34]. In their work, the suggested reaction mechanism involves: (a) production of OH^- ions from H_2O_2 (along with NO_3^- ions) reduction on the substrate surface and (b) reaction of H_2O_2 with $Zn(OH)_2$ to form ZnO_2 (H_2O_2 serves as an oxygen source). Moreover, Uekawa et al. reported and prepared ZnO_2 from the dispersed solution of $Zn(OH)_2$ precipitates in H_2O_2 solution [35]. The above findings led us to employ hydrogen peroxide as a suitable oxygen precursor to deposit Ga-O thin films.

This work aims to present and explain the deposition results of Ga-O thin films from aqueous $Ga_2(SO_4)_3$-H_2O_2 medium at room temperature according to the following deposition parameters: amount of H_2O_2, applied potential and deposition time. Annealing in air from 300 to 600^{o}C temperatures is also considered to study its effect on the composition, morphology and quality of the films. Additionally, the results of the fabrication of Ga-O based heterostructures are also presented and discussed. The fabrication of Ga-O based heterojunctions is performed by employing step by step electrodeposition of individual layers. The solar cell performance in the fabricated heterostructures is then evaluated from the corresponding current-voltage characteristics obtained after evaporation of indium (In) metal electrodes as contacts.

6.2 Experimental Procedure

6.2.1 Electrodeposition and characterization of Ga-O thin films

Ga-O thin films were electrodeposited on fluorine-doped tin oxide (FTO) coated glass substrate using the typical three-electrode electrochemical cell with FTO, platinum sheet, and saturated calomel electrode (SCE) as working, counter, and reference electrodes, respectively. As noted and observed in Ref. 26, no noticeable deposition was obtained from the solution containing $Ga_2(SO_4)_3$ only and without oxygen bubbling. Instead, the substrate undergone reduction (it turned black) during cathodic electrodeposition. Furthermore, with dissolved oxygen, which was carried out by oxygen gas bubbling, similar substrate reduction effect occurred upon applying the reduction potential. These observations suggested that the substrate was not stable in these solution conditions. However, by adding a suitable amount of H_2O_2 in the non-bubbled solution, the substrate reduction was prevented to happen. Hence, an aqueous solution containing 20 mM $Ga_2(SO_4)_3$ and H_2O_2 (taken from 9.79 M H_2O_2 solution) was considered and prepared to electrodeposit the Ga-O films. H_2O_2 was added in small amount before the start of the deposition experiment. All depositions were carried out at room temperature, normal pH (~2.52), and quiescent solution. Prior to electrodeposition, FTO substrate was ultrasonically cleaned in alkyl benzene, subsequently rinsed in pure water, and finally dried by nitrogen purging. After depositions, freshly electrodeposited Ga-O films were naturally dried in air ambient. Cyclic voltammetry (CV) was carried out to decide the suitable applied voltage. Deposition time was varied from 2 - 10 min.

Compositional analysis and surface morphology studies were performed using a JEOL JAMP-9500F field emission Auger microprobe at a probe voltage of 10 kV and a current of 1.0×10^{-8} A. Argon ion etching was done using an acceleration voltage of 2 kV with ion current of 2.6 μA to sputter the film' surface. The Auger electron spectroscopy (AES) spectra were recorded and analyzed after 10 s sputtering with a rate of 9.5 nm/min. The composition ratio (O/Ga) was calculated using standard Ga_2O_3 compound (with O/Ga ~ 1.5). The crystalline structure of the sample was characterized by X-ray diffraction (XRD), which was carried out using a SmartLab

[X-ray Diffractometer]. The thickness of the films was measured using an Accretech Surfcom-1400D profilometer. A JASCO U-570 ultraviolet/visible/near infrared (UV/vis/NIR) spectrometer was used for optical transmission studies from 300 – 900 nm wavelengths with the FTO substrate as the reference.

6.2.2 Fabrication of Ga-O-based heterojunction solar cells

The as-deposited and annealed Ga-O thin films are utilized to fabricate Ga-O-based heterostructures. SnS and Cu_2O are considered to be the *p-type* absorber layers to form a *p-n* heterojunction. Both *p-type* layers are electrodeposited on top of either as-deposited or annealed Ga-O thin films to fabricate SnS/Ga-O and Cu_2O/Ga-O superstrate heterostructures. Indium electrodes are then evaporated on top of the absorber layer and on FTO to provide electrical contacts during current-voltage (J-V) characterizations. The photovoltaic performance of these heterostructures are investigated and evaluated from the obtained J-V curves of the fabricated SnS/Ga-O and Cu_2O/Ga-O heterojunctions. Illumination condition is carried out using a solar-simulated light source with an intensity of 100 mW/cm^2.

6.3 Results and Discussion

6.3.1 Cyclic voltammetry

Figure 6.1 shows the CV curve obtained from the $Ga_2(SO_4)_2$-H_2O_2 solution at normal pH. From this graph, the current response is recorded against applied voltage (V vs SCE), which is scanned in a triangular form. The cathodic scan starts from 0 to -1.5 V and the anodic scan is from -1.5 to +0.5 and back to 0 V at a constant scan rate of 20 mVs^{-1}. As seen in Fig. 6.1, a gradual increase in current density was observed from -0.1 to -0.5 V and a cathodic peak appeared at around -0.68 V. The existence of this cathodic peak was not observed in the CV curve for H_2O_2-free solution, that is, only small and constant (plateau-type) cathodic current density is obtained at this potential region. Hence, the cathodic peak seen in Fig. 6.1 could be associated to the reduction of H_2O_2. In the anodic scan, no perceivable anodic peak was observed. Try-test depositions were performed to decide the suitable deposition potential.

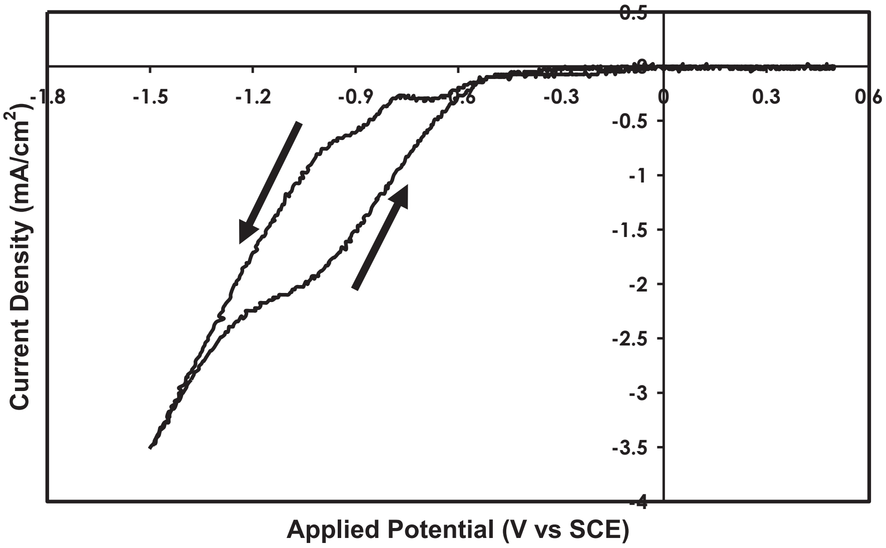

Fig. 6.1 CV curve obtained from $Ga_2(SO_4)_3$ - H_2O_2 aqueous solution. The voltage scan rate is 20 mVs^{-1}. The directions of the arrows correspond to the cathodic (down) and anodic (up) scans, respectively.

For 5 min deposition, no considerable film thickness was attained at potentials more positive than -1.0 V. This signifies that large overpotential is needed to activate the reaction on the FTO substrate. It should be noted that the formation of the film on the substrate depends on the available reduced species near the substrate during electrodeposition. For higher deposition potential, the OH^- ions produced during electroreduction are expected to be large. Thus, short deposition time is needed to form the film on the substrate. Hence, the chosen potential values are more negative than or equal to -1.0 V.

6.3.2 H_2O_2 optimization

Initially, -1.2 V was considered as the applied potential to optimize the amount of H_2O_2, which was added in small amount: 0.13-0.28 mL. It should be noted that all the prepared solutions were clear and transparent before, during and after deposition. No noticeable precipitation was observed. All the as-deposited films appeared translucent under transmitted light. Higher amount of H_2O_2 in the solution (0.16-0.28 mL) resulted to higher degree of non-uniformity and roughness. This observation could be attributed to the rapid reaction, which is represented by the bubbling effect or oxygen gas generation in the solution that occurred during deposition. It was confirmed further that by adding much higher amount (1.0-2.0 mL) of H_2O_2, the reaction was so violent. The thickness of these films ranges from 0.40 – 0.75 μm over an entire deposition area. On the other hand, for 0.13 mL of H_2O_2 in the solution, relatively uniform thickness of about 0.5 μm was obtained. In the succeeding results, the amount of H_2O_2 added in the solution is kept constant at 0.13 mL and other parameters such as applied potential and deposition time were varied to investigate their effects on the morphological and compositional properties of the films.

6.3.3 As-prepared Ga-O thin films: Thickness, surface morphology and AES analysis

Table 6.1 gives the approximated thickness and the surface morphology type (crack morphology, CM or crack-free morphology, CFM) of the samples deposited at -1.2, -1.1 and -1.0 V at different deposition times. At potential of -1.2 V, the deposition rate is close to 0.1μm/min, which is higher than the rate at lower potential (about 30 - 60 nm/min). The different cathodic potential provides different amount of electrons for the deposition reaction. Higher applied potential promotes the generation of OH^- by electrochemical reduction of H_2O_2 near the cathode. Thus, it is expected that the surface density of the film is increased and the deposition rate is accelerated. Furthermore, the agglomeration or coalescence of smaller grains could be intensified at higher potential and longer deposition time. Hence, an increase of surface roughness along with the deterioration of the film quality can be attained under this condition.

Figure 6.2 shows the surface morphologies of the as-prepared samples deposited at -1.2 V for (a) 5 and (b) 2 min, (c) at -1.1 V for 2 min and (d) at -1.0 V for 5 min. As evident in Fig. 6.2(a), crack morphology with coalescence of smaller grains on the background film is observed. Although the aggregation is reduced for 3 min deposition at the same potential of -1.2 V, but the crack-morphology is still observed. On the other hand, crack-free surfaces are attained for 2 min deposition at applied potentials of -1.2 and -1.1 V. Similar crack-free, smooth surface, and good surface coverage as in Fig. 6.2(c) are also observed at -1.0 V for 5 min as shown in Fig. 6.2(d). Moreover, extending the deposition time to 10 min at -1.0 V could still produce crack-free surface as shown in Fig. 6.2(e), but rough films with aggregation could be obtained. The crack-free morphologies seen in Fig. 6.2 (b-d) are related to the attained total film thickness as reflected in Table 6.1. This implies that thinner films avoid the possibility to have crack morphologies.

Deposition voltage (V)	Deposition time (min)	Thickness (μm)	Surface morphology
-1.2	5	0.50	CM
	3	0.25~0.35	CM
	2	0.10~0.15	CFM
-1.1	5	0.20~0.30	CM/CFM
	3	0.10~0.15	CFM
-1.0	10	0.25~0.30	CFM
	5	0.15~0.20	CFM
	3	0.10~0.15	CFM

Table 6.1 Approximate thickness and surface morphology type denoted by CM (crack-morphology) and CFM (crack-free morphology) of the samples deposited at different potentials and deposition times.

Figure 6.3 shows the AES spectra of the films deposited at -1.2 and -1.0 V for 2 and 5 min, respectively. These spectra were recorded after 10 s sputtering of the film surface. Sputtering was carried out to remove unwanted carbon or other impurities. As evident in the spectra, Ga and O peaks are clearly observed. The estimated O/Ga ratio is about 2.0 (referenced to standard Ga_2O_3) for both samples. These O/Ga values may signify GaOOH formation on the substrate.

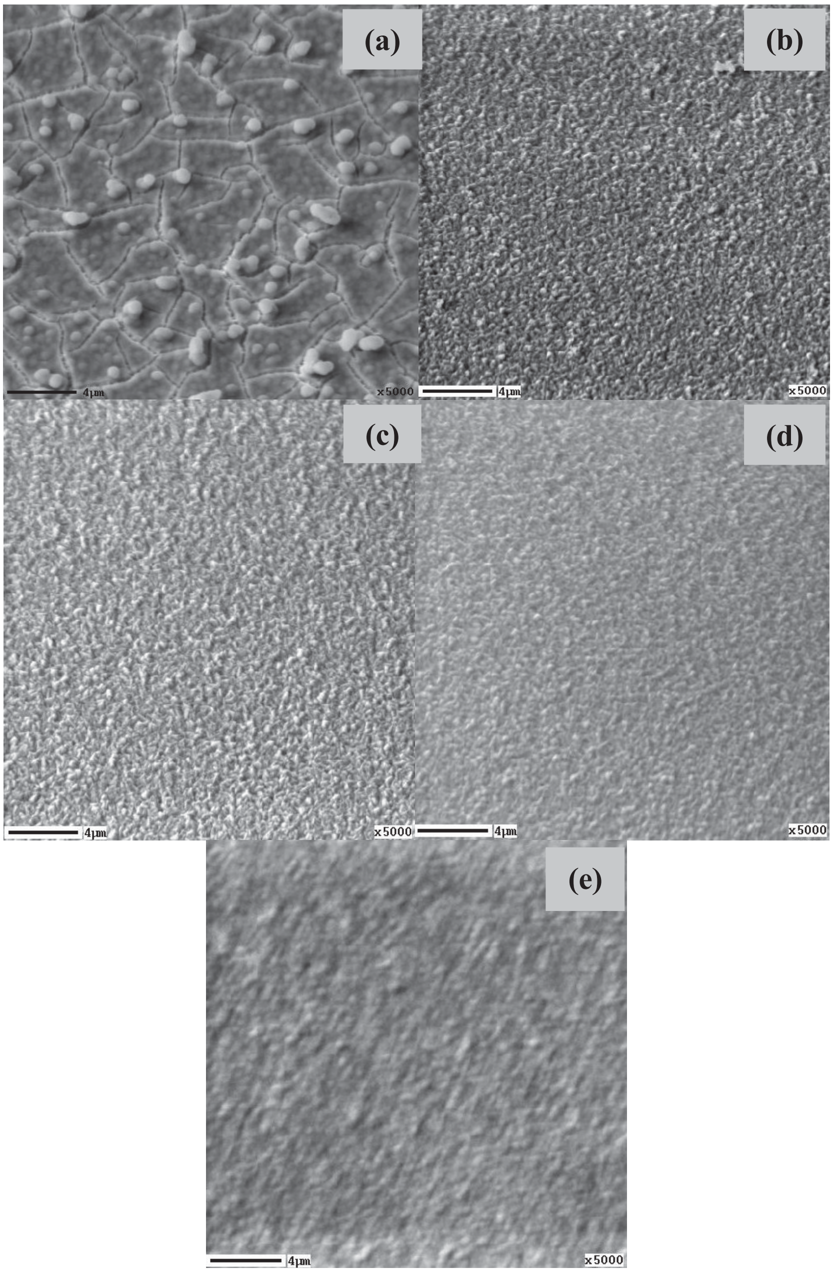

Fig. 6.2 SEM images of as-deposited Ga-O thin films deposited at -1.2 for (a) 5 and (b) 2 min, (c) at -1.1 V for 2 min, at -1.0 V for (d) 5 and (e) 10 min.

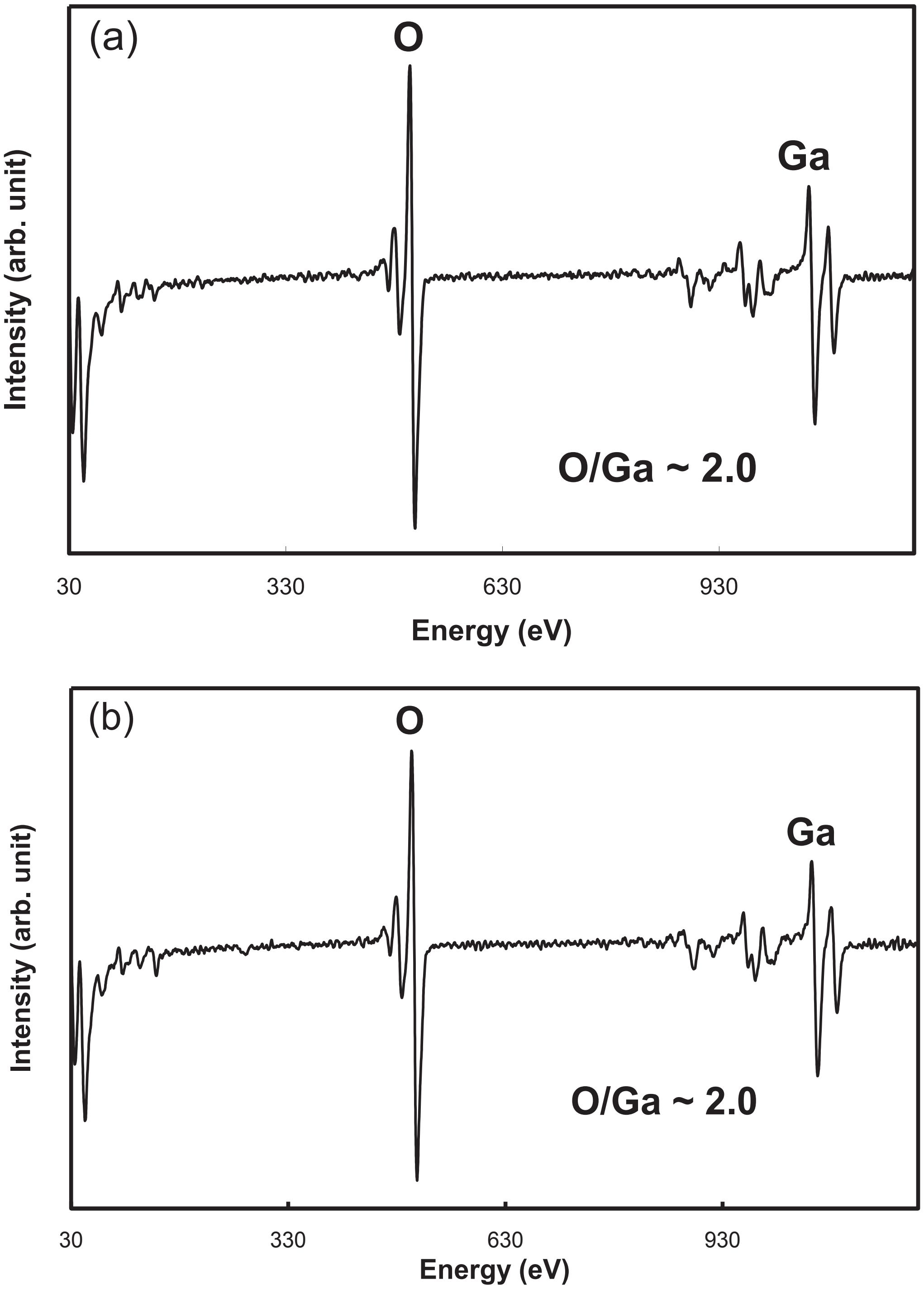

Fig. 6.3 AES spectra of as-prepared Ga-O thin films deposited at (a) -1.2 for 2 min and (b) -1.0 V for 5 min.

Similar Auger spectra as shown in Fig. 6.3 are attained for as-prepared samples deposited at -1.1 V for 2 min and -1.0 V for 10 min.

6.3.4 Thin film formation

The formation of Ga-O thin films from aqueous gallium sulfate solution at room temperature on FTO substrate by electrodeposition is mainly based on the generation of OH^- ions at the cathode. When a certain cathodic voltage is applied, the OH^- ions are produced near the cathode by electrochemical reduction of starting precursors such as hydrogen peroxide and dissolved oxygen (O_2). For H_2O_2-free solution and under dissolved O_2 condition (oxygen gas was bubbled through the solution until saturation), the substrate still undergoes reduction during electrodeposition and no film formation is attained. Thus, the apparent reaction that produces OH^- ions in Ga^{3+} + H_2O_2 aqueous solution could be due to the electroreduction of H_2O_2. Then, the Ga^{3+} ions react with the electrochemically produced OH^- ions to form GaOOH. These reactions can be represented by

$$H_2O_2 + 2e^- \rightarrow 2OH^-, \tag{6.1}$$

$$Ga^{3+} + 3OH^- \rightarrow GaOOH + H_2O. \tag{6.2}$$

The formation of GaOOH represented in reaction (6.2) is entirely different from the approach employed and reported in Ref. 23 according to the following considerations: (a) OH^- is generated first due to H_2O_2 electroreduction represented by reaction (6.1); (b) Deposition is carried out at room temperature; and (c) Relatively short deposition time is needed to deposit the GaOOH thin films. Thus, the method employed in this study deviates from the chemical solution deposition approach, which involves thermohydrolysis of Ga^{3+} in heated aqueous solutions, carried out in Ref. 23. Moreover, the deposition procedure followed in this work is also different from the process employed in Ref. 25 to deposit GaOOH nanorods on ITO substrate with thin layer of antimony-doped SnO_2 (ATO) according to considerations (a), (b), and (c). For instance, in their work, the OH^- ions are generated by electroreduction of nitrate ions, which are present in the solution. Hence, this work suggests different approach to deposit Ga-O based thin films.

6.3.5 Annealed Ga-O thin films: Morphological and compositional studies

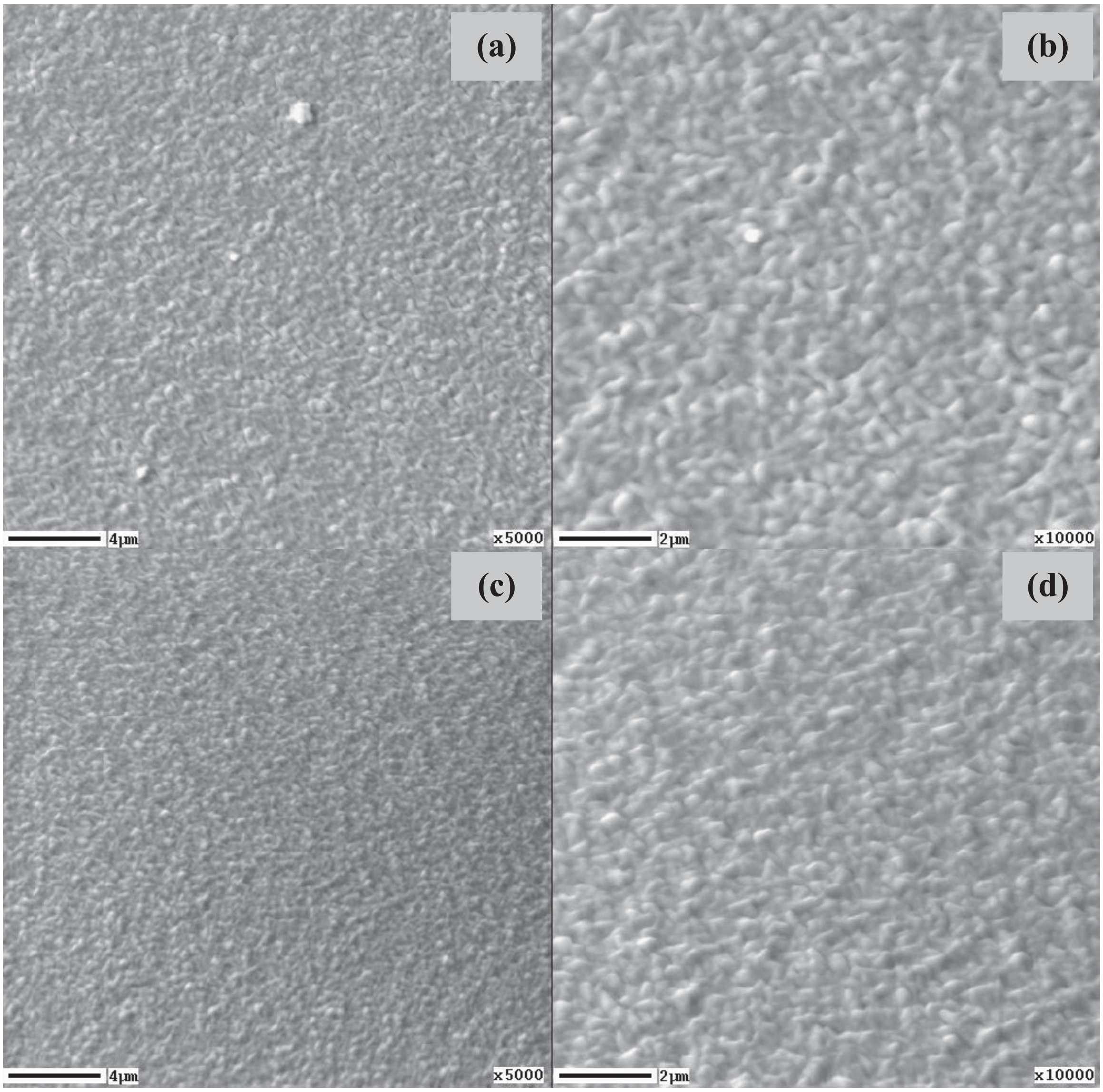

Fig. 6.4 Surface morphologies of Ga-O thin films annealed at temperatures 600 (a, b) and 300°C (c, d). (a, c) at low magnification and (b, d) at high magnification.

The thermal treatments of as-deposited Ga-O thin films were carried out by simple annealing process in ambient air for 1 h at 300-600°C to investigate its effect on the morphology and composition. Annealed Ga-O thin films (as shown in Figure 6.4) retained the same morphology as that of as-deposited Ga-O thin films after thermal treatment.

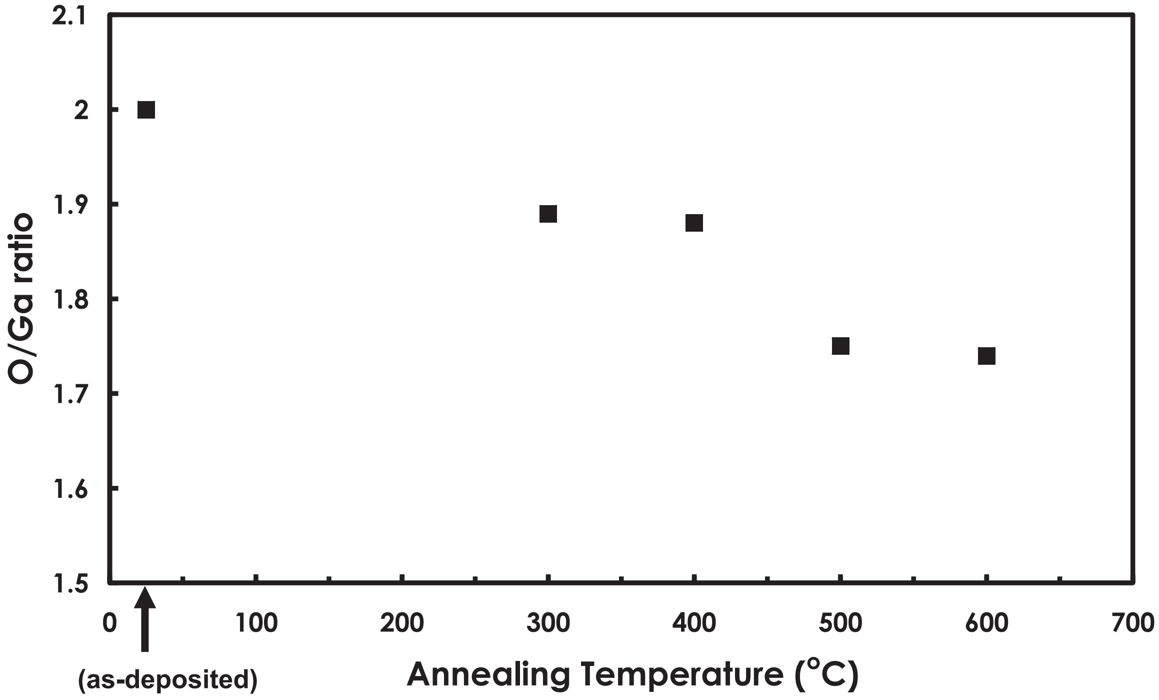

Fig. 6.5 Estimated compositional ratio (O/Ga) plotted against annealing temperature of the Ga-O samples deposited at -1.0 V.

The estimated O/Ga ratios of the samples deposited at -1.0 V for 5 min are plotted against annealing temperature and shown in Figure 6.5. As seen in this plot, the O/Ga ratios slightly reduced after 300-400°C annealing and closer to stoichiometric Ga_2O_3 after annealing at 500-600°C. This decrease could be associated to the decomposition of GaOOH by annealing. Thermal decomposition of GaOOH forming Ga_2O_3 at 400°C has been reported and demonstrated in previous works on GaOOH [6, 13, 23, 36-38]. The decomposition of GaOOH can be expressed as

$$2GaOOH \rightarrow Ga_2O_3 + H_2O. \tag{6.3}$$

Reaction (6.3) is similar to reaction (2) in Ref. 23. Along with the decomposition due to thermal treatment, the thickness of the film decreases after annealing. For instance, 0.5 μm film thickness reduced to 0.25 μm after annealing at 600°C for 1 h. However, in this work, thermal annealing at temperature higher than 600°C could not be performed because the FTO substrate cracked or broke in this temperature range.

6.3.6 XRD analysis and optical transmission study

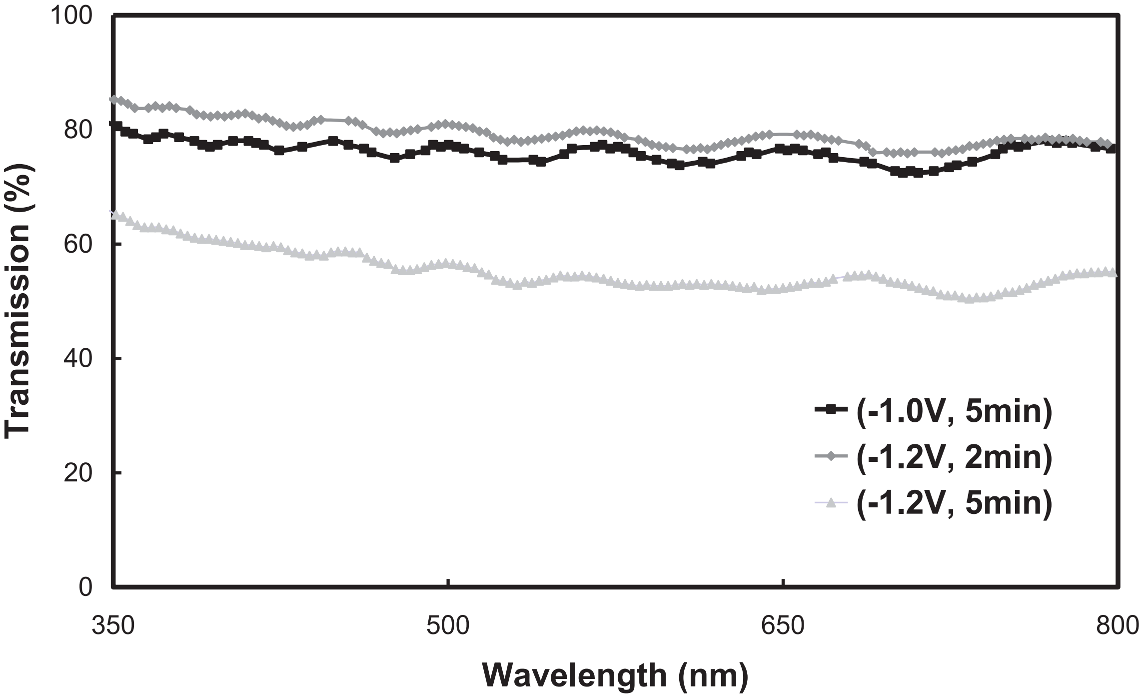

Fig. 6.6 Optical transmission of as-deposited Ga-O thin films deposited at -1.2 V for 5 and 2 min and at -1.0 V for 5 min.

Figure 6.6 exhibits the optical transmission (in %) of the as-prepared sample deposited at -1.2 and -1.0 V. Relatively good transparency (~ 80 %) in 350-800 nm wavelength is obtained for thinner samples (~ 0.15-0.20 μm). Additionally, for sample deposited at -1.2 V and same deposition time (5 min), the transmission decreases to about 60 % in the same wavelength range. This decrease is attributed to the increase of thickness as reflected in the Table 6.1 shown in section 6.3.3. No absorption edge was attained because the FTO substrate has an optical absorption edge between 300 - 350 nm. Hence, the band gap of as-prepared Ga-O thin film could not be estimated in this work. Sinha et. al found that the band gap value for thin film-based GaOOH is 5.27 eV with absorption edge between 200 – 300 nm [5].

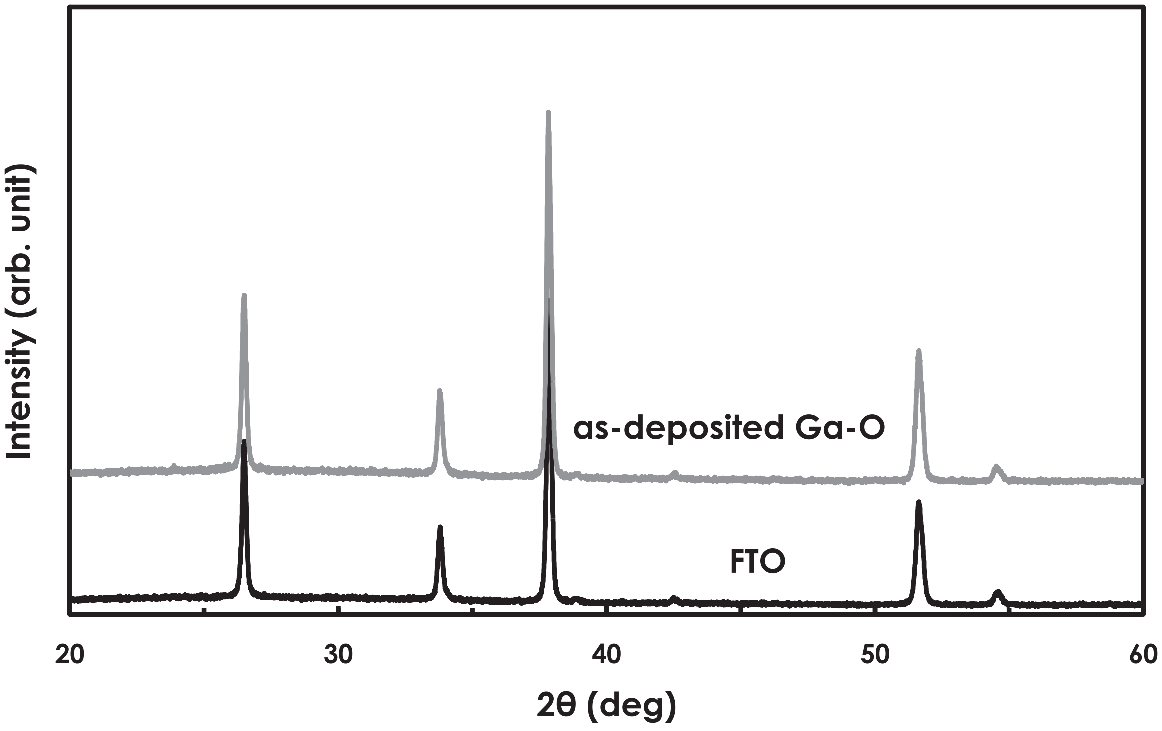

Fig. 6.7 XRD patterns of as-deposited Ga-O thin films and FTO substrate.

Figures 6.7 and 6.8 depict the XRD patterns of the as-deposited and 600°C-annealed Ga-O thin films with the typical XRD peaks of FTO substrate. As can be seen in the patterns of as-deposited and annealed Ga-O samples, only FTO (110), (101), (200) and (211) prominent peaks were observed and no perceivable peaks associated to GaOOH or Ga_2O_3 are observed. These suggest that the as-prepared and annealed samples are either consist of very fine grains (nanocrystalline) or amorphous in nature.

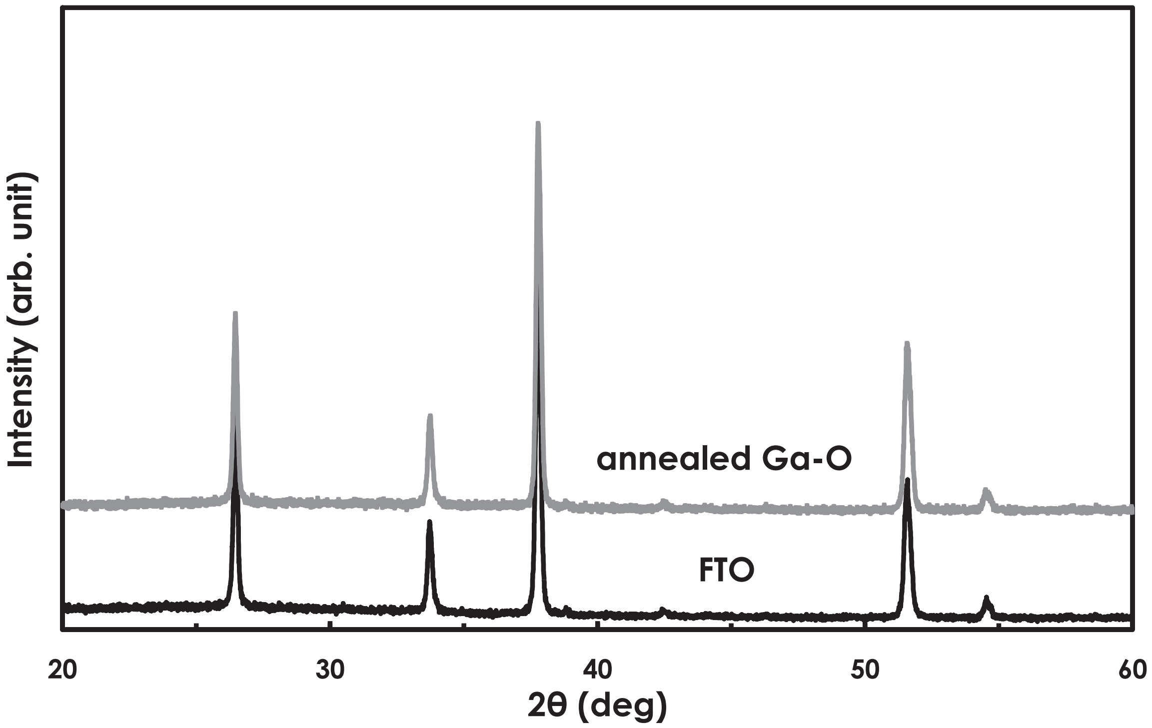

Fig. 6.8 XRD patterns of 600°C-annealed Ga-O thin films and FTO substrate.

6.3.7 Fabrication of SnS/Ga-O and Cu_2O/Ga-O heterostructures

The electrodeposited Ga-O thin films (as-deposited and annealed) are utilized and partnered with electrodeposited *p-type* SnS and Cu_2O thin films to fabricate heterojunction solar cells. The SnS/Ga-O and Cu_2O/Ga-O heterostructures are fabricated by step-by-step electrodeposition (ED) of individual layers, that is, after depositing the Ga-O film as window layer, SnS or Cu_2O absorber layer is then electrodeposited on top of the window layer.

For SnS deposition, a three-step pulsed electrodeposition (with potentials V_1 = variable, V_2 = -0.6 V and V_3 = 0 V at equal pulse time of $t_1 = t_2 = t_3 = 10$ s) is employed for 20 min using FTO/Ga-O as the working electrode. The solution contains 30 mM $SnSO_4$ and 100 mM $Na_2S_2O_3$. For potentiostatic electrodeposition of SnS absorber layer on Ga-O, cyclic voltammetry (CV) is usually carried out to decide the suitable potential. This preliminary step is essential in the fabrication of *p-n* heterostructures via step-by-step electrodeposition method. The CV curves for

SnS on FTO and SnS on Ga-O thin film is shown in Figure 6.9 from $SnSO_4$-$Na_2S_2O_3$ aqueous solution at room temperature. It should be noted that the SnS deposition condition is adopted from the work of Naglaa Fathy et al. on electrodeposition of SnS [39] with varied V_1. As depicted in Fig. 6.8, the onset of the reduction potential for SnS on Ga-O is slightly shifted towards more negative potential compared to that on FTO only. However, the reduction peak is situated at almost the same potential (~ -0.9 V vs SCE). Hence, the suitable potential values obtained in SnS deposition on FTO can also be utilized in the electrodeposition of SnS on Ga-O. The decrease in the observed reduction current density for SnS on Ga-O film is due to the presence of Ga-O layer. The total resistive property of Ga-O/FTO is expected to be higher than that of bare FTO. Thus, the measured deposition current density is lower in SnS/Ga-O deposition configuration. However, preliminary fabrication of SnS/Ga-O heterostructure revealed that no good SnS layer (not continuous over the entire area) is attained using the as-deposited Ga-O film. Hence, thermal treatment is tried on Ga-O film prior to SnS deposition to fabricate SnS/Ga-O heterojunction.

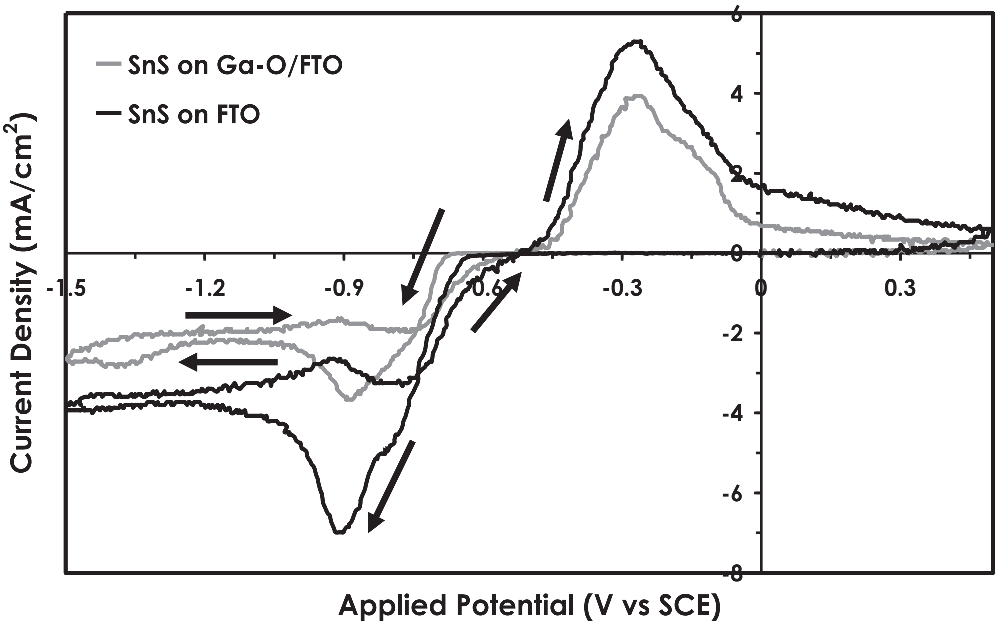

Fig. 6.9 Cyclic voltammetry curve for SnS on Ga-O film obtained from $SnSO_4$ and $Na_2S_2O_3$ aqueous solution at room temperature. The potential is scanned at a rate of 20 mVs^{-1}. The arrows represent the direction of the cathodic and anodic scans.

For Cu_2O/Ga-O heterostructure, galvanostatic electrodeposition is performed to deposit Cu_2O over the as-deposited and annealed Ga-O thin films from aqueous basic solution containing 0.2 M $CuSO_4$, 1.6 M lactic acid, and KOH solution (for pH adjustment to 12.5). The Cu_2O deposition condition is adopted from the work of Ichimura and Song on step-by-step electrodeposition of Cu_2O/ZnO heterojunction solar cells [40-41]. In galvanostatic ED, a constant current density (-1.0 mA/cm^2) is applied on the electrochemical system for 10 min with Ga-O/FTO as the working electrode. The annealing condition for Ga-O layer is at 400 ^oC in ambient air for 1 hour. After the electrodeposition of the *n-* and *p-type* layers, indium electrodes are then evaporated on top of the absorber layer and on FTO to provide electrical contacts for current-voltage characterizations.

6.3.8 Current-voltage characterizations of SnS/Ga-O and Cu_2O/Ga-O heterostructures

The current-voltage (J-V) profiles of the SnS/Ga-O heterostructure with SnS deposition potential of under dark and light conditions are displayed in Figure 6.10. As seen in Fig. 6.10 (a), SnS/Ga-O configuration with 400^{o}C-annealed Ga-O and SnS deposited at V_1 = -1.2 V vs SCE shows some rectifying behavior. Photocurrent is observed under illumination; however, no photovoltaic characteristics are achieved after expanding the region near 0 V. The measured current density for the heterostructure is too large. Moreover, at less negative V_1 (-1.1 V vs SCE) for SnS deposition, the SnS/Ga-O heterojunction depicts very poor rectification (nearly ohmic behavior) as seen in Fig. 6.10 (b).

Figure 6.11 shows the J-V characteristics for the fabricated Cu_2O/Ga-O superstrate heterostructures. Photoresponse is clearly observed under illumination condition. The heterojunctions displays rectifying behavior and photovoltaic characteristics. The solar cell parameters: open circuit voltage (V_{OC}) and short circuit current density (J_{SC}) are approximately 0.15 V and 0.35 mA/cm^2, respectively; for heterostructure with as-deposited Ga-O layer. Slight increase in the values of the V_{OC} (0.22 V) and J_{SC} (0.45 mA/cm^2) is obtained for the configuration with the annealed Ga-O film as the window layer. This slight improvement could be due to improved morphology after annealing or in the crystallinity. It is well known that with appropriate annealing condition, enhancement of the morphology and crystallinity of the thin films can be achieved. The estimated conversion efficiency η is (1.3 and 2.5) x 10^{-2} % for heterostructures with as-deposited and annealed Ga-O layers, respectively.

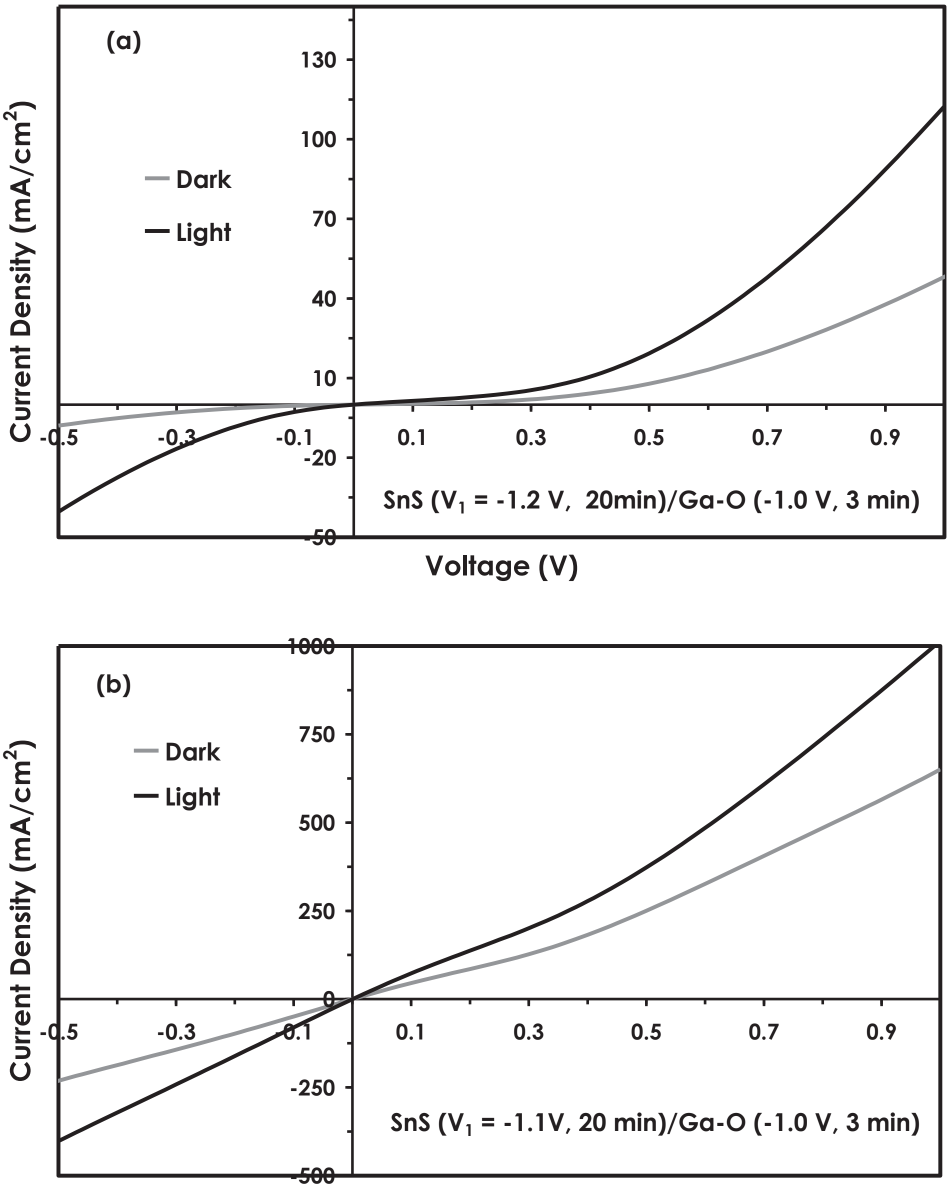

Fig. 6.10 Current-voltage characteristics of SnS/annealed-Ga-O heterojunctions with SnS deposition potential V_1 (a) -1.2 and (b) -1.1 V and Ga-O layer is annealed at 400°C for 1 h.

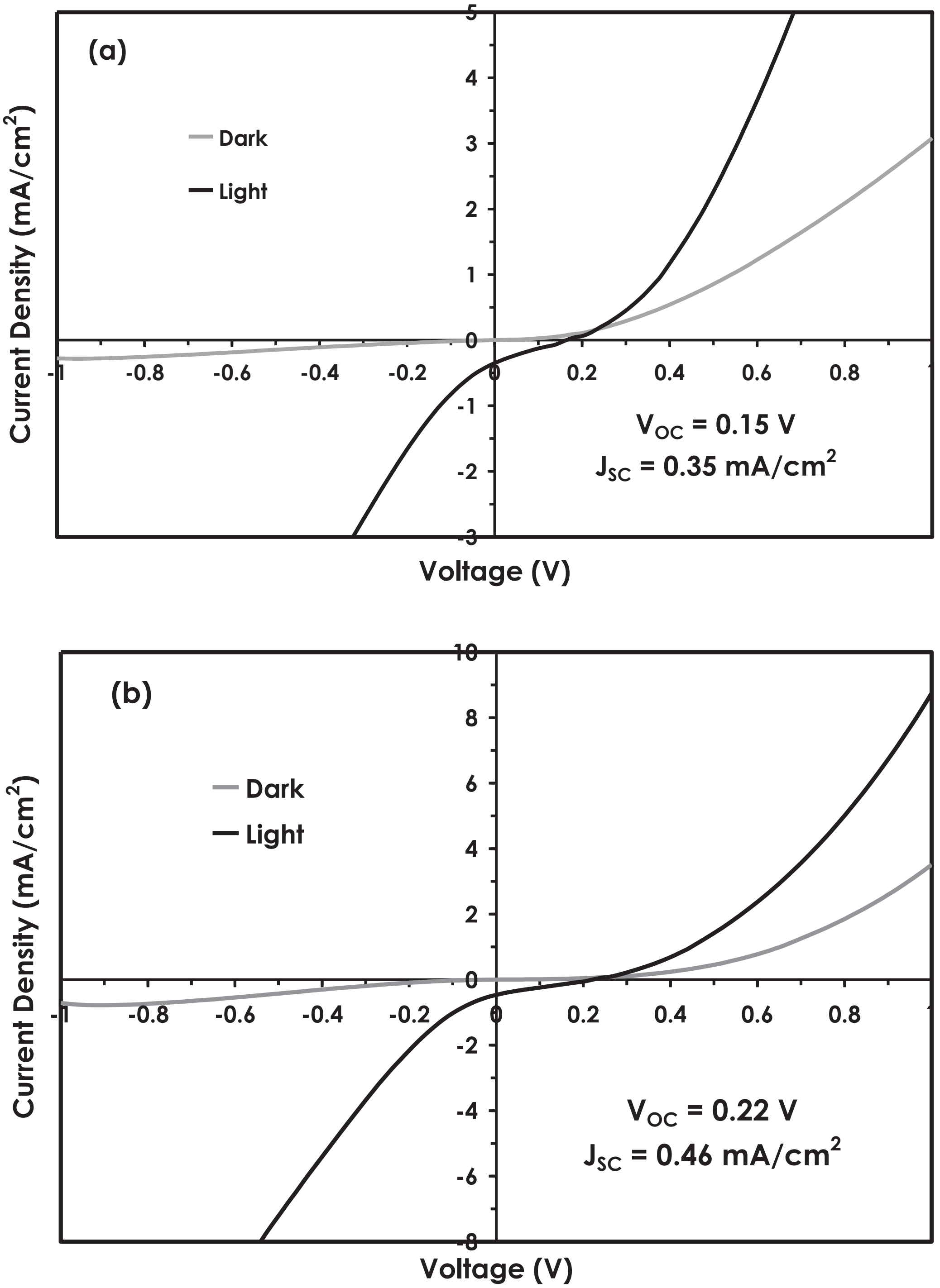

Fig. 6.11 Current-voltage (J-V) characteristics of Cu_2O/Ga-O heterostructures with (a) as-deposited and (b) 400°C-annealed Ga-O window layers.

6.4. Conclusions

Ga-O thin films were electrodeposited on FTO substrate from an aqueous $Ga_2(SO_4)_3$-H_2O_2 solution. It was found that for higher applied potential and longer deposition time, the film showed crack-morphology with intense aggregation of particles on the background film. However, Ga-O samples deposited at relatively lower potential (-1.0 V) exhibited crack-free surface characteristics and good surface coverage. Moreover, the O/Ga ratios for the as-prepared samples were very close to 2.0, which signified GaOOH formation. Annealing in air at 500-600^{o}C reduced the O/Ga to about 1.75. This result suggested the decomposition of GaOOH to Ga_2O_3. The surface morphology did not change after thermal treatment. Furthermore, the Ga-O thin films were found to be transparent in the visible wavelength region. However, the optical absorption characteristics of the substrate used in this study forbids the estimation of the band gap. These findings can also be utilized to electrodeposit other oxides semiconductor using H_2O_2 at room temperature.

Fabrication of Ga-O based heterostructures was made possible by employing step-by-step electrodeposition technique. SnS/Ga-O superstrate heterojunction showed some rectification with annealed Ga-O layer; but photovoltaic properties were not achieved by this configuration. The origin of too large photocurrent measured in this heterostructure is not known. Probably, the junction formed between SnS and Ga-O is poor. On the contrary, by utilizing Cu_2O as absorber layer instead of SnS, rectification and photovoltaic properties were obtained for Cu_2O/Ga-O heterostructures with as-deposited and annealed Ga-O layer. Estimated V_{OC}, J_{SC} and η are (0.15, 0.35, 1.3 x 10^{-2}) and (0.22 V, 0.46 mA/cm^2, 2.5 x 10^{-2} %), respectively. The results suggest that better junction is formed between Cu_2O and Ga-O. However, further studies are still necessary to improve the photovoltaic characteristics obtained for Cu_2O/Ga-O heterojunction solar cells.

References

[1] H. H. Tippins: Phys. Rev. **140** (1965) A316.

[2] M. Ogita, H. Ohta, M. Hirano, and H. Hosono: Appl. Phys. Lett. **77** (2000) 4166.

[3] M. Rebein, W. Henrion, M. Hong, J. P. Mannaerts, and M. Fleischer: Appl. Phys. Lett. **81** (2002) 250.

[4] M. Passlack, E. F. Schubert, W. S. Hobson, M. Hong, N. Moriya, S. N. G. Chu, K. Konstadindis, J. P. Mannaerts, M. L. Schones, and GJ. Zydzik: J. Appl. Phys. **77** (1995) 686.

[5] G. Sinha, K. Adhikary, and S. Chaudhuri: J. Cryst. Growth **276** (2005) 204.

[6] Y. Ohya, J. Okano, Y. Kasuya, and T. Ban: J. Ceram. Soc. Jpn. **117** (9) (2009) 973.

[7] M. Ristic, S. Popovic, and S. Music: Mater. Lett. **59** (2005) 1227.

[8] Z. Ji, J. Du, J. Fan, and W. Wang: Opt. Mater. **28** (2006) 415.

[9] T. Oshima, T. Okuno, and S. Fujita: Jpn. J. Appl. Phys. **46** (2007) 7217.

[10] A. Petitmangin, C. Hébert, J. Perrière, B. Gallas, L. Binet, P. Barboux, and P. Vermaut: J. Appl. Phys. **109** (2011) 013711.

[11] G. X. Liu, F. K. Shan, J. J. Park, W. J. Lee, G. H. Lee, I. S. Kim, B. C. Shin, and S. G. Yoon: J. Electroceram. **17** (2006) 145.

[12] G. A. Battiston, R. Gerbasi, M. Porchia, R. Bertoncello, and F. Caccavale: Thin Solid Films **279** (1996) 115.

[13] X. Liu, G. Qiu, Y. Zhao, N. Zhang, and R. Yi: J. Alloys Comp. **439** (2007) 275.

[14] H. W. Kim and S. H. Shim: Thin Solid Films **515** (2007) 5158.

[15] X. Xiang, C.B. Cao, Y. J. Guo, and H. S. Zhu: Chem. Phys. Lett. **378** (2003) 660.

[16] U. M. Graham, S. Sharma, M. K. Sunkara, and B. H. Davis: Adv. Funct. Mater. **13** (2003) 576.

[17] G. S. Park, W. B. Choi, J. M. Kim, Y. C. Choi, Y. H. Lee, and C. B. Lim: J. Cryst. Growth **220** (2000) 494.

[18] J. C. Hulteen and C. R. Martin: J. Mater. Chem. **7** (1997) 1075.

[19] B. Hu and J. Shi: J. Mater. Chem. **13** (2003) 1250.

[20] M. Sun, D. Li, W. Zhang, X. Fu, Y. Shao, W. Li, G. Xiao, and Y. He: Nanotechnology **21** (2010) 355601.

[21] D. C. Hall, H. Wu, L. Kou, Y. Luo, R. J. Epstein, O. Blum, and H. Hou: Appl. Phys. Lett. **75** (1999) 1110.

[22] L. H. Peng, C. H. Liao, Y. C. Hsu, C. S. Jong, C. N. Huang, J. K. Ho, C. C. Chiu, and C. Y. Chen: Appl. Phys. Lett. **76** (2000) 511.

[23] S. Fujihara, Y. Shibata, and E. Hosono: J. Electrochem. Soc. **152**(11) (2005) C764.

[24] H.S. Qian, P. Gunawan, Y. X. Zhang, G. F. Lin, J. W. Zheng, and R. Xu: Cryst. Growth Des. **8** (4) (2008) 1282.

[25] H. K. Lee, D. H. Joo, M. S. Kim, and J. S. Yu: Nanoscale Res. Lett. **7** (2012) 458.

[26] S. Chowdhury and M. Ichimura: Jpn. J. Appl. Phys. **48** (2009) 061101.

[27] S. Chowdhury and M. Ichimura: Jpn. J. Appl. Phys. **49** (2010) 062302.

[28] M. Ichimura, K. Takeuchi, Y. Ono, and E. Arai: Thin Solid Films **361-362** (2000) 98.

[29] E. Fatas, P. Herrasti, F. Arjona, and E. Garcia-Camarero: J. Electrochem. Soc. **131** (1984) 2243.

[30] B. W. Sanders and A. H. Kitai: J. Cryst. Growth **100** (1990) 405.

[31] F. Goto, M. Ichimura, and E. Arai: Jpn. J. Appl. Phys. **36** (1997) L1146.

[32] D. Ramírez, D. Silva, H. Gómez, G. Riveros, R. E. Marotti, and E. A. Dalchiele: Sol. Energy Mater. Sol. Cells **91** (2007) 1458.

[33] T. Pauporté and D. Lincot: J. Electroanal. Chem. **517** (2001) 54.

[34] X. Han, R. Liu, W. Chen and Z. Xu: Thin Solid Films **516** (2008) 4025.

[35] N. Uekawa, N. Mochizuki, J. Kajiwara, F. Mori, Y. J. Wu, and K. Kakegawa: Phys. Chem. Chem. Phys. **5** (2003) 929.

[36] T. Sato and T. Nakamura: Thermochim. Acta **53** (1982) 281.

[37] C. R. Patra, Y. Mastai and A. Gedanken: J. Nanopart. Res. **6** (2004) 509.

[38] Y. Zhao, R. L. Frost, J. Yang, and W. N. Martens: J. Phys. Chem. C **112** (2008) 3568.

[39] A. Naglaa Fathy: *Electrochemical Deposition and Characterization of ZnS, ZnO,* $ZnO_{1-x}S_x$*, and SnS Thin Films for Photovoltaic Applications*, **Ph.D. Thesis** (2006) & references therein.

[40] M. Ichimura and Y. Song: Jpn. J. Appl. Phys. **50** (2011) 051002.

[41] Y. Song and M. Ichimura: Jpn. J. Appl. Phys. **51** (2012) 10NC39.

CHAPTER 7

Electrodeposition and Characterization of Fe-O Thin Films from Oxygen-Bubbled Aqueous Solutions

7.1 Introduction

Micro- and nano-structured iron oxides/oxyhydroxides have been regarded as attractive semiconductor materials in many scientific and technological applications. They are suitable for photoelectrochemical solar cells, catalyst/photocatalyst, sensors, electrodes in Li ion batteries and supercapacitors due to their abundance at or near the Earth's surface, environmental compatibility, suitable band gaps and high specific surface area [1-4]. Additionally, iron oxyhydroxides can also be used as adsorbent materials for environmental concerns. For instance, they are potential materials for the removal of toxic ions such as Cr (VI) and As (V) in contaminated drinking water and other polluted aqueous solutions [5-6]. Among the most common iron oxides/oxyhydroxides polymorphs: hematite (α-Fe_2O_3), maghemite (γ-Fe_2O_3), magnetite (Fe_3O_4), goethite (α-FeOOH), akaganeite (β-FeOOH) and lepidocrocite (γ-FeOOH); α-Fe_2O_3 is the most popular because it is thermodynamically and chemically stable over a broad pH range [7-10] and it can sufficiently utilize ~40% of the visible light spectrum [11]. Numerous reports have been devoted to the semiconductor properties and potential applications of α-Fe_2O_3.

Interestingly, iron oxide hydroxides can be utilized as starting precursors to produce iron oxides by thermal treatment depending on the annealing conditions. For instance, Naono and Nakai reported the thermal decomposition of γ-FeOOH particles to γ-Fe_2O_3 at 200^{o}C and to a more stable phase, α-Fe_2O_3 at 400^{o}C [12]. In addition, Music et al. studied and reported the decomposition of β-FeOOH particles to α-Fe_2O_3 at temperature range of 300-600^{o}C [13]. These reports suggest that iron oxide hydroxides are essential materials to produce the most stable iron oxide phase, α-Fe_2O_3.

Several studies have been devoted to the synthesis, growth, and deposition of γ-FeOOH by spray [14], hydrolysis of Fe ions [15-16], chemical oxidation of Fe(II) ions or Fe(II) complexes [17-26], and electrodeposition techniques [27-32]. Carpenter et al. reported amorphous γ-FeOOH on polyimide film deposited by spray method [14]. Nagtegaal et al. reported deposition of FeOOH film from iron nitrate solution by hydrolysis at room temperature [15]. Moreover, γ-FeOOH can be prepared via the chemical oxidation of green rusts as intermediate products. Commercially available green rust powders can also be used as starting precursors to produce γ-FeOOH by direct chemical oxidation, though the product is usually a mixture of α-, β- and γ-FeOOH and Fe_3O_4 phases. Schneider et al. and J. Majzlan et al. reported the synthesis of γ-FeOOH thin film by chemical oxidation of synthesized green rust thin film [17-18]. Nakanishi et al. prepared and deposited γ-FeOOH on Pd-catalyzed substrates facilitated by electroreduction of nitrate ions in the solution [27]. FeOOH can be electrodeposited from acidic solution (pH = 2.9) via reduction of H_2O_2; as a result, OH^- ions are generated in the process [30]. However, the solution should contain complexing agent (F^-) to increase the solubility of Fe^{3+}. Other efforts have been performed in either slightly higher pH (6.0–8.0) or in acidic solution (pH = 4.1) by anodic oxidation of ferrous ions. At higher pH, complexing agents such as NH_4^+ are often included to increase the solubility of Fe^{2+} [31-32].

So far, the semiconductor properties of γ-FeOOH have not been reported and investigated yet. Hence, this work focuses on electrodeposition of γ-FeOOH thin films from oxygen-bubbled aqueous solution of Fe^{2+} ions at room temperature. Different deposition parameters such as type of supporting electrolytes, stirring rate, applied potentials, and deposition time are considered in electrodepositing the films in acidic solution. The as-prepared γ-FeOOH thin films are then characterized to study and investigate their semiconductor properties such as conductivity type, photoresponse, optical transmission, and band gap. Thermal annealing in air is also considered to investigate its effect on the composition and quality of the films.

Moreover, the fabrication of Fe-O based heterojunctions by employing step-by-step electrodeposition of the *n-type* window (as-deposited and annealed Fe-O) and *p-type* absorber (SnS and Cu_2O) layers are also presented to discuss the possible heterojunction solar cell application of the electrodeposited Fe-O thin films.

7.2 Experimental Details

7.2.1 Electrodeposition and characterization of Fe-O thin films

Fe-O thin films were electrodeposited on indium tin oxide (ITO)-coated glass substrate using the typical three-electrode electrochemical cell with ITO, platinum (Pt) sheet, and saturated calomel electrode (SCE) as working, counter, and reference electrodes, respectively. An aqueous solution containing 0.05 M $FeSO_4.7H_2O$ and 0.1 M KCl was prepared to electrodeposit the Fe-O thin films. Sodium sulfate (Na_2SO_4) as supporting electrolyte was also used to investigate its effect on the deposition of the films. In this solution condition, KCl was replaced by Na_2SO_4 with equal concentration. The as-prepared solutions were then saturated with oxygen by bubbling before the start of electrodeposition. Additionally, an investigation for hydrogen peroxide (H_2O_2) instead of dissolved oxygen as oxygen precursor was also performed at room temperature; but it turned out that by adding just one drop of aqueous H_2O_2 in $FeSO_4$-KCl (or $FeSO_4$-Na_2SO_4) solution, the appearance of the solution changed from colorless to transparent reddish-brown, which indicates oxidation of Fe^{2+} to Fe^{3+} (H_2O_2 as oxidizing agent). However, after few minutes, brown-colored precipitates appeared in the solution. These precipitates could be the highly insoluble iron (III) hydroxides, $Fe(OH)_3$. Thus, deposition using H_2O_2 as oxygen precursor was not performed further at the present.

All depositions were carried out at room temperature and in either quiescent or non-quiescent solution. For non-quiescent condition, the solution was stirred during deposition at different stirring rates (150, 300, and 600 rpm) using a magnetic stirrer to study its effect on the quality of the films. Thermal annealing in air for 1 hour was also carried to investigate its effect on the physical, compositional, and morphological properties of the films.

As a usual procedure prior to electrodeposition, ITO substrate was ultrasonically cleaned in alkyl benzene, subsequently rinsed in pure water, and finally dried by nitrogen purging. Similarly, Pt counter electrode was ultrasonically cleaned in deionized water and then dried in nitrogen gas. Cyclic voltammetry (CV) was carried out to determine the suitable potentials for the deposition of the film. All deposition potential values were referenced to SCE.

Compositional analysis and surface morphology studies were performed using a JEOL JAMP-9500F field-emission Auger microprobe at a probe voltage of 10 kV and a current of 1.0 x 10^{-8} A. Argon ion etching was done using an acceleration voltage of 2 kV with ion current of 2.6 μA to sputter the film's surface. Auger electron spectroscopy (AES) spectra were recorded and analyzed at the surface and after sputtering the surface with a rate of 10 nm/min. The composition ratio (Fe/O) was calculated using the standard Fe_2O_3 compound (with Fe/O ~ 0.67). Additionally, Raman spectroscopy was done by utilizing JASCO NRS-3300 laser Raman spectrophotometer for further analysis of the composition of the as-deposited samples. A red laser with 632.83 nm wavelength was used in Raman spectroscopy. The crystalline structure of the sample was characterized by X-ray diffraction, which was carried out using a SmartLab X-ray Diffractometer. The thickness of the films was measured using an Accretech Surfcom-1400D profilometer. A JASCO U-570 ultraviolet/visible/near infrared (UV/vis/NIR) spectrometer was used for optical transmission studies from 300 – 1000 nm wavelengths with the substrate as the reference.

7.2.2 Fabrication of SnS/Fe-O and Cu_2O/Fe-O heterojunction solar cells

The as-prepared Fe-O thin films were then utilized as window layers and partnered with potentiostatically-electrodeposited SnS and galvanostatically-electrodeposited Cu_2O to fabricate SnS/Fe-O and Cu_2O/Fe-O heterojunctions. All the heterostructures (SnS/Fe-O and Cu_2O/Fe-O) are fabricated with the same heterojunction configurations (superstrate structures), that is, a light with intensity of 100 mW/cm^2 was illuminated from the source and transmitted from the substrate side towards the *n-type* layer (Fe-O) and then reached the absorber *p-type* layer.

For SnS/Fe-O heterojunction structure, SnS was deposited via the three-step pulsed electrodeposition onto the Fe-O layer. The deposition potentials are $V_1 = -1.0$ V, $V_2 = -0.6$ V and $V_3 = 0$ V at equal pulse time $t_1 = t_2 = t_3 = 10$ s for 10 min. The working solution contained 10 mM $SnSO_4$, 50 mM $Na_2S_2O_3$ and 5 or 20 mM $FeSO_4.7H_2O$. It has been observed that no good SnS layer deposition attained on as-prepared Fe-O using the usual solution condition (mixture of $SnSO_4$ and $Na_2S_2O_3$ only) to electrodeposit SnS layer. This observation is thought to be due to the possible dissolution of Fe-O film in acidic aqueous solution. Dissolution can be regarded as the more dominant process than SnS deposition. Hence, negating this effect is necessary to provide relatively good SnS thin film deposition on the Fe-O layer. One possible technique is by buffering the solution with a precursor that supplies the appropriate ions for suppression of FeOOH dissolution. This technique has been employed by Musselman et al. to fabricate ZnO/Cu_2O heterojunctions via electrodeposition method [33]. In their work, ZnO powder is used and added in the solution as the buffering precursor prior to Cu_2O deposition. It turns out that ZnO powder supplies the suitable ions to effectively negate the dissolution effect on ZnO during Cu_2O layer deposition.

For Cu_2O/Fe-O heterostructures, as-prepared and annealed Fe-O thin films are used as window layers. The *p-type* Cu_2O absorber layer is then deposited on Fe-O by employing galvanostatic electrodeposition. The deposition condition for Cu_2O is adopted from the work of Ichimura and Song [34-35]. Briefly, the Cu_2O deposition solution contained 0.2 M $CuSO_4$, 1.6 M lactic acid and the pH was adjusted to 12.5 by adding suitable amount of KOH in the solution. Deposition was carried out in slightly elevated temperature of 40 ^oC and in a quiescent solution. A constant current density (-1.0 mA/cm^2) was applied to electrodeposit Cu_2O on Fe-O layer. The thickness of the FeOOH layer was varied to investigate its effect on the photovoltaic performance of the fabricated Cu_2O/Fe-O heterostructures. Indium (In) electrodes are then evaporated on ITO and on the top of Cu_2O layer to provide electrical contacts during current-voltage (J-V) characterizations.

7.3 Results and Discussion

7.3.1 Cyclic voltammetry and thin film formation

Figure 7.1 shows the CV curves obtained from the aqueous solutions (a) without and (b) with oxygen bubbling. The solution contained 0.05 M $FeSO_4.7H_2O$ + 0.1 M KCl. In curve (a), during cathodic scan, no reduction peak was observed. A sharp increase in reduction current started at around -0.94 V. This current can be associated to the plating of Fe metal onto the substrate at a large overpotential due to the reduction of Fe^{2+} to Fe. This onset potential for Fe plating agrees very well to the value (-0.947 V vs SCE) obtained by Brogan from $FeSO_4$ aqueous solution [36]. It has been reported that from thermodynamic calculations the onset of the reduction Fe^{2+} to produce Fe should begin at around -0.772 (V vs SCE) [37]. The possible reason for the deviation of the values could be due to the slow rate of reaction at less reductive potential. Indeed, Fe deposition is expected to happen during cathodic voltage scan from a non-oxygen-bubbled solution. In the anodic scan, a well-defined anodic peak at -0.5 V is observed. This can be considered as the oxidation of the deposited Fe attained during cathodic reaction.

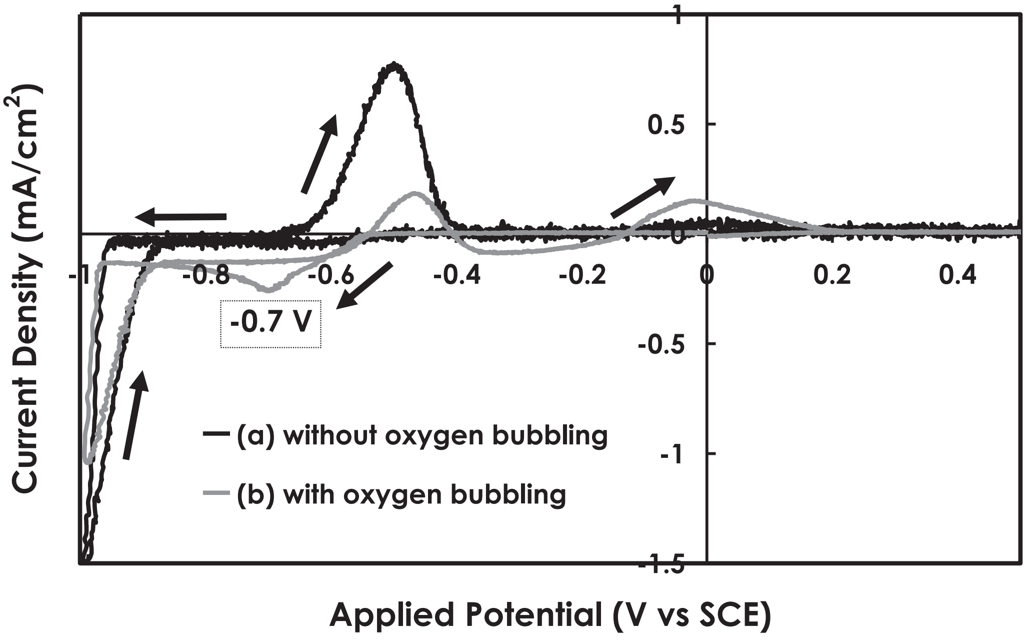

Fig. 7.1 CV curves obtained from 0.05 M $FeSO_4.7H_2O$ + 0.1 M KCl aqueous solution (a) without and (b) with oxygen bubbling. The voltage scan rate is 5 mVs^{-1}. The directions of the arrows correspond to cathodic (to the left or down) and anodic (up) scans.

On the other hand, by employing oxygen bubbling as shown in curve (b), the reduction current started to be visible at -0.55 V and a discernable reduction peak at around -0.70 V was attained. This could imply that dissolved oxygen promotes the cathodic reaction associated to the film formation onto the ITO substrate. In the reverse potential scan, two distinct peaks were observed: at -0.46 and -0.02 V. The peak at -0.46 V is similar to the anodic reaction observed in no oxygen bubbling case, while the broad peak at -0.02 V can be considered as oxidation of the other species present during electrodeposition.

The formation of the iron compound thin films from oxygen-bubbled aqueous iron sulfate solution at room temperature can be described as electrochemical reaction involving the starting precursors: Fe^{2+}, dissolved oxygen and water forming iron oxide hydroxide (FeOOH) as the final product. The overall reaction mechanism can be represented by,

$$4Fe^{2+} + 3O_2 + 2H_2O + 8e^- \rightarrow 4FeOOH \qquad (7.1)$$

This electrochemical reaction will result to the deposition FeOOH film onto the substrate. Without oxygen bubbling, the deposition current is very small, that is, very thin film is attained even after 20 min of deposition. Hence, all samples used for characterization are electrodeposited from the oxygen-bubbled solutions.

In addition, subsidiary reactions (chemical reactions) other than reaction (7.1) above could also occur during the deposition process. These reactions may involve generation of H^+, which in effect reduces the solution's pH. The change in pH value was monitored with a pH meter. It was observed that the pH slightly reduced from 4.60 to 4.40 after 10 min bubbling. By visual observation, the solution remained clear and precipitation was not seen during the entire bubbling process. When the bubbling time is extended to 60 min, the solution appearance changed to pale yellow and the pH further reduced to 4.06. These observations may signify oxidation of some Fe^{2+} ions under aerobic condition. Generally, a change in color (from colorless to yellowish appearance) can be expected if the amount of oxidized species in the starting solution is larger than that of the remaining un-oxidized Fe^{2+} ions. At room temperature, this effect is considered very slow compared to the change at higher temperature condition. To verify this, a separate experiment is performed at slightly elevated temperature of 40 ^{o}C. After 10 min oxygen bubbling, a yellowish solution was obtained. The pH of this oxygen-bubbled solution reduced to 4.11. This implies that at higher temperature, the oxidation of Fe^{2+} happens at a relatively faster rate. In addition, extending the bubbling duration also decreased the pH significantly with the formation of yellowish precipitates or colloidal particles.

Moreover, the solution's pH further reduced to 3.88 after 20 min deposition. By visual observation, the solution after deposition contained yellow colloidal particles or precipitates. This observation is probably due to the reaction of Fe^{2+} with dissolved oxygen and water forming iron oxide hydroxides as precipitates. The reaction can be described and represented by

$$2Fe^{2+} + \frac{1}{2}O_2 + 3H_2O \rightarrow 2FeOOH + 4H^+ . \qquad (7.2)$$

Reaction (7.2) is similar to the reported precipitation reaction for γ-FeOOH produced by hydration and oxidation of Fe^{2+} ions accompanied by proton generation [38].

7.3.2 Surface morphology studies

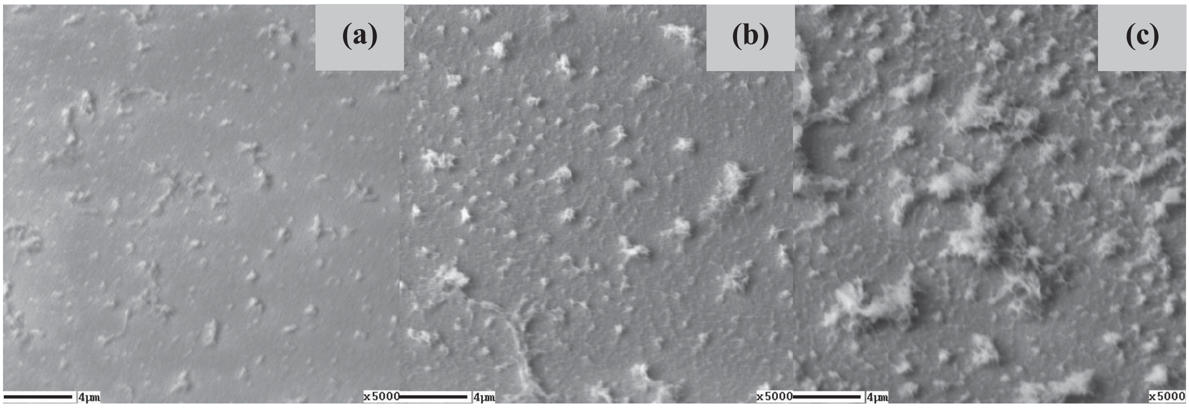

Fig. 7.2 SEM images of as-prepared Fe-O thin films deposited at -0.9 V for (a) 2, (b) 5, and (c) 10 min.

Figures 7.2 shows the surface morphologies of the as-prepared thin films deposited at -0.90 V at different deposition times (2 – 10 min). As seen in Fig. 7.2 (a), deposition at -0.9 V for 2 min, the surface seems flat with minimal aggregation. As deposition time is extended up to 20 min as depicted in Fig. 7.3 (a), flake like morphologies become apparent and somewhat disperse over the entire area. Additionally, the aggregation becomes more intense and non-uniformity in the surface is very evident. This can contribute to a significant roughness of the films. This flake like type morphology of γ-FeOOH was reported by Jia et. al on the synthesis of γ-FeOOH nanoflakes by using simple ethylene glycol (EG)-mediated solution method [6]. By comparing the surface images of the samples deposited at other potentials (-0.8 and -0.7 V) as shown in Figs. 7.3 (b) and (c), the surfaces seem to have similar dispersed flake like morphologies. In addition to that, non-uniformity in the surface is clearly observed. Extending the deposition potential at more negative values; for instance, at -1.1 and -1.3 V, the films exhibit a mixture of FeOOH and Fe metal. As displayed in the surface images in Figs. 7.3 (d) and (e), the surfaces exhibit additional cubic and a mixture of dominantly cubic-dendritic morphologies at -1.1 and -1.3 V, respectively. These types of morphology are characteristics of Fe metal constituents in the film.

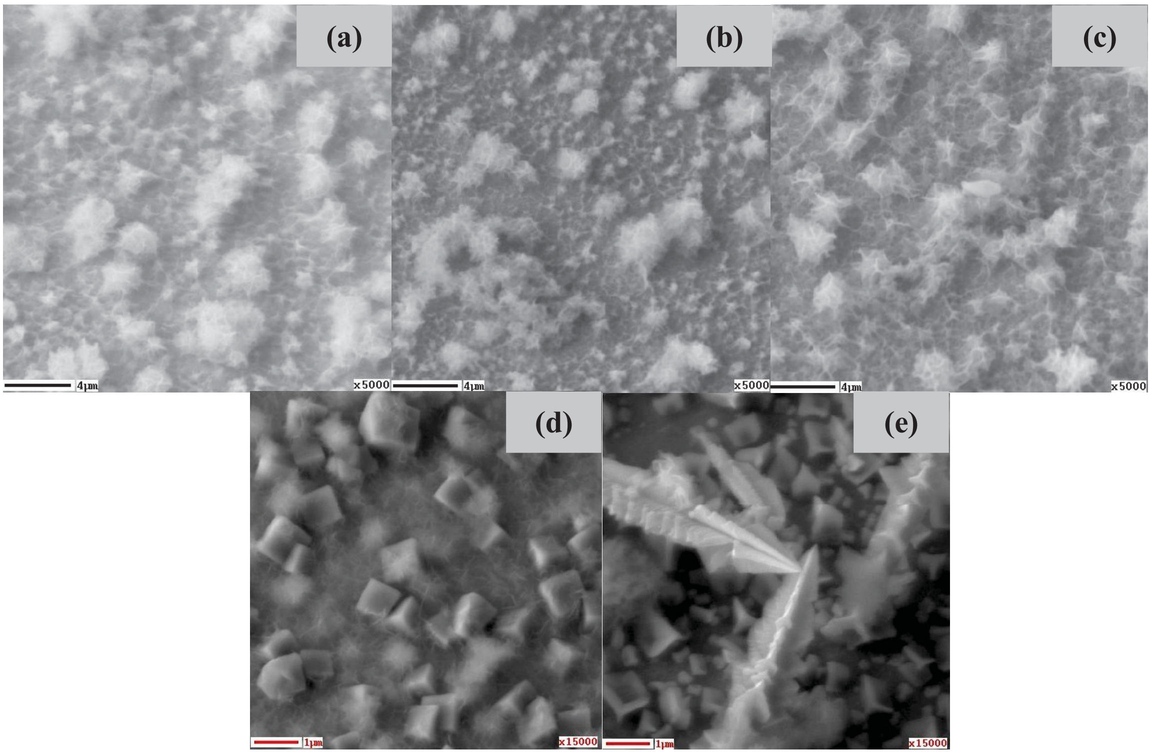

Fig. 7.3 SEM images of as-prepared Fe-O thin films deposited at (a) -0.9, (b) -0.8 and (c) -0.7 V for 20 min. Surface images of the films deposited at (d) -1.1 and (e) -1.3 V prepared for 2 min (magnification: 15,000).

7.3.3 XRD, Auger, and Raman spectroscopic analyses

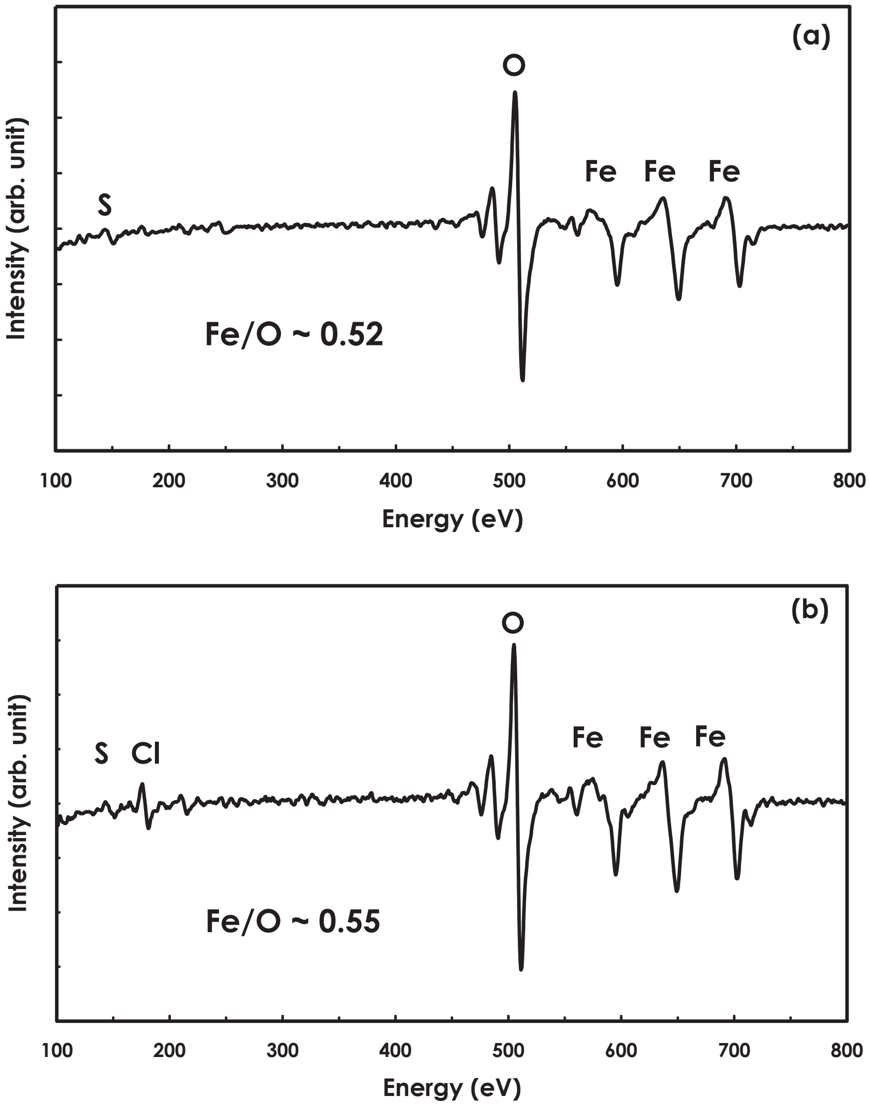

Fig. 7.4 Auger spectra for sputtered surface of as-prepared thin film deposited at -0.9 V for (a) 20 and (b) 5 min.

Auger spectroscopic analysis was carried out to determine the composition of the films at the surface as well as at the inner portion of the film. Figure 7.4 shows the AES spectra of the as-prepared films deposited at -0.9 V after 30 s of Argon ion sputtering. It should be noted that the sputtering is usually done to remove contaminations like carbon impurities, which are ubiquitously present at the film's surface. As seen in these spectra, Fe and O peaks are clearly observed with Fe/O ratio ranges from 0.52 - 0.55, which is estimated using the standard Fe_2O_3. These results support the formation of non-stoichiometric FeOOH film onto the substrate as described in reaction (7.1).

It is noticeable that small sulfur (S) peak could appear in the spectrum even after sputtering. Additionally, chlorine (Cl) peak is evidently visible in the spectrum especially for samples deposited at shorter times as depicted in Fig. 7.4 (b). The origin of these sulfur and chlorine impurities could be due to some sulfate (SO_4^{-2}) and Cl^- ions that are being incorporated during the formation of the FeOOH film. To verify this possibility, Raman spectroscopic analysis is performed for further analysis of the chemical bonding between Fe and O constituents.

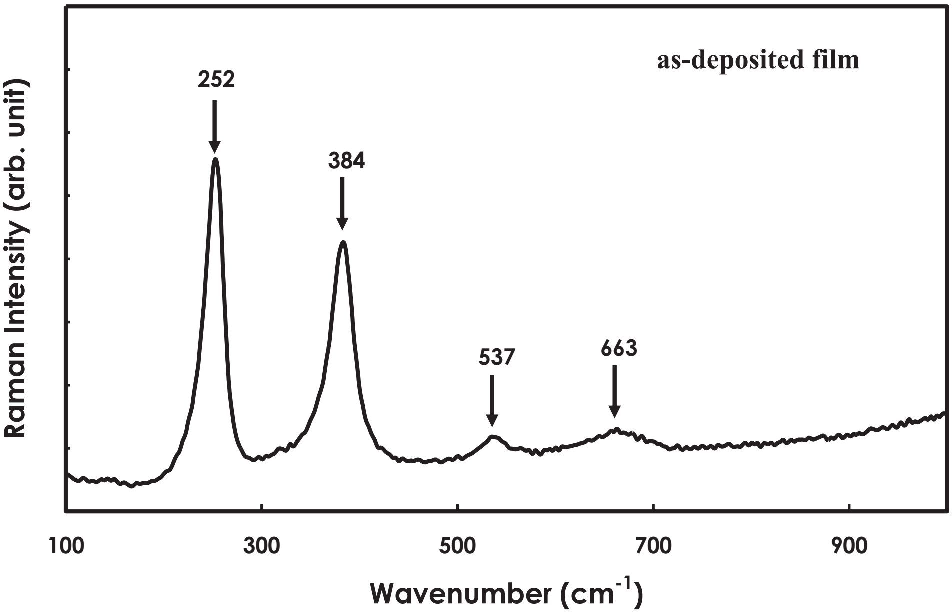

Fig. 7.5 Corresponding Raman shift for the as-prepared thin film deposited at -0.9 V.

Figure 7.5 depicts the Raman shift for the as-prepared film deposited at -0.9 V for 20 min. Two sharp peaks (252 and 384 cm^{-1}) and two broad peaks (537 and 663 cm^{-1}) are observed. These observed peaks are the characteristic Raman shifts of γ-FeOOH [39-44]. These results further confirm the formation of FeOOH onto the substrate. However, the presence of S impurities due to sulfate ions as detected in AES measurement can be considered small since no peak associated to sulfate band (which is prominently located near 1000 cm^{-1}) [45] is displayed in Raman result. It is important to note that the inclusion of SO_4^{2-} and Cl^- ions in FeOOH has been reported to be possible. For instance, previous studies have concluded that β-FeOOH material contains chloride ions [46-48].

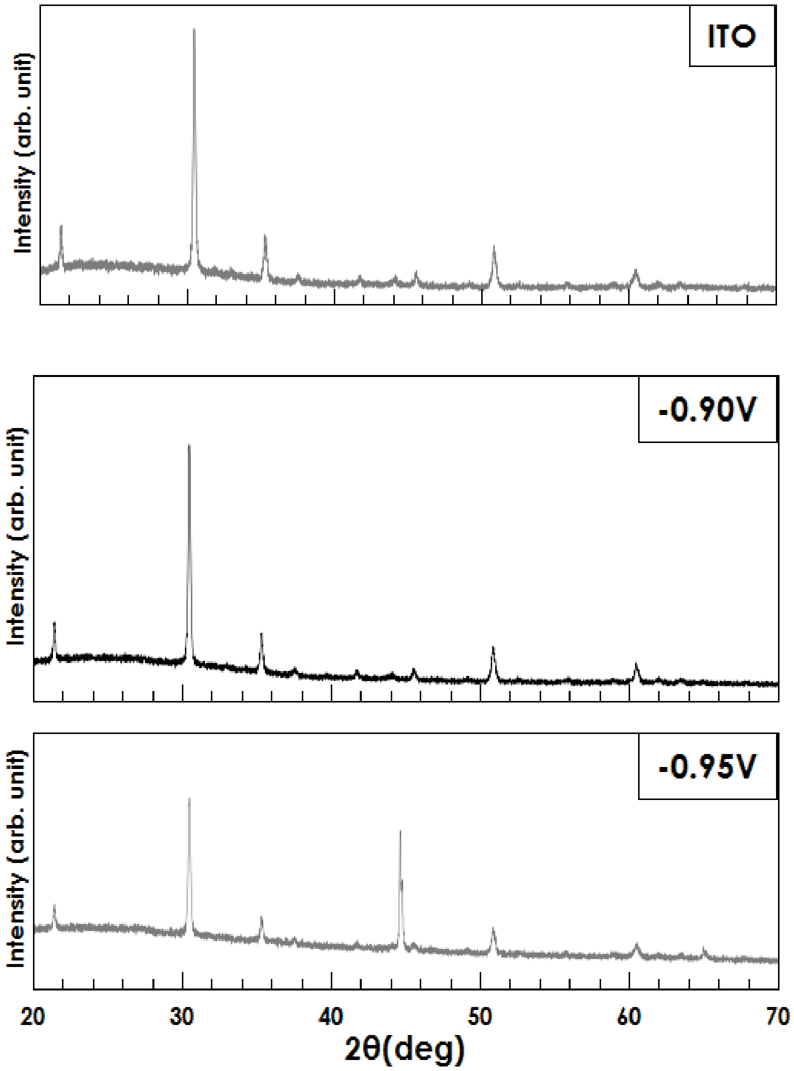

Fig. 7.6 XRD patterns for the ITO substrate and the as-prepared thin films deposited at different potentials: -0.90 and -0.95 V for 20 min.

Figure 7.6 shows the XRD patterns of as-prepared thin films deposited at -0.90 and -0.95 V. The pattern of ITO substrate is also shown for comparison. It is observed that no perceivable XRD peaks associated to γ-FeOOH for the film deposited at -0.90 V. This suggests that the electrodeposited γ-FeOOH thin film consists of very fine grains (nanocrystalline structure), i.e., the film does not have a long-range order sufficient for XRD but a sufficient short-range order for Raman scattering. However, for the film deposited at -0.95 V, the prominent peak of α-Fe, (110) diffraction, is clearly observed at $2\theta = 44.66^{o}$. Additionally, the peak near $2\theta = 65^{o}$ can be associated to Fe(200) diffraction. These results imply that the plating of Fe metal onto the substrate is obtained at reduction potentials more negative than -0.90 V. As discussed in the CV results, the onset of Fe plating occurs near -0.95 V. It can be said that the film deposited at a reduction potential of -0.95 V is a mixture of FeOOH and a highly crystalline α-Fe. With this observation, the maximum reduction potential to obtain pure γ-FeOOH film without Fe impurities is at -0.90 V.

7.3. 4 Optical transmission and band gap estimation

Figure 7.7 shows the optical transmission of the γ-FeOOH films deposited at -0.9 V for 10 and 20 min. It should be noted that since the ITO substrate was used as the reference in the double-beam spectrometer measurement, the effects of the substrate absorption was basically removed. However, the transmission of the substrate in the UV range (< 350 nm) is low, and therefore the data in the wavelength range < 350 nm may be not so reliable. As depicted in the figure, no clear absorption edge is observed for the thicker sample deposited for 20 min because the optical transmission of the sample gradually decreases with wavelength; but for the thinner film, an absorption edge is apparently between 400 and 500 nm. Hence, this absorption edge can be regarded as the optical characteristic of the as-deposited γ-FeOOH film.

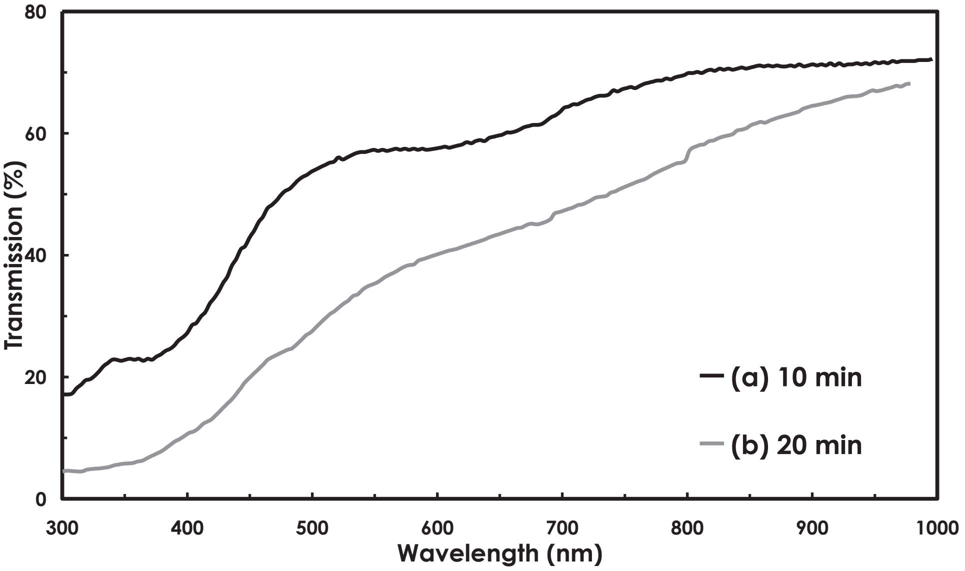

Fig. 7.7 Optical transmission for the as-prepared thin films deposited at -0.9 V for (a) 10 and (b) 20 min.

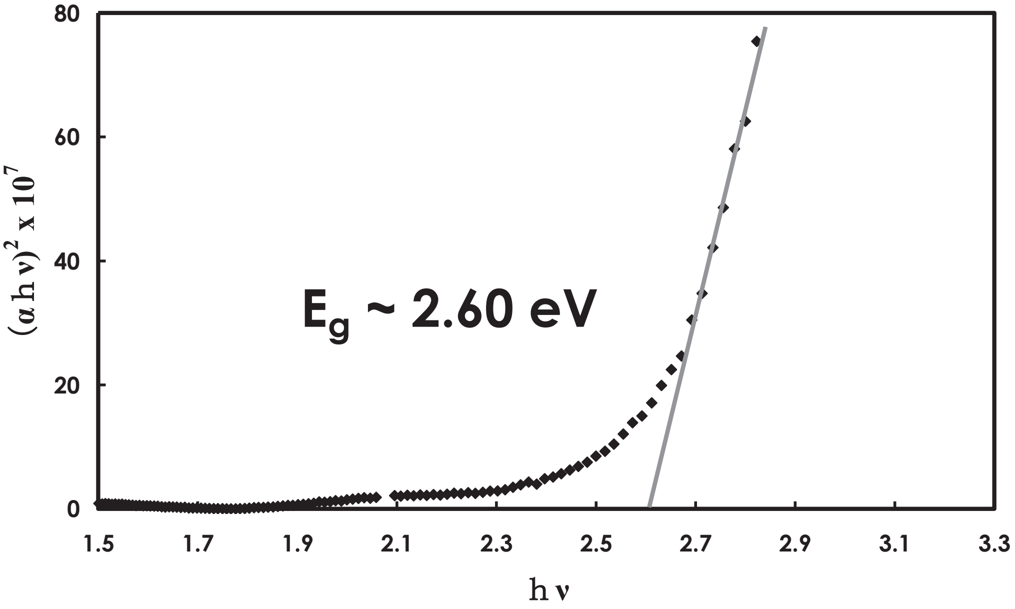

Fig. 7.8 The corresponding Tauc's plot of the transmission curve for the FeOOH sample deposited at -0.9 V for 10 min to estimate the band gap.

The optical band gap of γ-FeOOH can be experimentally determined from the plot of $(\alpha hv)^2$ versus *hv*, where *α* is the absorption coefficient near the absorption edge, *h* is the Planck's constant and *v* denotes the frequency. The linear region is extrapolated to estimate the band gap as depicted in Figure 7.8. As seen in this Tauc's plot, the band gap is estimated to be 2.6 eV. This value is slightly higher than the reported band gaps of α-Fe_2O_3, γ-Fe_2O_3 and β-FeOOH materials (2.0~2.2 eV) [49-52]. These results may suggest the potential usage of γ-FeOOH obtained via electrodeposition technique for solar cells and other device applications.

7.3.5 Photoelectrochemical measurements: conductivity type and photosensitivity determination

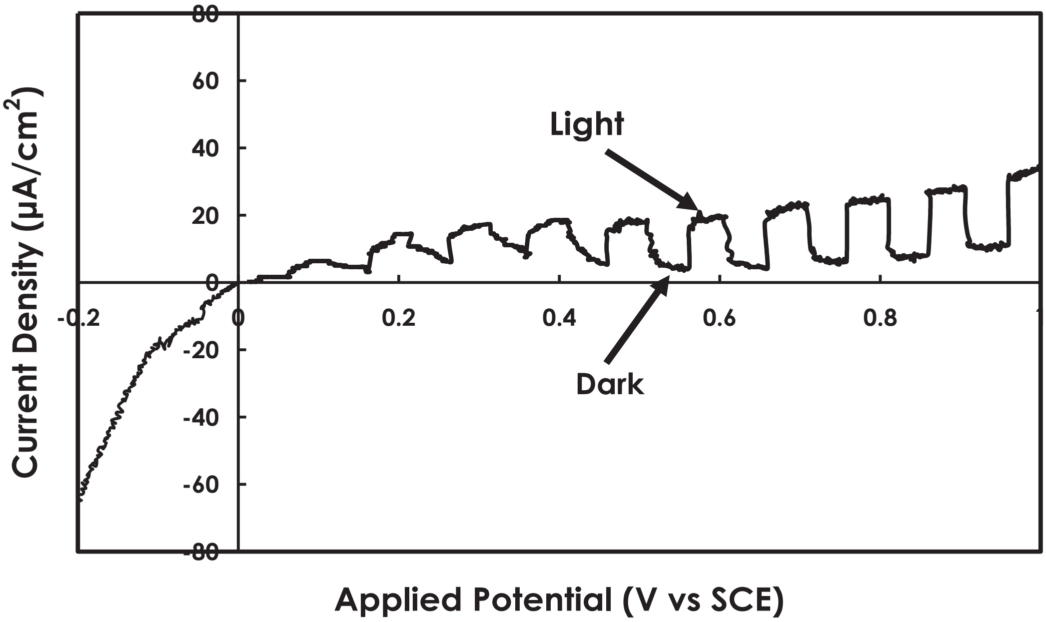

Fig. 7.9 Photoresponse characteristics of γ-FeOOH film deposited at -0.9 V for 20 min.

Photoelectrochemical (PEC) measurements using the as-deposited γ-FeOOH as the cathode electrode were carried out in aqueous solution containing 100 mM Na_2SO_4 under chopped illumination (with an intensity of 100 mW/cm^2) from the substrate side of the film to evaluate and determine the photosensitivity and also the conductivity type of the semiconductor material.

The photocurrent response is recorded or plotted against the applied potential (linearly increasing or fixed). Figure 7.9 shows the PEC response of the as-prepared γ-FeOOH under linearly increasing bias from -0.2 to +1.0 (V vs SCE). For reverse (cathodic) bias, only an increase in current is attained under dark and illumination conditions. However, the photocurrent response during forward (anodic) bias scan is clearly observed, that is, positive photocurrent increased under illumination and decreased under dark condition. Hence, generation of carriers by photo irradiation occurs in the electrodeposited γ-FeOOH. Since the observed photocurrent is positive, the photogenerated minority carriers are holes. Thus, the as-deposited γ-FeOOH exhibits n-type conductivity.

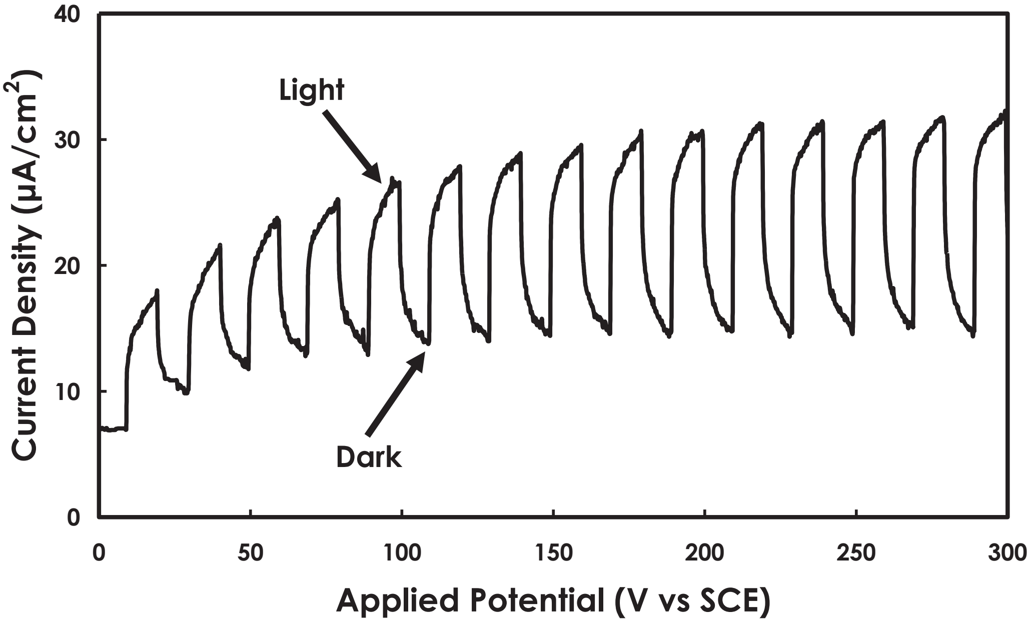

Fig. 7.10 Photoresponse for γ-FeOOH film at constant applied potential of 0.6 (V vs SCE).

Figure 7.10 shows the transient photocurrent response obtained by applying a potential of 0.6 (V vs SCE) at the scan rate of 5 mV/s. The photocurrent of the as-deposited γ-FeOOH thin film shows no sign of any degradation. This implies that the material is quite stable in Na_2SO_4 aqueous solution. Thus, this result suggests that γ-FeOOH thin films can have a potential use in water splitting applications.

7.3.6 Effect of stirring and supporting electrolytes

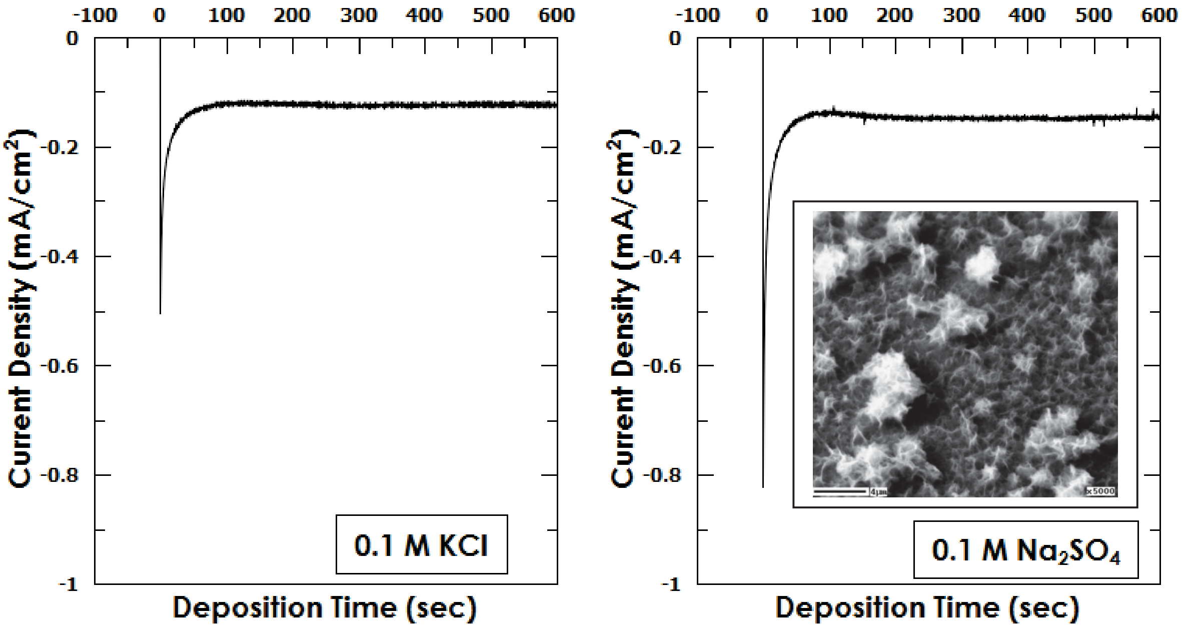

Fig. 7.11 Current density profiles obtained from deposition in aqueous solutions with either KCl or Na_2SO_4 as supporting electrolytes. Inset shows the morphology of the sample.

As discussed in the AES results presented in Section 7.3.3, Cl^- ions can be incorporated in the γ-FeOOH film. These anions can be adsorbed during film formation. It has been known that the formation of FeOOH could also depend on the nature of the anions present in the starting solution. For instance, chloride as an inert anion is preferred to produce γ-FeOOH and carbonates direct the system towards goethite (α-FeOOH) formation [53-54]. Additionally, Cl^- and SO_4^{2-} ions are useful to obtain pure γ-FeOOH via the formation of intermediate green rust products [55]. It is also possible that during the formation of FeOOH from solutions with the presence of both Cl^- and SO_4^{2-} ions, the inclusion of these anions by adsorption can be expected. Thus, for this reason, instead of KCl as supporting electrolytes, Na_2SO_4 is utilized to ensure homogeneity of the anions in the solution (SO_4^{2-} ions) since the Fe salt ($FeSO_4•7H_2O$) already has the sulfate component. This preparation surely avoids the inclusion of Cl^- ions during film formation.

Figure 7.11 shows the current density profiles for the γ-FeOOH films deposited at -0.9 V for 10 min using different supporting electrolytes added into the solution. It is observed that at the initial stage of electrodeposition, the obtained current density is higher in the solution with Na_2SO_4 compared to that attained in the solution with KCl. This could mean that the non-uniformity of the anions in the solution might affect the deposition of the film onto the substrate. As seen also in the figure, after the initial surge of deposition, a large decrease in the reduction current is observed for solution with either KCl or Na_2SO_4 as supporting electrolyte. After around 100 s, a constant reduction current is obtained. The decrease could be associated not only to the increase of the resistivity of the substrate when the film started to form but also to the decrease of the available ions near the vicinity of the substrate to participate in the formation of the film. In addition to that, as discussed in Section 7.3.1, a subsidiary reaction could happen during deposition; as a result, some yellowish precipitates were formed in the solution.

The formation of precipitates could affect the deposition of the film via electrochemical reaction. It is observed that the precipitate formation is more apparent when the duration of deposition is extended to 30-60 min. As noted also that this formation of yellow precipitates is very sluggish at room temperature condition. Hence, at shorter deposition time, γ-FeOOH film is dominantly formed due to the electrochemical reaction described by reaction (7.1). The inset in Fig. 7.11 shows the morphology of the film deposited at -0.9 V for 20 min from $FeSO_4$-Na_2SO_4 solution. This morphology and the image shown in Fig. 7.3 (a) for the film prepared from $FeSO_4$-KCl solution that is deposited at the same potential and deposition duration conditions display very similar surface morphology.

Figure 7.12 (a) depicts the transmission curve of the sample deposited from the solution using Na_2SO_4 as supporting electrolyte. It can be seen that the optical transmission of the sample deposited from the mixture of $FeSO_4$-Na_2SO_4 is slightly improve from 500-1000 nm wavelength range. It is observed that very similar morphology as shown in Fig. 7.2 (c) is attained from this solution condition. Hence, the reason for the slight improvement is not yet known. In addition to that, the absorption edge is also slightly shifted towards longer wavelength. In fact, a large decrease in transmission started at around 550 nm for the sample obtained from $FeSO_4$-Na_2SO_4

solution and ~500 nm for the sample deposited from the $FeSO_4$-KCl solution. As displayed in the Tauc's plot shown in Fig. 7.12 (b), the band gap of γ-FeOOH film is estimated to be ~2.45 eV.

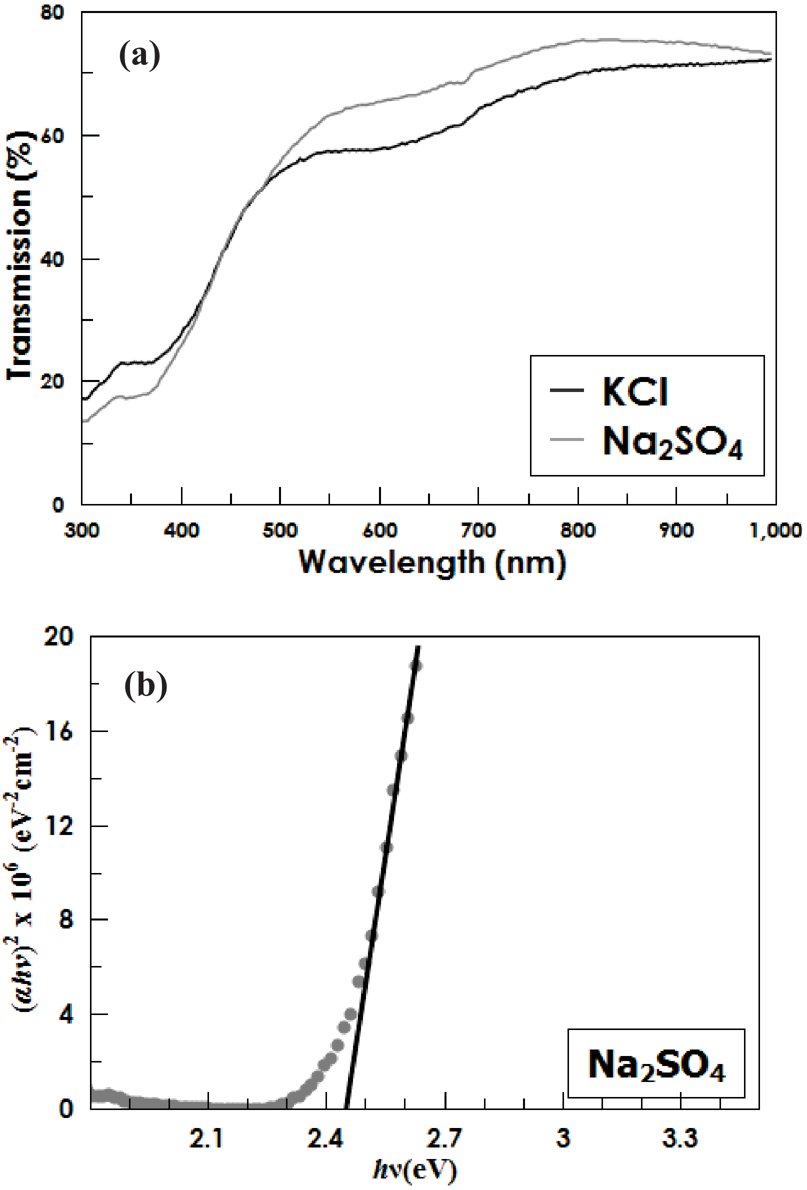

Fig. 7.12 (a) Transmission curve and (b) the corresponding Tauc's plot obtained for the sample deposited from solution with Na_2SO_4 as supporting electrolyte. The transmission curve for the sample deposited from the solution with KCl is re-plotted for comparison.

In addition to this slight improvement in the optical properties, the homogeneity of the anions in the working solution results to the disappearance of the Cl peak in the AES spectrum. Only sulfur impurity represented by the S peak is observed after 180 s of sputtering (Figure 7.13).

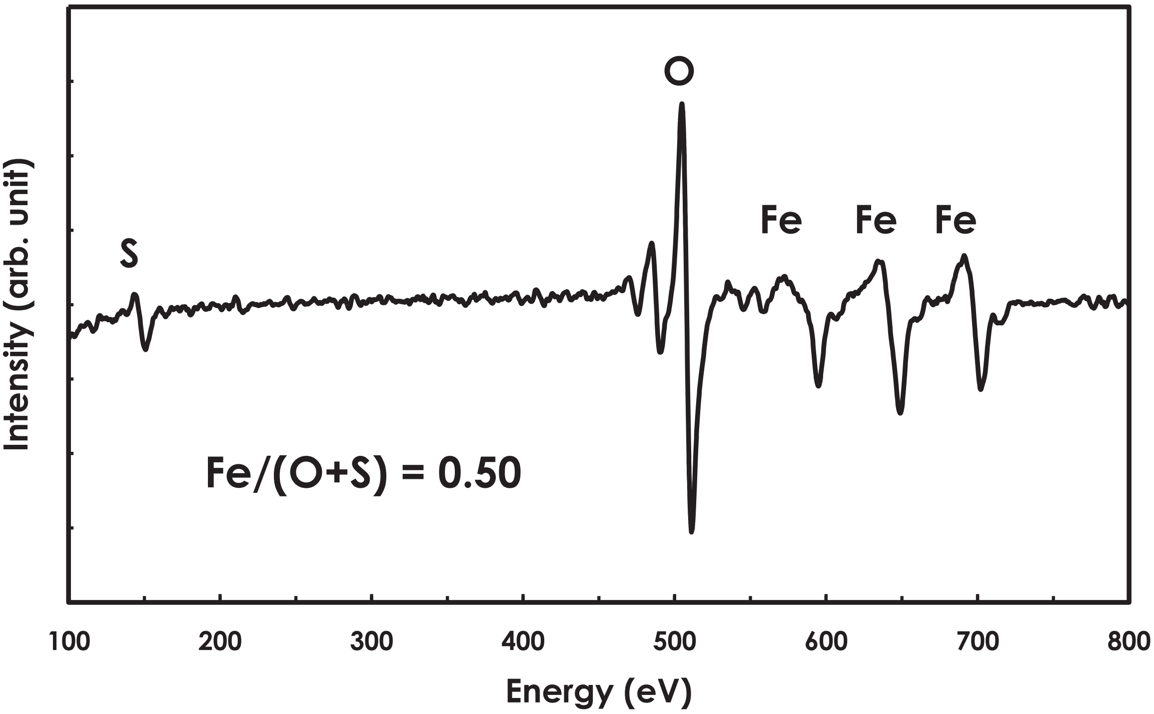

Fig. 7.13 Auger spectrum for the FeOOH sample prepared from $FeSO_4$-Na_2SO_4 solution and deposited at -0.9 V for 20 min.

The effect of stirring is also studied by employing magnetic stirrer during deposition at different stirring rates from 150 – 600 rpm. By stirring the solution during deposition, it could be assumed that a homogenous distribution of cathodic and anodic ions in the electrolyte can be achieved. The relationship of the obtained film thickness against stirring rate is plotted and shown in Figure 7.14. It is observed that for non-stirred $FeSO_4$-Na_2SO_4 solution, a thickness of 50 nm is achieved after 10 min of deposition. Almost the same film thickness is attained when deposition is carried out in stirred solution at a rate of 150 rpm. However, for much higher stirring rate (300 and 600 rpm), the obtained film thickness is 150 and 350 nm after 10 min of deposition, respectively. This implies that the thickness can be significantly increased by stirring the solution at an appropriate rate during deposition. Additionally, much thicker film (~1.0 µm) is obtained at 600 rpm compared to ~ 0.5-0.6 µm at 300 rpm after 60 min of deposition. The reason for the significant increase in the thickness obtained in stirred solution can be analyzed from the current density recorded and monitored during film formation. It is expected that a higher current density will result to a thicker film (larger thickness). By looking at the current density profiles obtained from the stirred solutions as shown in Figure 7.15, the deposition current is clearly enhanced by stirring.

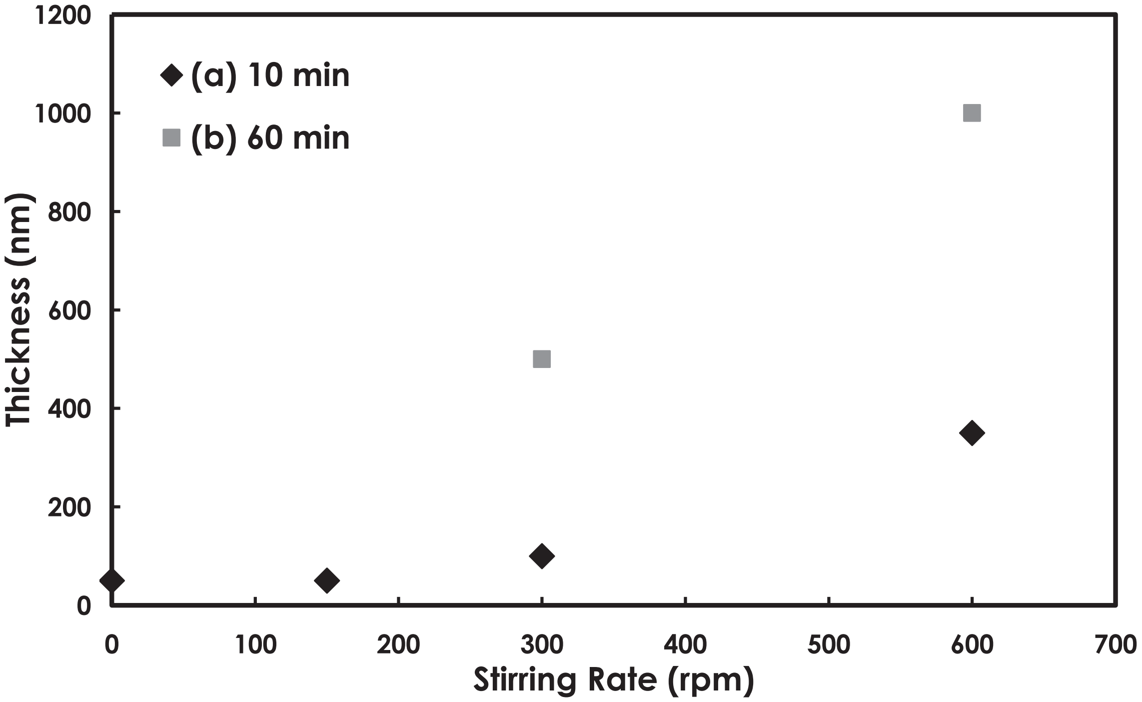

Fig. 7.14 Relationship of film thickness against stirring rate for as-prepared γ-FeOOH thin films deposited at -0.9 V for 10 min.

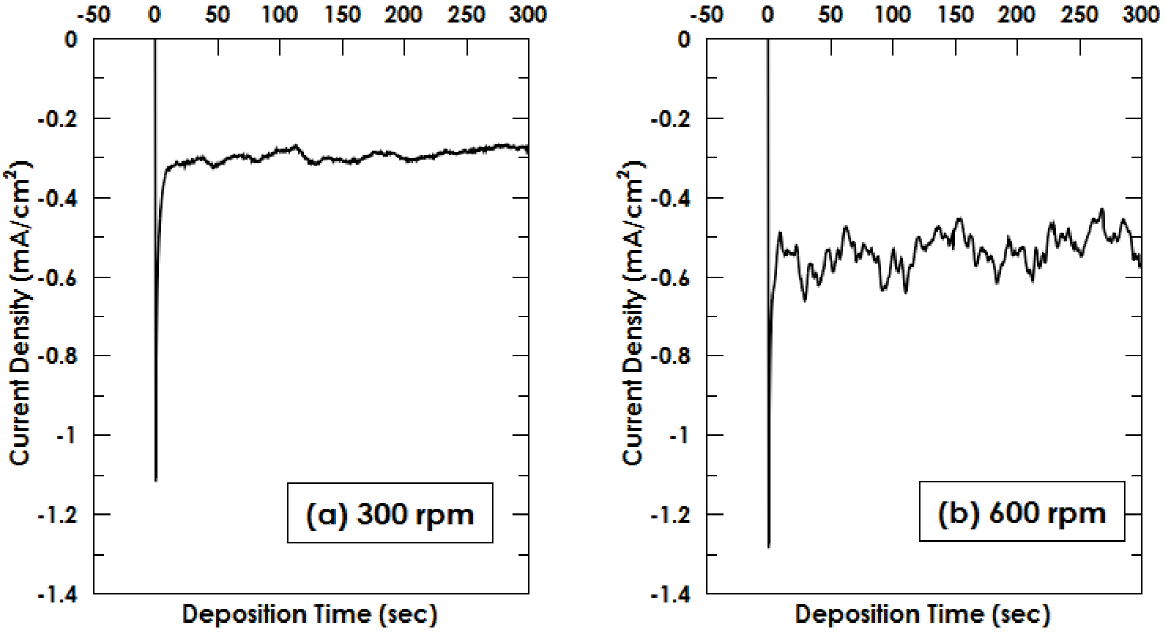

Fig. 7.15 Current density profiles obtained from stirred solutions containing $FeSO_4$ and Na_2SO_4 at different stirring rates (a) 300 and (b) 600 rpm.

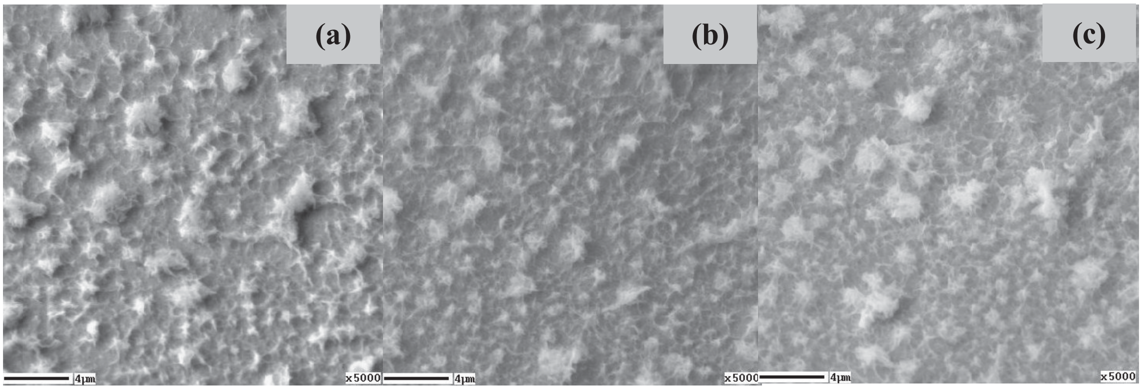

Fig. 7.16 SEM images for as-prepared Fe-O thin films from stirred solution at a rate of (a) 150, (b) 300, and (c) 600 rpm. All samples are deposited at -0.9 V for 10 min.

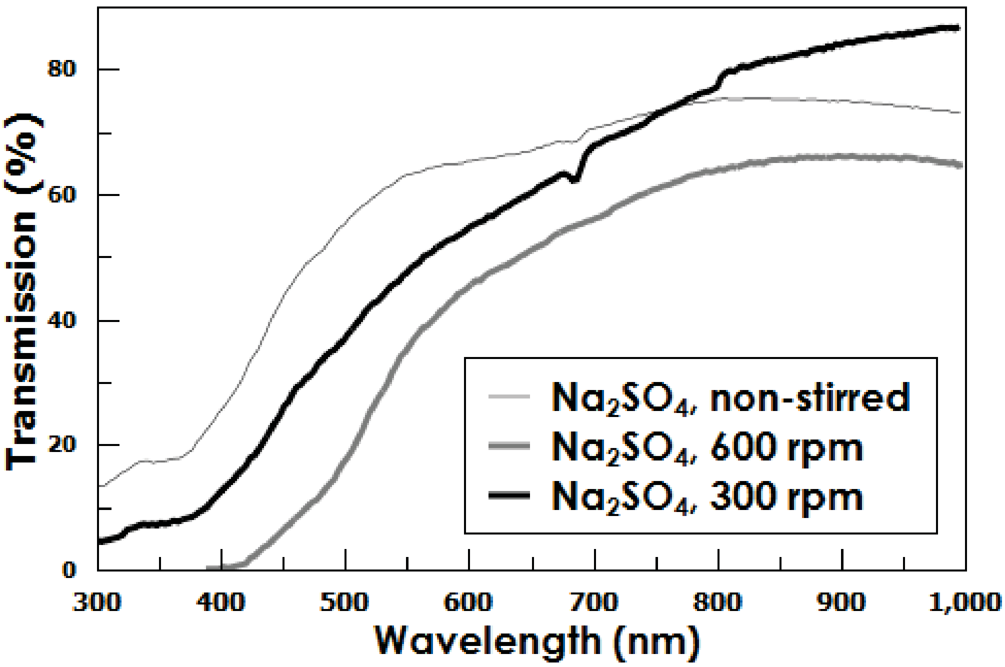

Fig. 7.17 Transmission curves for the as-prepared FeOOH films deposited from stirred $FeSO_4$-Na_2SO_4 solutions at a rate of 300 and 600 rpm. Also shown is the transmission curve for the film obtained from non-stirred condition.

The enhanced current density attained for deposition under stirring condition can be regarded as the improvement in the deposition condition. The surface morphologies of the as-prepared thin films obtained from stirred solution at different rates: (a) 150, (b) 300, and (c) 600 rpm are shown in Figure 7.16. It can be seen that a similar disperse flake like morphologies are attained with some aggregations; but it seems that the aggregation is reduced by stirring. This observation can be deduced by comparing Fig. 7.16 (c) with the morphology displayed in the inset of Fig. 7.11. Both these films exhibit same thickness (~0.35 μm); however, intense aggregation is very apparent for the film deposited under non-stirred solution. In stirred solution condition, the roughness is somewhat reduced. This is may be due to the removal of some weakly bonded aggregates by stirring during film deposition.

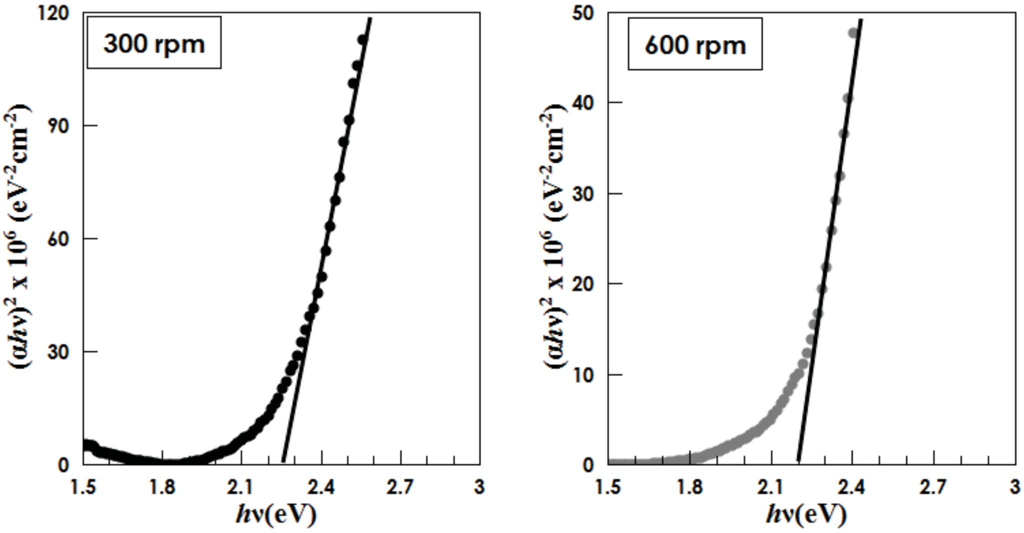

Fig. 7.18 Band gap estimation for the as-prepared films deposited from stirred $FeSO_4$-Na_2SO_4 solutions at different stirring rates (300 and 600 rpm).

Figure 7.17 shows the transmission curves for the as-prepared samples deposited at -0.9 V from stirred $FeSO_4$-Na_2SO_4 solutions at different rates (300 and 600 rpm). The reduced transmission attained for stirred solutions is due to the difference in thickness (as illustrated in Fig. 7.14 for 10 min of deposition). The corresponding Tauc's plots of the transmission curves for the samples prepared at 300 and 600 rpm are depicted in Figure 7.18. It appears that the band gaps of these films are slightly lower (2.2 – 2.25 eV). These estimated values are consistent with the observed absorption edge, which are slightly shifted towards higher wavelength (e.g. closer to 600 nm for sample deposited under 600 rpm stirring rate condition).

7.3.7 Annealing effects on Fe-O thin films: morphological and compositional analyses

Thermal annealing was performed using the tube furnace in ambient air for 1 h. The as-prepared FeOOH thin film deposited at -0.9 V for 10 min from stirred solution at a rate of 600 rpm is used for this study. The annealing temperature is kept at 400°C. Figure 7.19 shows the variation of the composition ratios: O/Fe and S/(Fe+O) with depth for the annealed film. It is observed that the surface contains no sulfur and higher O/Fe ratio (close to 2.0). After 30 s of sputtering, the O/Fe ratio reduced to ~1.80. The reason for this oxygen-rich composition is not yet investigated. Possibly, some oxygen impurities are present at or near the surface. After 120 and 300 s sputtering, the composition ratio is reduced to 1.60-1.62, which is closer to the stoichiometric ratio of Fe_2O_3. Meanwhile, the S/(Fe+O) ratio after Argon ion sputtering can be considered very small (0.02-0.03). Additionally, the morphology of the annealed sample is somewhat refined (by comparing Fig. 7.16 (c) and the inset SEM image in Fig. 19).

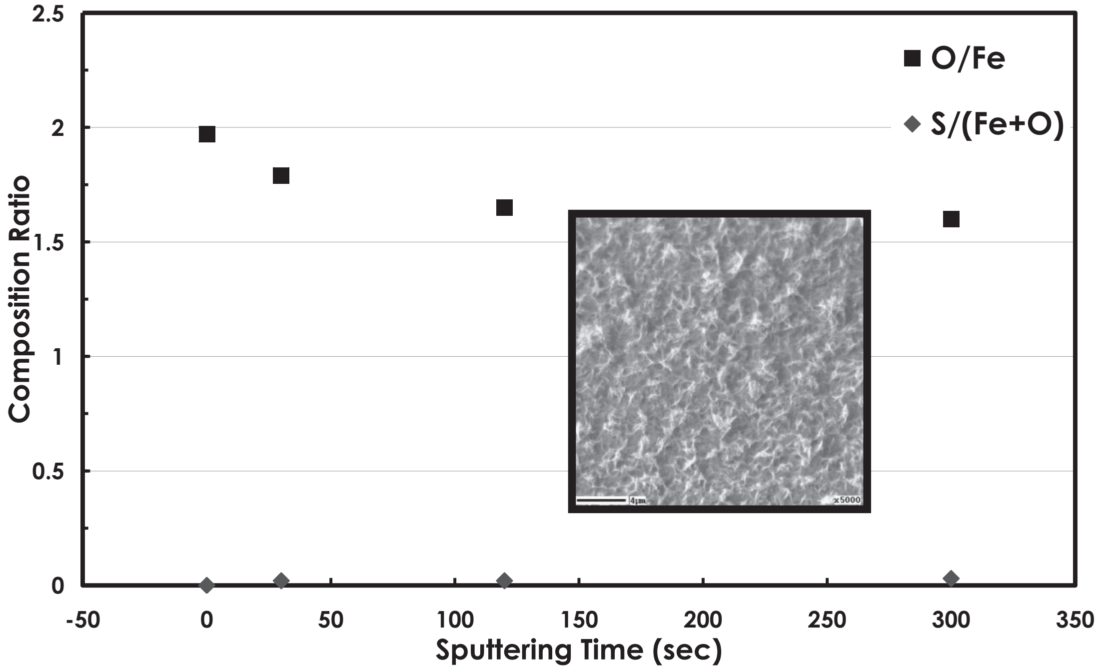

Fig. 7.19 Composition ratios (Fe/O and S/(Fe+O)) obtained from Auger analysis at the surface and the inner part of the film (annealing temperature: 400°C). Inset shows the SEM image of the annealed sample.

Raman spectroscopy is done to analyze further the chemical composition of the film. Figure 7.20 shows the Raman spectrum of the annealed sample. Also shown for comparison is the measured typical Raman characteristics of commercial Fe_2O_3 powder as standard. The prominent Raman shifts for the annealed samples are located at the wave numbers 225, 296, 408, 497, 610, and 1311 cm^{-1}. These wave numbers can be regarded as the Raman characteristics of α-Fe_2O_3 material. Also, it seems that there is a slight shift of the observed wave numbers for the annealed sample in referenced to that obtained for Fe_2O_3 powder as standard. This can be due to some defects, which could be present in the film. Thus, the transformation of electrodeposited γ-FeOOH to α-Fe_2O_3 by thermal annealing is confirmed; the result also agrees well on the reported transformation at this temperature [12].

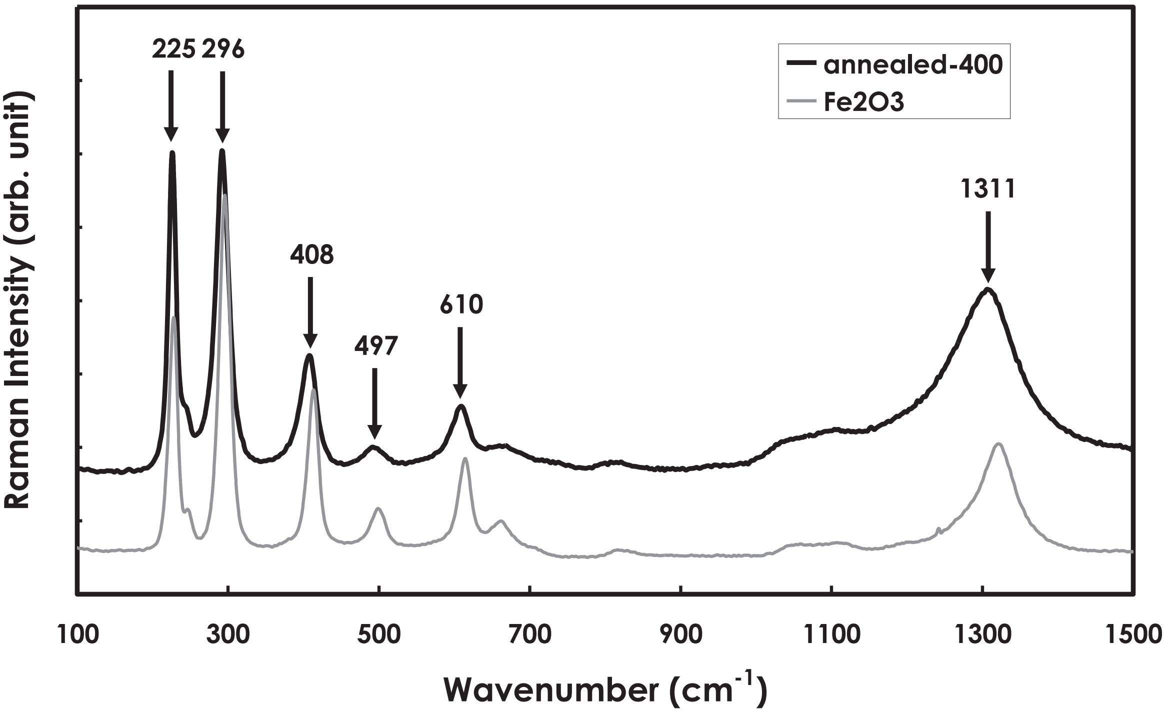

Fig. 7.20 Raman spectrum of annealed-FeOOH thin film. The typical Raman shifts of Fe_2O_3 powder is also shown for comparison.

7.3.8 Fabrication and characterization of SnS/FeOOH heterostructures

As reported by Musselman et al. that the buffering technique employed during Cu_2O electrodeposition by adding appropriate amount of ZnO powder as the buffer prevents unwanted impurities and dissolution of ZnO nanostructures during Cu_2O deposition; thus, effectively improved the photovoltaic performance of the ZnO/Cu_2O heterostructures [30].

In a similar manner, for SnS deposition solution, adding small amount of $FeSO_4$ shows improvement in the SnS deposition (continuous and adhered-well on the FeOOH film). The effect of adding $FeSO_4$ can be regarded as: (a) a buffer in the solution to suppress the dissolution of FeOOH film during SnS deposition and (b) Fe may be deposited and incorporated in the SnS forming Fe-doped SnS or the like. In the latter consideration, for an aqueous solution containing Sn^{2+} and Fe^{2+} ions, the electroreduction of Sn^{2+} is highly favorable compared to Fe^{2+} reduction since the standard potential for Sn^{2+} reduction forming Sn^0 (E^o = -0.38 V vs SCE) is less negative (or more positive) than that of Fe^{2+} reduction forming Fe^0 (-0.65 V vs SCE). Although it is possible that Fe can be incorporated in the SnS films depending on the applied potential; but at V_1 = -1.0 V, Fe peak was not detected in the AES spectrum, as shown in Figure 7.21, for the sample deposited under the described solution condition.

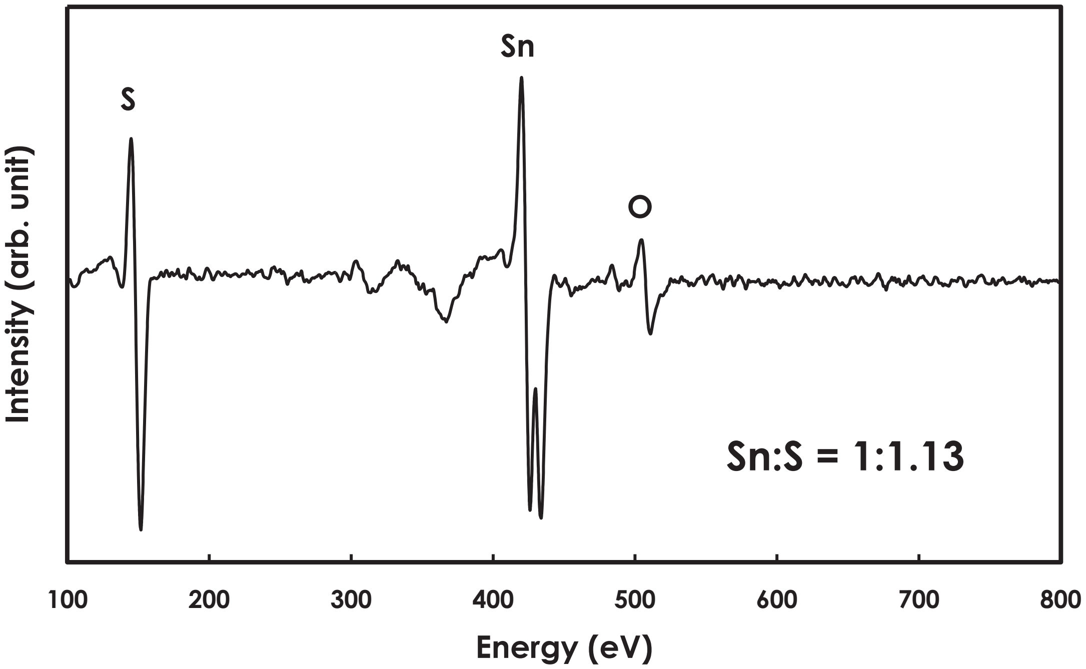

Fig. 7.21 AES spectrum for SnS thin film deposited from $FeSO_4$-$SnSO_4$-$Na_2S_2O_3$ solution.

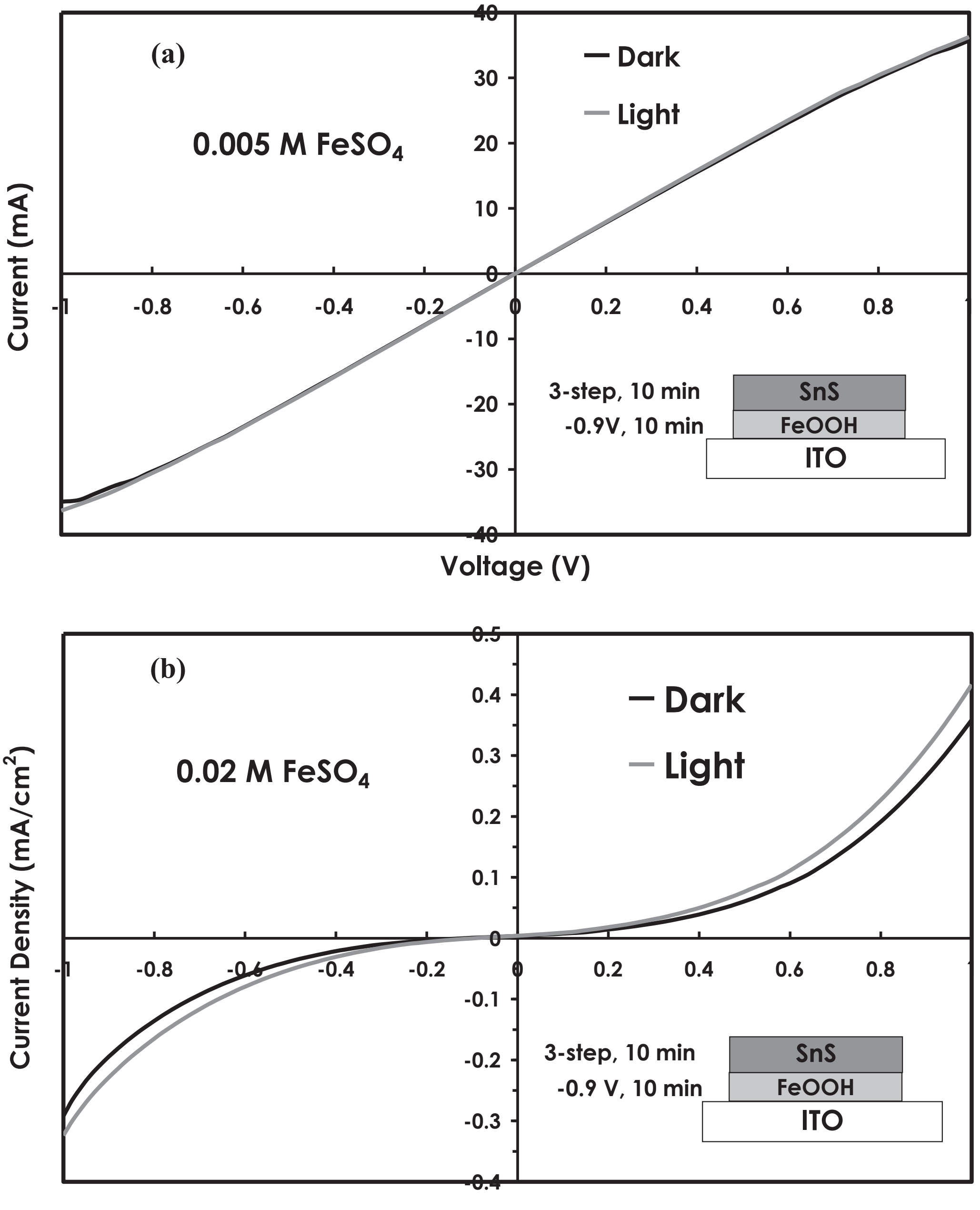

Fig. 7.22 Current-voltage characteristics of SnS/FeOOH heterojunctions with SnS layer deposited from the mixture of $SnSO_4$-$FeSO_4$-$Na_2S_2O_3$ in aqueous solution with different $FeSO_4$ concentration: (a) 0.0005 and (b) 0.02 M.

Figure 7.22 depicts the current-voltage (J-V) characteristics of the fabricated SnS/FeOOH heterojunctions with SnS layer electrodeposited from a mixture of $SnSO_4$-$FeSO_4$-$Na_2S_2O_3$ aqueous solution. For a low concentration (0.005 M) of $FeSO_4$ added in the SnS deposition solution, the heterostructure exhibited nearly ohmic type behavior and no photovoltaic characteristics were attained. However, when 0.02 M $FeSO_4$ was added in the solution prior to SnS deposition on FeOOH layer, the heterojunction characteristics showed some improvement in the rectification property; but still no photovoltaic effect was observed.

7.3.9 Fabrication and characterization of Cu_2O/FeOOH heterostructures

Another potential thin film-based *p-type* absorber material that can be utilized to fabricate heterojunction solar cells is the Cu_2O semiconductor. Cu_2O partnered with ZnO to obtain *p-n* heterostructure have shown promising photovoltaic properties [33-35]. In this regard and with the successful elucidation of the potential features of FeOOH material as discussed mostly in this chapter, the fabrication of Cu_2O/FeOOH is attempted in this work for the first time. Cu_2O thin film is electrodeposited on as-deposited and 400°C-annealed FeOOH thin film via galvanostatic approach (at constant cathodic current). Three different heterostructures were fabricated using both as-deposited and annealed FeOOH layers. For Cu_2O/FeOOH superstrate heterostructure with as-deposited FeOOH layer, two different thicknesses (0.05 and 0.35 μm) of FeOOH thin films are considered: (1) Cu_2O/0.05-FeOOH and (2) Cu_2O/0.35-FeOOH heterojunction structures.

The J-V characteristics of structure (1) are shown in Figure 7.23. From this figure, the Cu_2O/0.15-FeOOH heterojunction displays some rectifying behavior and the photocurrent is clearly observed under illumination condition. Furthermore, the photovoltaic properties of the heterostructure are evaluated by expanding the region near 0 V in the J-V curve in illumination condition as depicted in Fig. 7.23 (b). The obtained open circuit voltage (V_{OC}) and short circuit current (J_{SC}) are 0.11 V and 0.95 mA/cm^2, respectively. Moreover, the variation in the solar cell parameters is apparently observed from one electrode to another within the entire heterojunction area, that is, the photovoltaic parameters are $V_{OC} = 0.08 – 0.11$ V, $J_{SC} = 0.82 – 0.95$ mA/cm^2 and $\eta = 1.4 – 2.5 \times 10^{-2}$ %. Similarly, for structure (2) with 0.35 μm FeOOH layer, the photovoltaic characteristics are also confirmed as displayed in Figure 7.24; but the best values of the solar cell parameters for this structure are V_{OC} = 0.07 V, J_{SC} = 0.65 mA/cm^2, and $\eta = 1.2 \times 10^{-2}$ %; these values are smaller than that obtained from structure (1) with thinner FeOOH layer. Additionally, non-uniformity in the values from one electrode to another is apparent.

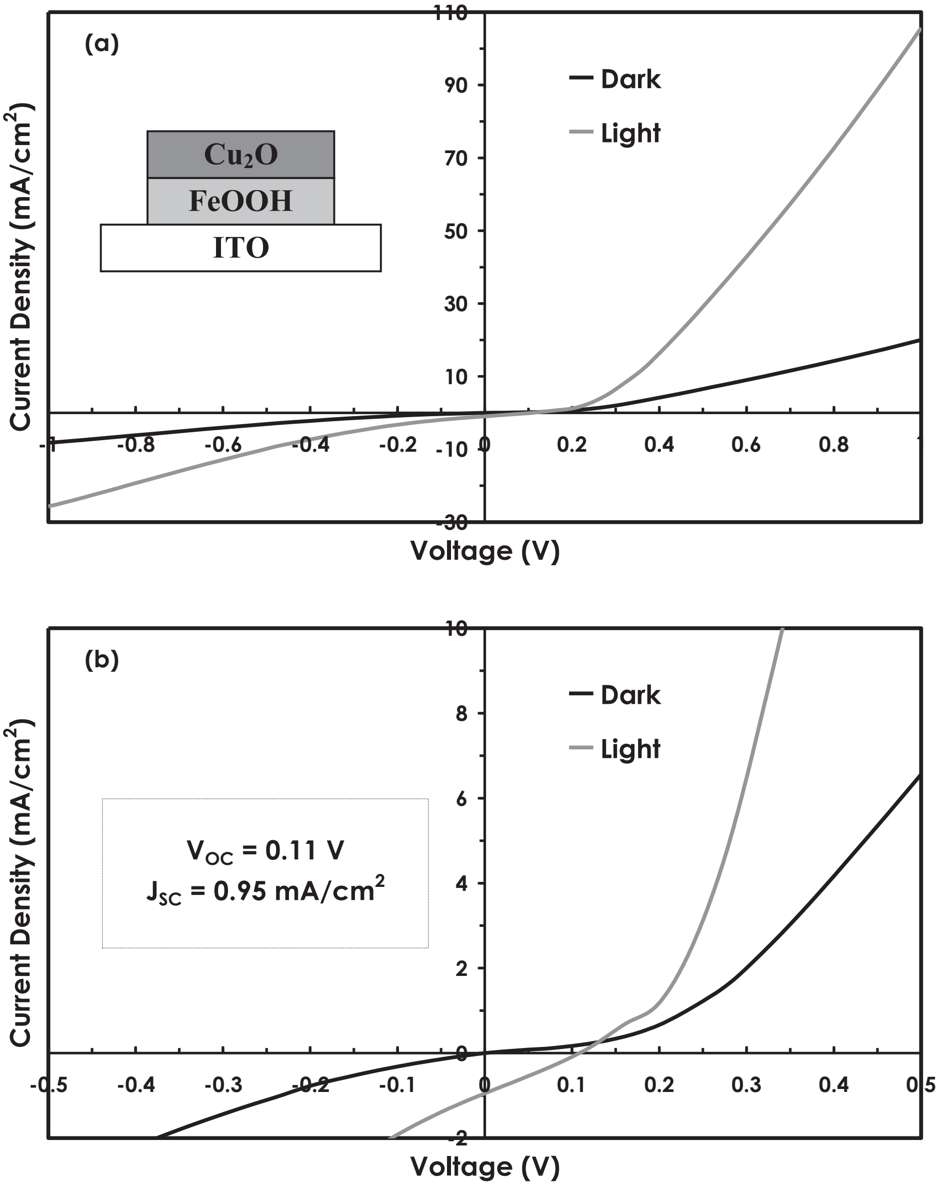

Fig. 7.23 J-V characteristics for Cu_2O/0.05-FeOOH heterojunction under dark and illumination conditions.

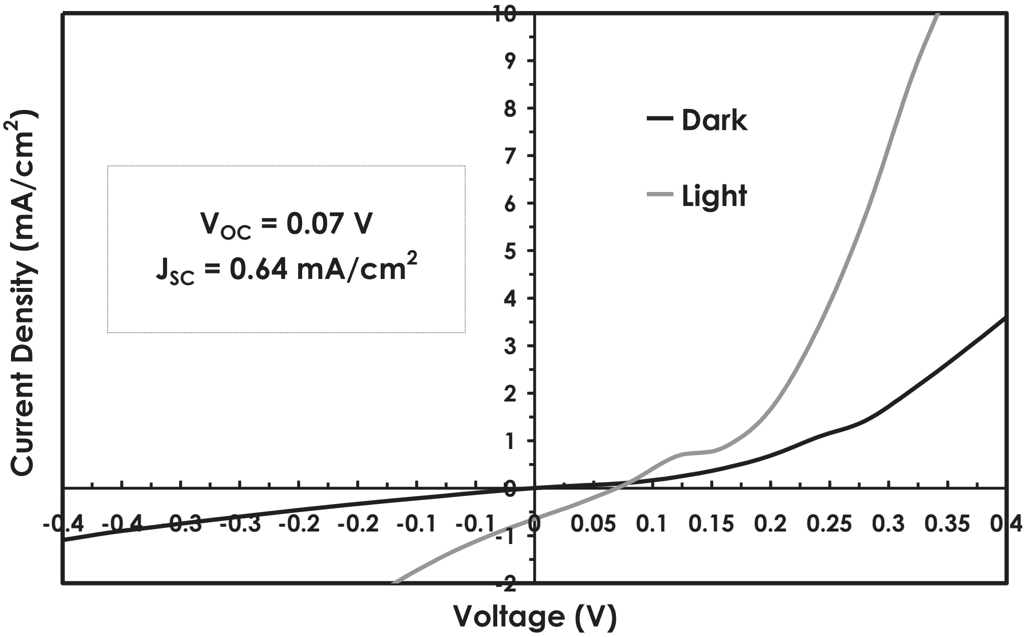

Fig. 7.24 J-V curves of Cu_2O/FeOOH heterojunction with 0.35 µm-thick FeOOH layer under dark and illumination conditions.

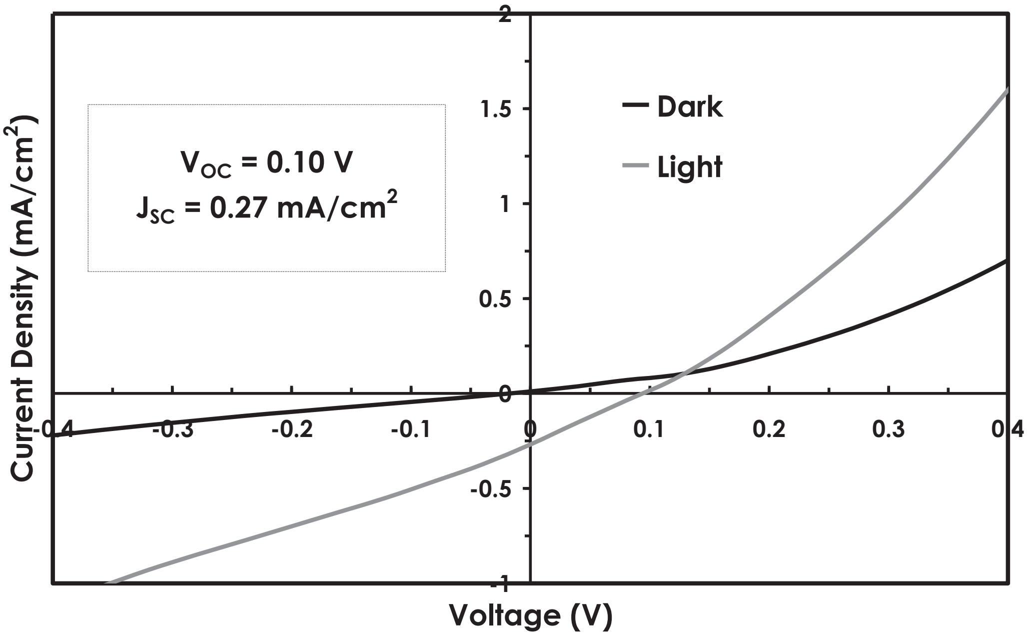

Fig. 7.25 J-V curves of Cu_2O/Fe_2O_3 heterojunction under dark and illumination conditions.

Figure 7.25 depicts the J-V characteristics of the fabricated Cu_2O/Fe_2O_3 heterostructure under dark and light conditions. The Fe_2O_3 window layer was obtained by annealing the as-prepared FeOOH layer, which was deposited at -0.9 V for 10 min prior to the electrodeposition of Cu_2O. The annealing condition was 400°C in air for 1 h. The annealed FeOOH film appeared reddish-orange, which is a typical appearance of Fe_2O_3. As seen in this figure, the Cu_2O/Fe_2O_3 heterojunction exhibits some rectifying properties and the photovoltaic characteristics are demonstrated and confirmed under light condition. The best values of the solar cell parameters are $V_{OC} = 0.10$ V and $J_{SC} = 0.27$ mA/cm^2. The estimated efficiency η is in the order of 10^{-3} %. All the fabricated heterostructures based on the combination of Cu_2O and as-deposited and annealed FeOOH (or Fe_2O_3) thin films display some rectifying and photovoltaic characteristics, but the fabrication process is not yet optimized. Further studies are still necessary to optimize the fabrication condition.

7.4 Conclusions

γ-FeOOH thin films were successfully electrodeposited on ITO substrate by employing simplified electrodeposition approach on oxygen-bubbled aqueous solution containing $FeSO_4$-KCl ions at room temperature. Potential values in the vicinity of -0.70 V vs SCE were chosen as the suitable potentials to electrodeposit pure γ-FeOOH films. Extending the deposition potential favored intense aggregation with disperse flake like morphology. Raman spectrum of the as-deposited thin film showed two sharp peaks at (252 and 384) cm^{-1} and two broad peaks at (538 and 664) cm^{-1}. These Raman shifts are the characteristics of γ-FeOOH material. From AES study, the estimated Fe/O ratios (0.51 ~ 0.54) agree well on the Raman result. Photoelectrochemical measurement revealed that the as-deposited γ-FeOOH was quite stable in Na_2SO_4 aqueous solution and exhibited n-type conductivity. Furthermore, the photoresponse was confirmed under illumination condition.

Homogeneity of the anions was performed by choosing suitable supporting electrolyte (Na_2SO_4). Electrodeposition from $FeSO_4$-Na_2SO_4 showed slight improvement in the deposition current; but the physical and morphological properties of these films did not change significantly.

However, slight change in the optical transmission and band gap was elucidated. By employing stirring during deposition, thicker γ-FeOOH could be achieved at shorter deposition time. This is due to an enhanced deposition current incurred by stirring. Improvement in the optical and morphological properties were attained under stirred solution condition. The absorption edge of the γ-FeOOH thin film was found to be between 400-600 nm wavelength range and the direct band gap was approximated to be 2.2 - 2.6 eV.

SnS/FeOOH, Cu_2O/FeOOH, and Cu_2O/Fe_2O_3 have been successfully fabricated for the first time by employing electrodeposition method. SnS/FeOOH with SnS layer electrodeposited from a mixture of $SnSO_4$-$FeSO_4$-$Na_2S_2O_3$ showed some rectification but no photovoltaic behavior. However, Cu_2O/FeOOH and Cu_2O/Fe_2O_3 heterojunctions exhibited both rectifying and photovoltaic characteristics. The best solar cell parameters: $V_{OC} = 0.11$ V, $J_{SC} = 0.95$ mA/cm^2 and $\eta = 2.5 \times 10^{-2}$ % were achieved from the Cu_2O/FeOOH heterostructure with 0.05 µm-thick FeOOH layer. Further investigation and optimization of the fabrication conditions are still needed to exploit the photovoltaic properties attained in the present experimental conditions.

References

[1] E. L. Miller, D. Paluselli, B. Marsen, and R. E. Rocheleau: Thin Solid Films, **466** (2004) 307.

[2] B. Pal and M. Sharon: Thin Solid Films, **379** (2000) 83.

[3] S. S. Kulkarni and C. D. Lokhande, Mater. Chem. Phys., **82** (2003) 151.

[4] J. Sarradin, A. Guessors, and M. Ribes, J. Power Sources, **62** (1996) 149.

[5] H. Li, W. Li, Y. Zhang, T. Wang, B. Wang, W. Xu, L. Jiang, W. Song, C. Shu, and C. Wang: J. Mater. Chem., **21** (2011) 7878.

[6] Y. Jia, T. Luo, X. Yu, Z. Jin, B. Sun, J. Liu, and X. Huang: New J. Chem. (2013) Advance Article.

[7] M. Patange, J. Jadhav, and S. Biswas: AIP Conf. Proc. **1447** (2012) 455.

[8] T. Lindgren, H. Wang, N. Beermann, L. Vayssieres, A. Hagfeldt, and S.E. Lindquist: Sol. Ener. Mater. Sol. Cells **71** (2002) 231.

[9] J. H. Kennedy and M. Anderman: J. Electrochem. Soc. **130** (4) (1983) 848.

[10] S. S. Shinde, R. A. Bansode, C. H. Bhosale, and K. Y. Rajpure: J. Semicond. **32** (2011) 013001.

[11] S. Agarwala, Z. H. Lim, E. Nicholson, and G. W. Ho: Nanoscale **4** (2012) 194.

[12] H. Naono and K. Nakai: J. Colloid and Interface Sci. **128** (1989) 146.

[13] S. Musić, S. Krehula and S. Popović: Mater. Lett. **58** (2004) 444.

[14] E. E. Carpenter, V. Cestone, G. Landry, V. G. Harris: Chem. Mater. **15** (2003) 1235.

[15] M. Nagtegaal, P. Stroeve, J. Ensling, P. Gutlich, M. Schurrer, H. Voit, J. Flath, J. Kashammer, W. Knoll, and W. Tremel: Chem. Eur. J. **5** (1995) 1331.

[16] C. Peng, B. W. Jiang, Q. Liu, Z. Guo, Z. J. Xu, Q. Huang, H. J. Xu, R. Z. Tai and C. H. Fan: Energy Environ. Sci. 4 (2011) 2035.

[17] M. Schneider and M. Stratman: Ber. Bunsenges. Phys. Chem., **96** (1992) 1731.

[18] J. Majzlan, L. Mazeina, and A. Navrotsky: Geochim. Acta **71** (2007) 615.

[19] E. Repo, M. Mäinen, S. Rengaraj, G. Natarajan, A. Bhatnagar and M. Sillanpää: Chem. Eng. J. **180** (2012) 159.

[20] T. Ishikawa, H. Nishimori, I. Abe, and K. Kandori: J. Mater. Sci. Lett. **12** (1993) 1359.

[21] T. Ishikawa, K. Takeuchi, K. Kandori, and T. Nakayama: Colloids Surf. A **266** (2005) 155.

[22] R. F. Chen, H. X. Chen, Y. Wei, and D. L. Hou: J. Phys. Chem. C **111** (2007) 16453.

[23] Y. L. Lin, Y, Wei, and Y. H. Sun: J. Mol. Catal. A: Chem. **353-354** (2012) 67.

[24] P. Borer, B. Sulzberger, S. J. Hug, S. M. Kraemer and R. Kretzschmar: Environ. Sci. Technol. **43** (2009) 1871.

[25] S. Das, M. J. Hendry, and J. Essilfie-Dughan: Appl. Geochem. **28** (2013) 185.

[26] N. Schwertmann and R.M. Corneil: Iron Oxides in the Laboratory, VCH Publishers, New York, (1991).

[27] T. Nakanishi, Y. Masuda, and K. Koumoto: J. Cryst. Growth **284** (2005) 176.

[28] H. Antony, S. Peulon, L. Legrand, and A. Chausse: Electrochim. Acta, **50** (2004) 1015.

[29] A. Jagminas, K. Mažeika, E. Juška, J. Reklaitis and D. Baltrūnas: Appl. Surf. Sci. **256** (2010) 3993.

[30] R. Schrebler et al.: Electrochem. Solid-State Lett. **10** (10) (2007) D95.

[31] L. Ryan and K. S. Choi: Chem. Mater. **21** (2009) 3701.

[32] L. Martinez et al.: J. Electrochem. Soc. **154** (3) (2007) D126.

[33] K. P. Musselman, A. Marin, A. Wisnet, C. Scheu, J. L. MacManus-Driscoll, and L. Schmidt-Mende: Adv. Funct. Mater. **21** (2011) 573.

[34] M. Ichimura and Y. Song: Jpn. J. Appl. Phys. **50** (2011) 051002.

[35] Y. Song and M. Ichimura: Jpn. J. Appl. Phys. **51** (2012) 10NC39.

[36] L. J. Brogan: *Electrochemistry of* $FeSO_4$-$Na_2S_2O_3$ *and* $CuSO_4$-$Na_2S_2O_3$ *Systems for Template-Assisted Nanowire Synthesis*, **Ph.D. Thesis** (2011).

[37] Ref. 36 & references therein.

[38] H. Lin, H. Sakamoto, W. S. Seo, K. Kuwabara, and K. Koumoto: J. Cryst. Growth **192** (1998) 250.

[39] D. L. A. de Faria, S. Venâncio Silva and M. T. de Oliveira: J. Raman Spectroscopy **28** (1997) 873.

[40] R. J. Thibeau, C. W. Brown and R. H. Heidersbach: Appl. Spectrosc. **32** (1978) 532.

[41] D. Thierry, D. Persson, C. Leygraf, N. Boucherit and A. Hugot-Le Goff: Corros. Sci. **32** (1991) 273.

[42] G. Nauer, P. Stretcha, N. Brinda-Konopik and G. Liptay: J. Thermal Anal. **30** (1985) 813.

[43] T. Ohtsuka, K. Kubo and N. Sato: Corrosion **42** (1986) 476.

[44] J. Dünnwald and A. Otto: Corros. Sci. **29** (1989) 1167.

[45] W. Rudolph, M. H. Brooker, and P. R. Tremaine: J. Solution Chem. **28** (8) (1997) 757.

[46] C. Leygraf and T. Graedel: *Atmospheric Corrosion*, Wiley-Inter-Science, New York (2000) 9.

[47] R. M. Cornell and U. Schwertmann: *The Iron Oxides*, Wiley-VCH, Weinheim (2003) 185.

[48] S.-K. Kwon, S. Suzuki, M. Saito, T. Kamimura, H. Miyuki and Y. Waseda: Mater. Trans. **46** (9) (2005) 2030.

[49] H. B. Russell: *Characterization of Hematite Nanowire Arrays Synthesized by Atmospheric Plasma*, **Ph.D. Thesis** (2009)

[50] G. Rahman and O.-S. Joo: Mater. Chem. Phys. **140** (2013) 316.

[51] Z. Sun, X. Feng, and W. Hou: Nanotech. **18** (2007) 455607.

[52] A. G. Joly, G. Xiong, C. Wang, D. E. McCready, K. M. Beck, and W. P. Hess: Appl. Phys. Lett. **90** (2007) 103504.

[53] L. Carlson and U. Schwertmann: Clay Min. **25** (1990) 65.

[54] U. Schwertmann and R. M. Cornell: *Iron Oxides in the Laboratory: Preparation and Characterization*, Wiley-VCH, Weinheim (2000) 93.

[55] M. Kiyama, N. Jikuhara, and T. Takada: Bull. Chem. Soc. Japan **46** (1973) 323.

CHAPTER 8

Summary and Conclusion

This thesis reports the essential experimental results and characterizations on the electrodeposition of three (3) transparent oxide materials (SnO_2, Ga-O, and Fe-O) at room temperature and in aqueous solutions. The effects of different electrochemical parameters are considered to explain and discuss the physical, structural, morphological, electrical and optical properties of these oxide films. The importance of the two different oxygen precursors (dissolved oxygen and H_2O_2) for successful electrodeposition of oxide semiconductors is also elucidated. Furthermore, the potential usage of these oxides are attempted and demonstrated for future considerations in solar cell fabrications. The significant results achieved and presented in the preceding chapters are summarized and suggestions for future work are discussed in this chapter.

8.1 Electrodeposited SnO_2 thin films

Electrodeposition of tin oxide (SnO_2) thin films onto ITO substrate from strongly acidic ($pH < 1$) aqueous solution containing 30 mM $SnSO_4$ at room temperature was successfully performed by employing oxygen bubbling either before or during deposition. The dissolved oxygen was considered as the oxygen precursor for the formation of SnO_2 thin films. Transparent films were obtained from oxygen-bubbled solution at shorter deposition time. The as-deposited films showed nearly stoichiometric ratios (Sn:O = 1:1.96). Photoelectrochemical measurement revealed the *n-type* conductivity and the photosensitivity of the films under illumination condition. Thermal annealing in air did not significantly change the composition of the SnO_2 films.

Superstrate heterostructures based on SnO_2 and SnS materials were fabricated by electrodeposition method. The SnS/SnO_2 superstrate structure with 250^oC-annealed SnO_2 as a window layer exhibited an open circuit voltage (V_{OC}) of 60-90 mV and a short circuit current density (J_{SC}) of 1.54-9.74 mA/cm^2. However, the solar conversion efficiencies (10^{-2} – 10^{-1}%) are still low; this could be due to the interface defects in SnS/SnO_2 heterostructure as displayed by the observed surface states in the SnO_2 layer. From core level spectroscopic analysis at the SnS/SnO_2 interface, the valence band offset was determined to be approximately 1.85 eV. Using this value and the band gaps of individual layers, the conduction band minimum of SnO_2 was predicted to be higher than that of SnS by 0.65 eV; i.e., the fabricated SnS/SnO_2 heterojunction exhibited a type I heterostructure.

8.2 Electrodeposited Ga-O thin films

Electrodeposition of Ga-O thin films on FTO-coated glass substrate was successfully carried out at room temperature from aqueous gallium sulfate solutions with hydrogen peroxide as oxygen precursor. The optimization of different deposition parameters such as deposition voltage, amount of H_2O_2 and deposition time was found to be crucial in the obtainment of a crack-free and smooth film. Nearly smooth and crack-free morphologies were attained at -1.0 (V vs SCE) deposition potential. As-deposited films showed O to Ga ratio of 2.0, which signified GaOOH formation. Thermal annealing in air at 500-600^oC reduced the O/Ga ratio closer to stoichiometric gallium oxide (Ga_2O_3) but retained the morphology of the films. As-prepared GaOOH films with ~0.2 μm thickness have 80% transparency in the visible wavelength range. However, the band gap could not be estimated because no absorption edge was observed.

Fabrication of SnS/Ga-O and Cu_2O/Ga-O heterojunctions was successfully done by employing electrodeposition of each layer. For SnS/Ga-O heterostructure, the rectification property was confirmed for structure with SnS layer deposited on thermally annealed Ga-O layer. However, the photovoltaic characteristics were not attained for this heterojunction. On the contrary, heterostructures fabricated using galvanostatically-electrodeposited Cu_2O and potentiostatically-electrodeposited Ga-O (as-deposited and annealed) layers exhibited some rectifying and photovoltaic characteristics. The solar cell parameters: open circuit voltage and short circuit current (V_{OC}, J_{SC}) are (0.15 V, 0.35 mA/cm^2) and (0.22 V, 0.45 mA/cm^2) obtained from Cu_2O/Ga-O heterojunctions with as-deposited and 400^{o}C-annealed Ga-O layers, respectively.

8.3 Electrodeposited Fe-O thin films

Another interesting oxide semiconductor is the γ-FeOOH thin film electrodeposited on ITO-coated glass substrate from oxygen-bubbled aqueous solutions containing $FeSO_4$ and either KCl or Na_2SO_4 as supporting electrolytes at room temperature. Dissolved oxygen is considered as the oxygen precursor to deposit FeOOH. Different deposition parameters such as applied potential, deposition time, nature of supporting electrolytes, and stirring conditions have shown significant effect on the quality of FeOOH films. Potential values in the vicinity of the observed reduction peak (-0.7 V vs SCE) were chosen to electrodeposit the films. The observed Raman shifts at 252, 384, 538, and 664 cm^{-1} signified the characteristics of γ-FeOOH material. The Fe/O ratios of 0.51-0.54 were obtained from AES. XRD result suggested that the as-deposited γ-FeOOH film is nanocrystalline with crystallite size probably an order of nanometers. Photoelectrochemical measurement revealed that the as-prepared γ-FeOOH film exhibited *n-type* conductivity and photoresponse was confirmed during illumination. Moreover, the inclusion of Cl impurities in the film was avoided by ensuring the homogeneity of the anions in the solution. The band gap of γ-FeOOH was estimated to be 2.2 – 2.6 eV. A transformation of γ-FeOOH thin films to α-Fe_2O_3 was attained via thermal annealing at 400^{o}C in air for 1 h as displayed in Raman result. The O/Fe ratio was about 1.6, near the stoichiometric Fe_2O_3.

The SnS/FeOOH heterostructure with rectifying behavior was fabricated and demonstrated by buffering the SnS deposition solution with $FeSO_4$. However, the photovoltaic characteristics were not confirmed in the SnS/FeOOH configuration. Interestingly, for the first time, the rectifying and photovoltaic properties of *p*-Cu_2O/*n*-Fe-O heterojunction with as-deposited FeOOH and annealed-FeOOH (Fe_2O_3) layers were demonstrated by employing a combination of potentiostatic and galvanostatic electrodeposition techniques. The obtained solar cell parameters:

open circuit voltage and short circuit current (V_{OC}, J_{SC}) are (0.11 V, 0.95 mA/cm^2) and (0.07 V, 0.64 mA/cm^2) for Cu_2O/FeOOH heterojunctions with 50 nm- and 350 nm-thick FeOOH layers, respectively; and (0.10 V, 0.27 mA/cm^2) for Cu_2O/Fe_2O_3 heterostructure.

8.4 Suggestions for future work

The present work has shown that electrodeposition of oxide semiconductor materials (SnO_2, GaOOH, and FeOOH) can be achieved from aqueous solution at room temperature with either dissolved oxygen or hydrogen peroxide as suitable oxygen precursors. Higher temperature deposition was not attempted because precipitation occurred, which could affect the desired electrochemical reaction for film formation. However, deposition at this temperature would be possible if appropriate complexing agents are added in the solution to increase the solubility of metal ions that can participate in the precipitation reaction. Additionally, electrodeposition of oxide semiconductors using organic additives and in non-aqueous solution would also be feasible to obtain better quality oxide thin films. It is known that the organic additives have the ability to bind metal ions to form stable complexes over a broad pH range, and thus, the formation of metal oxides can be promoted.

Furthermore, as observed in the structural studies, electrodeposited SnO_2, Ga-O, and Fe-O films exhibited either amorphous or nanocrystalline structural properties. Thermal treatment of as-deposited thin films has been tried but it did not show improvement in the crystallinity. Thus, it is recommended that the structural properties of these oxide films under the present experimental conditions should be improved to have better window layers for photovoltaic devices.

Deposition of SnS on SnO_2, SnS on GaOOH, and SnS on FeOOH was achieved either by employing thermal treatment on the window layers or by buffering the SnS deposition solution. In SnS/FeOOH, buffering the SnS solution deposition was found to be successful to electrodeposit SnS on as-deposited FeOOH; but the buffering condition employed in this work is not yet optimized. Further investigations should be carried out to explain the details of the effects of this buffering technique in acidic solutions. For SnS/SnO_2 and SnS/GaOOH heterostructures, thermal annealing was performed on the window layers prior to the SnS layer deposition, but only the SnS/SnO_2 heterojunction displayed photovoltaic characteristics. The solar cell conversion efficiency of the fabricated SnS/SnO_2 heterostructure is still low, and thus further improvement is necessary. It is important to note that only the interface defects due to the surface states in the SnO_2 layer have been considered as one of the limiting factors in obtaining efficient SnS/SnO_2 solar cells, while the defects in the SnS layer have not been investigated. Hence, understanding the defects that maybe present in the individual layers of the heterostructure is significant.

Meanwhile, the electrodeposited Cu_2O/GaOOH and Cu_2O/FeOOH heterojunction solar cells with as-deposited and annealed GaOOH layers displayed both rectifying and photovoltaic characteristics. But, the fabrication conditions for these heterostructures are not yet optimized. In addition to that, the Cu_2O/GaOOH and Cu_2O/FeOOH interfaces have not been studied at present. Thus, intensive effort should be performed to have optimum fabrication condition and to elucidate the band bending at the heterointerface for Cu_2O/GaOOH and Cu_2O/FeOOH configurations.

PUBLICATIONS

1. J. J. M. Vequizo, J. Wang and M. Ichimura: *Electrodeposition of SnO_2 Thin Films from Aqueous Tin Sulfate Solutions*, Jpn. J. Appl. Phys. **49** (2010) 125502.

2. J. J. M. Vequizo and M. Ichimura: *Fabrication of Electrodeposited SnS/SnO_2 Heterojunction Solar Cells*, Jpn. J. Appl. Phys. **51** (2012) 10NC38.

3. J. J. M. Vequizo and M. Ichimura: *Electrodeposition of Ga-O Thin Films from Aqueous Gallium Sulfate Solutions*, Jpn. J. Appl. Phys. **52** (2013) 075503.

4. J. J. M Vequizo and M. Ichimura: *Electrodeposition and Characterization of γ-FeOOH Thin Films from Oxygen-Bubbled Aqueous Iron Sulfate Solutions*, Appl. Phys. Exp. **6** (12) (2013) 125501.

ORAL AND POSTER PRESENTATIONS

1. J. J. M. Vequizo, M. Kato and M. Ichimura: *Electrodeposited SnO_2/SnS heterojunction for solar cell fabrication*, 71st Japan Society of Applied Physics (JSAP) Autumn Meeting (2010), September 14-17, 2010, Nagasaki, Japan.

2. J. J. M. Vequizo and M. Ichimura: *Fabrication of Electrodeposited SnS/SnO_2 heterojunction solar cells*, 21st International Photovoltaic Science and Engineering Conference (PVSEC-21) (2011), November 28 – December 2, 2011, Fukuoka, Japan.

3. J. J. M. Vequizo and M. Ichimura: *Electrodeposition of Ga_2O_3 thin films from aqueous gallium sulfate solutions*, The Institute of Electronics, Information and Communication Engineers Technical Meeting (2012), May 16, 2012, Toyohashi, Japan.

4. J. J. M. Vequizo and M. Ichimura: *Electrodeposition of Ga-O Thin Films from Aqueous Gallium Sulfate Solutions*, 73rd Japan Society of Applied Physics (JSAP) Autumn Meeting (2012), September 11-14, 2012, Ehime, Japan.

5. J. J. M. Vequizo and M. Ichimura: *Electrodeposition of Ga-O Thin Films from Aqueous Gallium Sulfate Solutions*, International Union of Materials Research Societies-International Conference on Electronic Materials (IUMRS-ICEM) (2012), September 23-28, 2012, Yokohama, Japan.

6. J. J. M Vequizo and M. Ichimura: *Electrodeposition and Characterization of γ-FeOOH Thin Films from Oxygen-Bubbled Aqueous Iron Sulfate Solutions*, 74th Japan Society of Applied Physics (JSAP) Autumn Meeting (2013), September 16-20, 2013, Kyoto, Japan.